INTERCALATION CHANNELS IN STAGED, SILVER INTERCALATED TITANIUM DISULFIDE

by

Graham R. Carlow

B.Sc. (Honours) University of Victoria, 1987

THESIS SUBMITTED IN PARTIAL FULFILLMENT OF

THE REQUIREMENTS FOR THE DEGREE OF

DOCTOR OF PHILOSOPHY

in the Department

of

Physics

SIMON FRASER UNIVERSITY

July, 1992

APPROVAL

Name: Graham R. Carlow

Degree: Doctor of Philosophy

Title of Thesis: Intercalation Channels in Staged, Silver Intercalated Titanium Disulfide

Examining Committee:

Chairperson: Dr. J.C. Irwin

Dr. Robert F. Frindt
Senior Supervisor

Dr. George Kirczenow

Dr. Albert E. Curzon

Dr. Bretislav Heinrich

Dr. John Bechhoefer

Dr. Tilman Butz
External Examiner
Habilitation in Physics
Technische Universität, München
Federal Republic of Germany

Date Approved: July 15, 1992

PARTIAL COPYRIGHT LICENSE

I hereby grant to Simon Fraser University the right to lend my thesis, project or extended essay (the title of which is shown below) to users of the Simon Fraser University Library, and to make partial or single copies only for such users or in response to a request from the library of any other university, or other educational institution, on its own behalf or for one of its users. I further agree that permission for multiple copying of this work for scholarly purposes may be granted by me or the Dean of Graduate Studies. It is understood that copying or publication of this work for financial gain shall not be allowed without my written permission.

Title of Thesis/Project/Extended Essay

INTERCALATION CHANNELS IN STAGED, SILVER INTERCALATED

TITANIUM DISULFIDE

Author:

(signature)

GRAHAM R. CARLOW

(name)

AUGUST 7, 1992

(date)

ABSTRACT

The configuration of intercalant during the intercalation of a staged, layered compound has been investigated. Single crystals of titanium disulfide were partially electro-intercalated with silver to the stage-2 phase and subsequently cleaved. The newly exposed surfaces were examined with scanning Auger microscopy in order to measure the surface silver distribution. The surface Ag was found to be in the form of narrow finger-like structures, or channels, that extend from the intercalated crystal edge to the intercalation front. The width of the channels is about 5 μm and the spacing between channels is about 10 μm. By measuring the relative Auger electron intensities of the surface elements, along with experiments involving intercalation into two adjacent crystal edges, it was determined that the measured surface elemental distributions were not the result of a cleaving effect, but a measure of the bulk intercalant distributions that existed prior to cleaving. The interpretation of these structures is that they represent Daumas-Hérold intercalation domains, and the results provide the first direct evidence of regular domain structures.

Channel domains were also obtained from Monte Carlo computer simulations of intercalation. The simulations provided insight into the formation and growth of channels, along with possible configurations for changing the channel lengthscale with the time of intercalation.

This thesis is dedicated to A. H. Ferguson

ACKNOWLEDGEMENTS

I would like to express my thanks to my senior supervisor Dr. Robert F. Frindt for his encourangement and guidance throughout the course of my graduate studies.

I would also like to thank Per Joensen for the time he took in teaching me his excellent laboratory techniques, and also for his large contribution to the work presented in this thesis.

My thanks are expressed to the members of my supervisory committee, Dr. George Kirczenow for his insightful questions and comments regarding the computer simulations; Dr. Bretislav Heinrich for the time he took to teach me the workings of the SAM; Dr. Albert Curzon for his helpful discussions on electron microscopy; Dr. John Bechhoefer for his input concerning the physics of pattern formation. In addition I thank my external examiner, Dr. Tilman Butz, for the time he took to read and comment on this thesis.

This thesis would not have been possible without the financial support that I received. For this support I wish to thank the Natural Sciences and Engineering Reasearch Council of Canada, the Simon Fraser University Physics Department, and my supervisor Dr. R.F. Frindt. I also thank Dr. Frindt for his generosity in financing my trips to conferences in both Germany and France.

Finally, I express my deepest gratitude to Cheryl (the greatest) for all her support and good humour throughout the more difficult times of this thesis.

TABLE OF CONTENTS

LIST OF TABLES

LIST OF FIGURES

CHAPTER 1

INTRODUCTION

1.1 LAYERED COMPOUNDS

Layered compounds are of general interest because of their two-dimensional behaviour. Strongly bonded atomic layers are weakly bound to each other. This anisotropy results in these materials exhibiting interesting and unusual optical, electrical, and magnetic properties (1-5). The most widely studied layered materials include graphite and the transition metal dichalcogenides (TMD's): graphite for the ease in which many different atoms and molecules can be intercalated and TMD's for their application to high energy density intercalation batteries (6).

TMD's have the formula MX_2, where M is a transition metal (group IVB, VB, or VIB in the periodic table) and X is a chalcogen (S, Se, or Te). Different TMD's have varying electrical properties (3). In general, if M is a group IVB or VIB transition metal then the TMD has semiconducting or insulating properties; those formed from a group VB transition metal tend to be metallic. The layered structure, depicted in Figure 1.1, consists of a set of strongly bonded X-M-X sandwiches which are weakly bound to each other. The weak bonding is thought to be of a Van der Waals type and permits the crystals to cleave easily along the basal plane. Within an X-M-X sandwich, the M and X atoms form two-dimensional hexagonal arrays. The relative alignment of the two X arrays within one layer give either:

(i) M atoms octahedrally co-ordinated by six X atoms, or

(ii) co-ordination of the M atoms is trigonal prismatic.

These two structures are shown in Figure 1.2.

Variations in the stacking sequence and registry of successive X-M-X sandwiches along the c-axis leads to a number of crystal types. The number of sandwiches in a unit cell can range from one to six, resulting in different crystals structures which, in turn, exhibit different properties (1-5,7).

1.2 INTERCALATION

Intercalation is defined as the insertion of "guest" atoms into a host material without seriously altering the host structure. Removal of the guest atoms, termed deintercalation, leaves the host material in virtually its initial state.

Intercalation in layered materials occurs via the guest atoms entering the host material at the crystal edge and residing in the Van der Waals gaps, also referred to as galleries. Intercalation is accompanied by deformation of the host layers in order to accommodate the guest atoms, and also by a charge transfer between the guest and host materials, resulting in the guest atoms being electrically charged. Properties of an intercalated material can change drastically, depending on the amount and type of guest atom intercalated (1).

1.3 STAGING

1.3.1 Classical Staging

Intercalation in layered materials generally occurs in stages (1). Staging refers to a long-range one-dimensional ordering of sheets of intercalated atoms which are located between the host layers. For a stage-n compound the period of ordering consists of an intercalate layer followed

by n host layers. Figure 1.3 shows examples of stage-1, stage-2, and stage-3 systems.

Many different stages have been observed for different intercalated materials (1-5). In graphite intercalation systems, stages of 10 and greater have been reported (8); in Ag intercalated TiS_2 only stage-1 and stage-2 have been observed (9). In TiS_2 intercalated with Li, only stage-1 (10) and a disordered, or short range, stage-2 (11) are known to exist. Li intercalated TaS_2 exhibits very little staging (12). Different stages for a particular intercalated material can be obtained by varying the parameters of sample preparation, such as intercalant concentration, temperature, intercalation rate, and electrochemical cell voltage.

Measurement of whether staging occurs in layered materials or not, is usually determined by X-ray diffraction. Upon intercalation, the c-spacing of the host material changes; the lower the stage, the more the c-spacing changes. For situations where a mix of stages occurs, a Hendricks-Teller (13) analysis of the X-ray diffraction [001] peak positions, relative widths, and relative intensities provides information on the stages and the amount of each stage present.

The first theoretical efforts to understand classical staging in terms of a model free energy were made by Safran (14). Each gallery was modeled by a lattice gas of N_o available intercalate sites, N_i of which are occupied in gallery i. The model free energy used was of the form

$$\emptyset = E(\{N_i\}) - \mu \sum_i N_i - kT \sum_i [N_o \ln N_o - N_i \ln N_i - (N_o - N_i)\ln(N_o - N_i)] \quad (1.1)$$

where $E(\{N_i\})$ is the configurational energy of a set of intercalate layers

of occupancy $\{N_i\}$, μ is the chemical potential, and the last term is the entropy of the lattice gas in a mean field approximation. The configurational energy used was

$$E(\{N_i\}) = \sum_i -\epsilon z N_i^2/2N_o + \sum_{i<j} V_{ij} N_i N_j/N_o \qquad (1.2)$$

The first term represents the intralayer interactions between the intercalate atoms using a Bragg-Williams quadratic form; $-\epsilon$ is the nearest neighbor in-plane interaction energy and z is the in-plane co-ordination number. The second term represents the Coulomb repulsion between different intercalate layers. The interlayer repulsion used was of the power law form

$$V_{ij} = v_o |i-j|^{-\alpha} \qquad (1.3)$$

where: v_o and α are material dependent constants, and $|i-j|$ is the c-axis separation between the two intercalant layers.

By minimizing the free energy, Ø, with respect to the gallery occupancy N_i, Safran obtained a concentration-temperature plane of the phase diagram. This phase diagram showed regions containing many periodic structures. In addition to the simple stage-n structures, there existed a complete set of fractional stages n/m and complex stages n^*. Stage n/m refers to a periodic structure where the period consists of n host layers interleaved with m occupied intercalate galleries, the remaining galleries in the period being empty. In a complex stage-n^* structure the period consists of n host layers and n galleries, and all of the galleries contain some intercalate, except for one special gallery which contains more intercalate than the others. Also existing were complex fractional stages

$(n/m)^*$.

While Safran's model predicts the simple stage-n structures which are commonly observed experimentally, no complex stages and only two fractional stages; stage-3/2 (15) and stage-4/3 (16), have been reported (in graphite).

There are thought to be two reasons for the experimental absence of complex and almost all fractional stages. The first is the form of V_{ij} in Eq. 1.3. Safran and Hamann (17) showed by a Thomas-Fermi calculation of staging energetics that

$$V_{ij} \approx 0 \text{ if any guest layer occurs between the guest layers i and j.} \qquad (1.4)$$

This strong "screening" makes it impossible for fractional stages to be stable. The second is neglecting the effects of host layer cohesion in the model free energy. Host layer cohesion, that is the energy to separate the host layers in order to admit the guest atoms, was obtained by Dahn et al. (10) who used a simple plate and spring model. In their model, the van der Waals bonds between the host layers and the elastic effects resulting from intercalated guest atoms were modeled by springs between the host layers. The host layers were treated as perfectly rigid. The separation energy obtained for a give pair of host layers was

$$E_i = \sigma N_i / (N_i/N_o + \beta) \qquad (1.5)$$

The interpretation of the constants σ and β are:

σ = energy per intercalate site required to separate rigid host layers sufficiently to admit the intercalant,

σ/β = elastic energy of the deformation of a real, bendable host

around an isolated intercalate atom.

Host layer cohesion, along with the strong screening condition, was subsequently used by Millman and Kirczenow (18) and they obtained only simple stage-n structures.

A basic assumption of the above models is that the galleries between the host layers are intercalated continuously over large distances. However, as will be shown in the following sections, there is experimental evidence that within the galleries, the intercalate clusters into small microscopic islands.

1.3.2 Stage Transformations

Stage transformations, the phenomenon where the stage index, n, of an intercalated material changes, are observed commonly in both graphite and TMD intercalation compounds (1-5). For completely intercalated crystals, stage transformations are accompanied by a change in the local intercalant concentration. This is required since the number of galleries filled with intercalant changes during the transformation. In contrast, for partially intercalated crystals the local concentration of intercalant may remain constant during a transformation. Stage transformations are, however, inconsistent with the model of classical staging. The reason for this is that, while intercalated atoms are free to diffuse within the van der Waals gap, they cannot pass through the host layers. This has been demonstrated by Hooley et al. (19) in graphite systems and by Kaluarachchi and Frindt (20) in Ag_xTiS_2. Thus, in terms of classical staging, a stage-2 to stage-3 transformation shown in Figure 1.4(a) for a completely intercalated

crystal, and the stage-1 to stage-2 transformation shown in Figure 1.4(b) for a partially intercalated crystal, cannot occur unless the intercalant in some galleries leaves the crystal and re-enters in other galleries. This unphysical idea of stage transformations led Daumas and Hérold to propose a more elegant model of staging known as the Daumas-Hérold (DH) model (21), or the domain model.

1.3.3 Domain Model of Staging

The domain model of staging is shown in Figure 1.5 for stage-2 and stage-3 systems. In this model, the intercalation compound consists of regular microscopic domains. Within any domain, the intercalate layers ("islands") are continuous and, together with the host layers, form a staged sequence, but in adjacent domains the intercalant layers lie between different pairs of host layers. Thus, a macroscopic crystal can be stage-n almost everywhere and, at the same time, globally there can be an equal amount of intercalant between every neighboring pair of host layers. Stage-1 is identical in both the classical and domain models of staging.

The domain model allows the stage index to change during a stage transformation via the lateral movement of islands of intercalant between adjacent domains. Figure 1.6 shows both the stage-2 to stage-3 transformation for a completely intercalated crystal and the stage-1 to stage-2 transformation for a partially intercalated stage-1 crystal. The formation of domains in the resulting staged systems does not require the intercalant to diffuse through the host layers.

The reasons for domain formation are dominated by the energetics of elastic effects and charge transfer.

(i) Elastic Effects: When guest atoms enter the host material the host layers locally deform in order to accommodate the guest, as in Figure 1.7(a). This local deformation is in contrast to the rigid layer approximation used in classical staging theories (Section 1.3.1). The configuration of the guest atoms will be in such a way that the bending energy caused by the deformation of the host should be a minimum. Theory by Safran and Hamann (22) and Ohnishi and Sugano (23) treated the host as an anisotropic elastic continuum deformed by intercalated guest atoms. Their result was that the effective elastic interaction between guest atoms within the same gallery was attractive, which leads to island formation (Figure 1.7(b)). Also, the interaction of guest atoms in neighboring galleries, separated by a pure c-axis displacement, was repulsive. This leads to islands formed in neighboring galleries to be "staggered" along the c-axis, giving rise to domains (Figure 1.7(c)).

(ii) Charge Transfer: Upon intercalation, electrons are transferred from the guest to the host (for a donor guest) or from the host to the guest (for an acceptor guest). The amount of charge transfer depends on the guest, the host, and to a lesser extent on the stage. The Coulomb repulsion (Eq. 1.3) between charged intercalant layers, or islands, also results in staggered islands along the c-axis.

Kirczenow (24) used the idea of effective elastic and Coulomb interactions of guest atoms in novel three-dimensional Monte Carlo computer simulations of intercalation and deintercalation of microcrystals. In these simulations, the intercalate in the crystal was made of small, identical elementary islands (EI) which interact via a Hamiltonian based on

the Safran-Hamann model. The EIs entered the crystal edge from an intercalate reservoir and could move on a regular lattice of sites. The movement of EIs from site to site was determined from a standard Monte Carlo algorithm. The results were the first real-space visualizations of the microscopic processes involved in intercalate transport. Intercalation, island and domain formation, staging and stage transformations were all readily observed. Figure 1.8 shows such a simulation for a system intercalated to stage-2, and it reveals very clearly the existence of intercalation domains. An excellent review of these simulations is available in the literature (25).

Although these theoretical simulations give a direct visualization of the domain model, to date most experimental work provides only indirect evidence for the existence of islands and domains. Many experimental studies of stage transformations and intercalation kinetics are interpreted in terms of the domain model (26,27). For example, a pressure induced stage-2/stage-3 transformation (28) in potassium intercalated graphite was shown to be reversible (although hysteretic). The reversibility implies that the intercalate redistributes within the host galleries during the transition, as required by the domain model. Estimates of in-plane domain sizes are usually inferred by analyses of X-ray line widths and give values which range from 100Å to 10,000Å (26,28,29).

Direct experimental observation of intercalation domains is difficult to obtain and few results have been published. Thomas et al. (30), viewed intercalate structure edge on using atomic resolution electron microscopy on a residual compound of $FeCl_3$ intercalated graphite. The technique gave

real-space pictures revealing the stacking sequence of intercalate and host layers. Their results showed statistical distributions of intercalated layers, inter-penetration of differently staged regions, and isolated islands of intercalate. Since the technique viewed the intercalate edge on, it was not capable of determining the lateral shape of domains. Recently, Levi-Setti et al. (31), using a focussed ion beam and secondary-ion mass-spectroscopic mapping, observed randomly distributed bead-like regions on the surface of cleaved stage-2 and stage-4 $SbCl_5$ intercalated graphite. These regions had a typical lateral dimension of about 2000Å and were interpreted as intercalation domains. However, Bretz and Clarke (32) submitted that these regions were a result of the surface-exposed intercalate migrating and selectively decorating the exposed graphite surface and therefore having no connection to domain structure. The controversy was never resolved.

Despite much effort, no unambiguous, direct evidence of the lateral extent and shape of intercalation domains has been obtained. Such information is essential for a complete understanding of the dynamics of the intercalation process and the two-dimensional diffusion mechanism of the intercalant between the host layers.

1.4 TITANIUM DISULFIDE

Titanium disulfide (TiS_2) is a layered transition metal dichalcogenide as shown in Fig. 1.1, where M = Ti and X = S. Its structure is 1T (T for trigonal), that is, there is one S-Ti-S sandwich per unit cell and the Ti atom is coordinated by six S atoms octahedrally, as in Fig. 1.2(a). TiS_2 crystals are usually grown by the standard iodine-vapor-

transport method (33,34) which yields thin, plate-like crystals. Their lateral dimension is typically a few millimeters and they range in thickness from 10μm to 100μm. The weak bonding of the S-Ti-S sandwiches permits the crystals to be cleaved, along the basal plane, to thicknesses as small as a few hundred angstroms. The hexagonal TiS_2 unit cell and lattice parameters are shown in Figure 1.9. For each Ti atom, there are two tetrahedral sites and one octahedral site in the Van der Waals gap. The crystals have semi-metallic properties.

TiS_2 can be intercalated with donor guest atoms only. Intercalation with alkali metals such as lithium and sodium provides large voltages and high diffusion rates of the intercalate within the host galleries. For these reasons, these intercalation systems have great practical importance for use as high energy density batteries. From a purely experimental point of view, alkali metals are very inconvenient to use due to their high reactivity. Therefore, often the pseudo alkali metal, silver, is used as an intercalant species. Silver has the additional advantage that its presence can be readily detected by X-rays.

1.5 SILVER INTERCALATION IN TiS_2

Silver is readily intercalated into TiS_2 with a standard electrochemical cell (35) ($Ag_xTiS_2 | Ag^+ | Ag$) using an electrolyte of $AgNO_3$ in either water, glycerol, or acetonitrile. Upon intercalation the Ag resides in the Van der Waals gaps, and occupies the octahedral sites (9).

In Ag_xTiS_2, two different stages are known to exist, depending on the value of x:

(i) for $0.35 < x < 0.42$ the intercalated crystal is stage-1 (9).

Using electrochemical cell techniques, $x \approx 0.42$ is the largest fraction of Ag that can be intercalated. The expansion of the TiS_2 lattice parameters for a stage-1 system , along with the Ag position in the unit cell, are shown if Figure 1.10(a). The c-spacing expands by about 12% (9), in order to accommodate the Ag atoms. The change of the lattice parameters is measured with X-ray diffraction. At temperatures below about 250 K the Ag forms a $\sqrt{3}a_o \times \sqrt{3}a_o$ superlattice (36);

(ii) for $0.15 < x < 0.25$, the intercalated crystal is stage-2 (9). The lattice parameters and unit cell are shown in Figure 1.10(b). Again, in the Ag occupied regions, a $\sqrt{3}a_o \times \sqrt{3}a_o$ superlattice exists at temperatures below about 290 K (36). If x falls between the stage-1 and stage-2 values, the crystal contains a mix of the two stages.

Identifying a crystal as being in the stage-2 phase is more involved than identifying the crystal to be in the stage-1 phase. For stage-1 , every gallery is completely filled with Ag, while for stage-2 only every other gallery is filled with Ag (for a classical staging model). This long range ordering of full and empty galleries that exists for pure stage-2 cannot be determined strictly from the positions of the [001] X-ray diffraction peaks. Thus, Mori et al. (37) measured the positions and intensities of the [001] diffraction peaks for a stage-2 system ($x = 0.19$). They fitted many peaks ($4 \leq l \leq 29$) and unambiguously determined the long-range ordering, along the c-axis, that exists in the stage-2 system.

Another phase of Ag_xTiS_2 is the dilute stage-1 phase (9). The phase is often prepared by thermal intercalation techniques and occurs when $x \leq 1/12$. In the dilute stage-1 phase, the Ag occupies random octahedral sites in every gallery, thus it is similar (from a staging point of view)

to the regular stage-1 phase, except with a much lower concentration of Ag.

Kaluarachchi and Frindt (20) have shown that a TiS_2 crystal partially intercalated with Ag to stage-1 is unstable at room temperature, and rapidly converts to stage-2. They also demonstrated that the diffusion coefficient of Ag perpendicular to the TiS_2 layers is about five orders of magnitude smaller than the diffusion coefficient along the layers. This large anisotropy of diffusion justifies the assumption of two-dimensional motion for intercalate in the host galleries. Therefore, the stage-1 to stage-2 transformation occurs without Ag passing through the host layers and, according to the domain model, intercalation islands and domains should exist in stage-2 Ag/TiS_2. One indirect measurement of the domain size was reported by Kaluarachchi and Frindt (27). The lateral domain size was estimated to be 100-200 Å, based on a moving island model applied to sloping intercalation fronts of partially intercalated crystals.

1.6 THESIS WORK

The work in this thesis is part of the ongoing research at Simon Fraser University in the study of the properties of intercalated transition metal dichalcogenides. Silver intercalated titanium disulfide is a commonly studied system and the object of the author's research was to determine, directly, the lateral size and shape of intercalation domains in stage-2 Ag/TiS_2.

Intercalate distributions were determined by examining freshly cleaved surfaces of partially intercalated stage-2 crystals using a Scanning Auger microprobe and optical observation. The distributions were

determined through a series of Auger line scans and Auger maps. With this approach an immediate complication arises, since one is attempting to measure a bulk property of intercalation systems (domains) whereas Auger analysis is essentially a surface probe. Inferring bulk structure from surface analysis is always dangerous, so a large fraction of the research was spent attempting to prove that the surface intercalate distributions measured were representative of the bulk distributions.

In this thesis, the Scanning Auger Microprobe (SAM) and its modes of operation are described in Chapter 2. Although the SAM is much more versatile than is indicated in the chapter, only its operation as pertaining to this thesis is presented. The preparation of stage-2 Ag intercalated TiS_2, starting from TiS_2 single crystals, is described in Chapter 3. In Chapter 4, results of intercalate distributions obtained from the SAM are presented. Optical results of intercalate distributions are presented in Chapter 5, and these results are compared to those obtained by the SAM. Monte Carlo simulations of intercalation are presented in Chapter 6. Chapter 7 examines the intercalate distributions obtained both experimentally and during simulations, and provides a three-dimensional domain model of intercalation. Chapter 8 draws conclusions of the results obtained in this thesis work.

Fig. 1.1 Stacking of X-M-X sandwiches in transition metal dichalcogenides.

X - chalcogen

M - transition metal

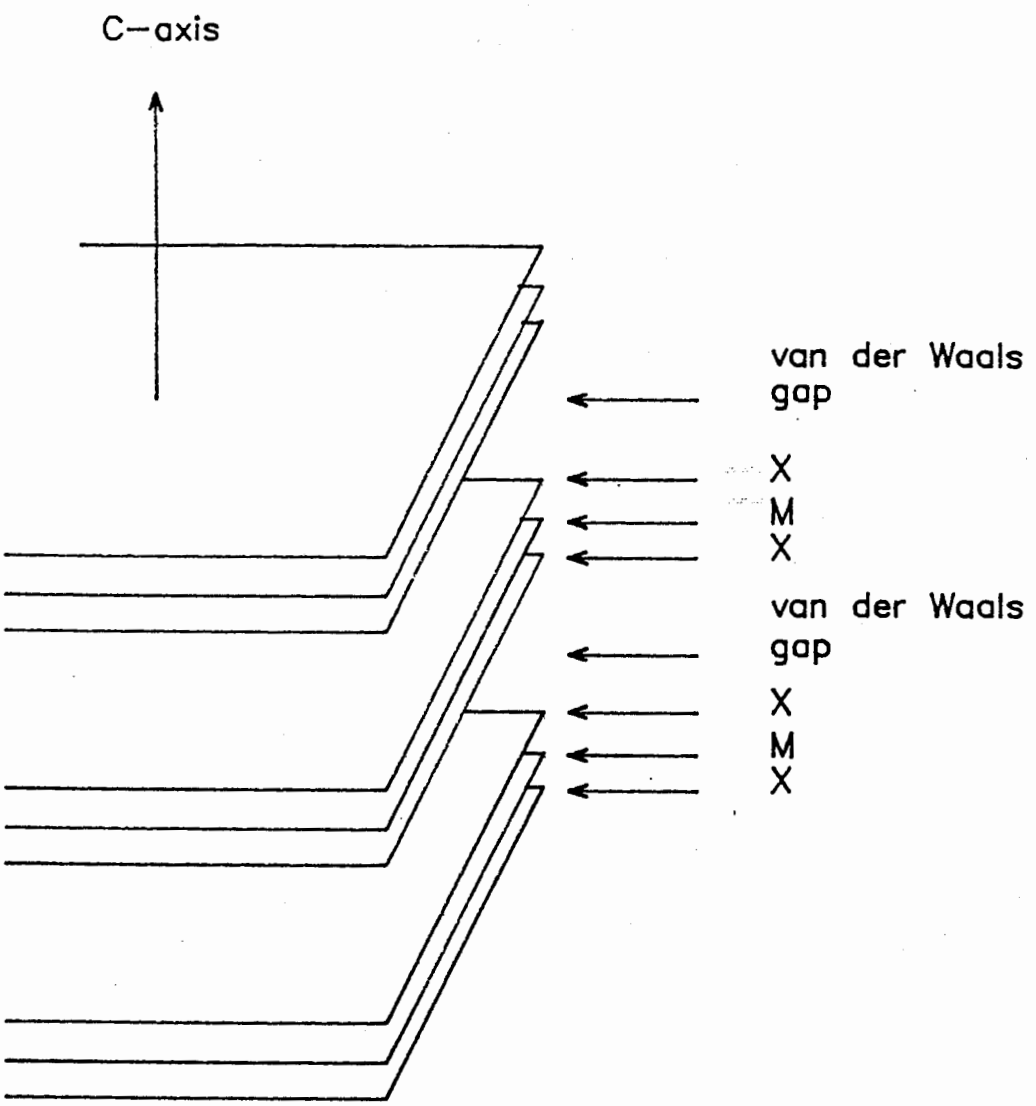

Fig. 1.1

Fig. 1.2 Chalcogen coordination around the transition metal atoms.

(a) Octahedral

(b) Trigonal prismatic structure

filled circle = transition metal

hollow circle = chalcogen

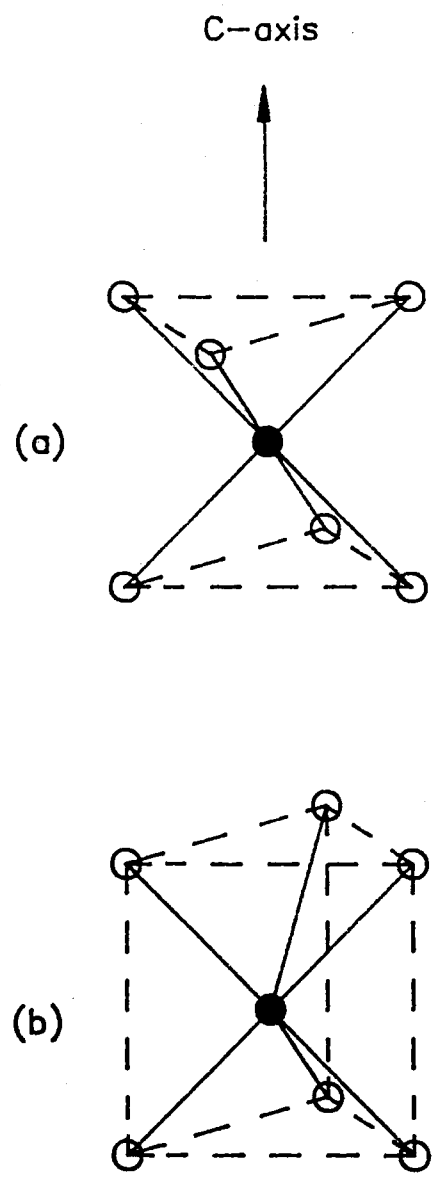

Fig. 1.2

Fig. 1.3 The classical model of staging.

straight line - Host layers

filled circles - Guest atoms

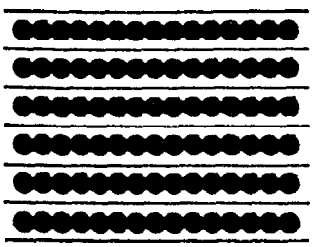

Stage 1

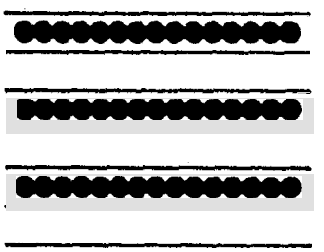

Stage 2

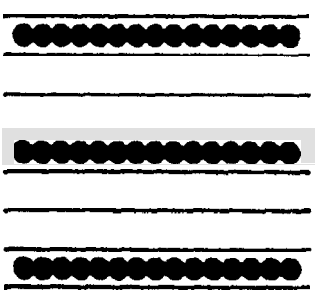

Stage 3

Fig. 1.3

Fig. 1.4 Stage transformations disallowed in the classical staging model.

(a) Stage-2 to stage-3 transformation for a fully intercalated crystal.

(b) Stage-1 to stage-2 transformation for a partially intercalated crystal.

straight lines = host layers

filled circles = guest atoms

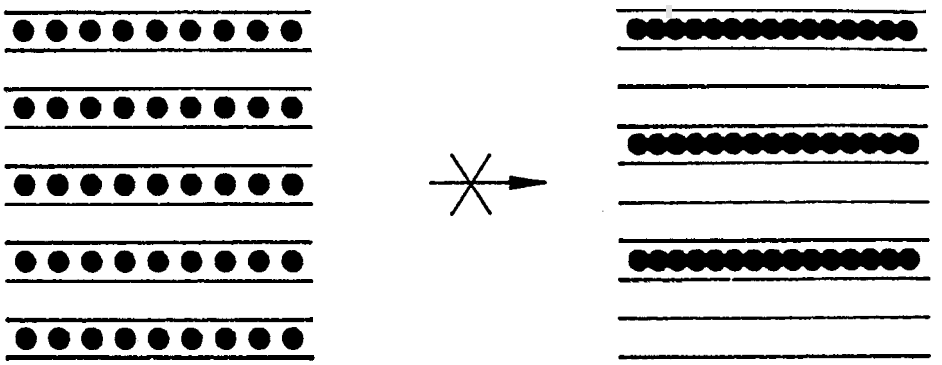

Stage 2 Stage 3

(a)

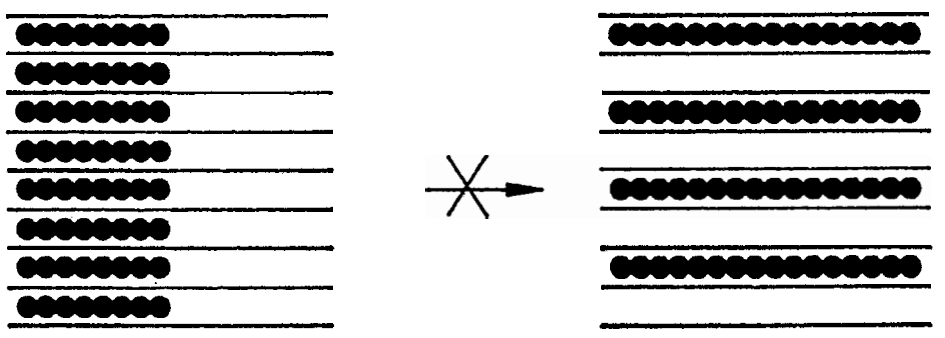

Stage 1 Empty Crystal Stage 2

(b)

Fig. 1.4

Fig. 1.5 Daumas and Hérold's domain model of staging.

straight lines = host layers

filled circles = guest atoms

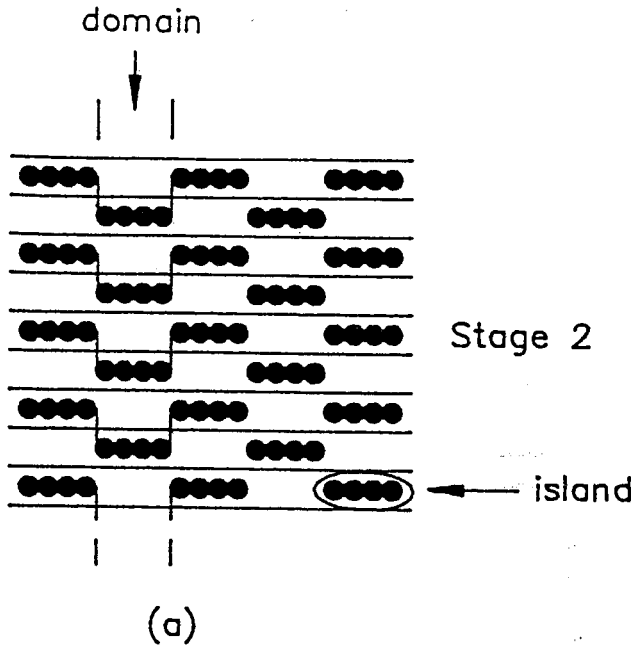

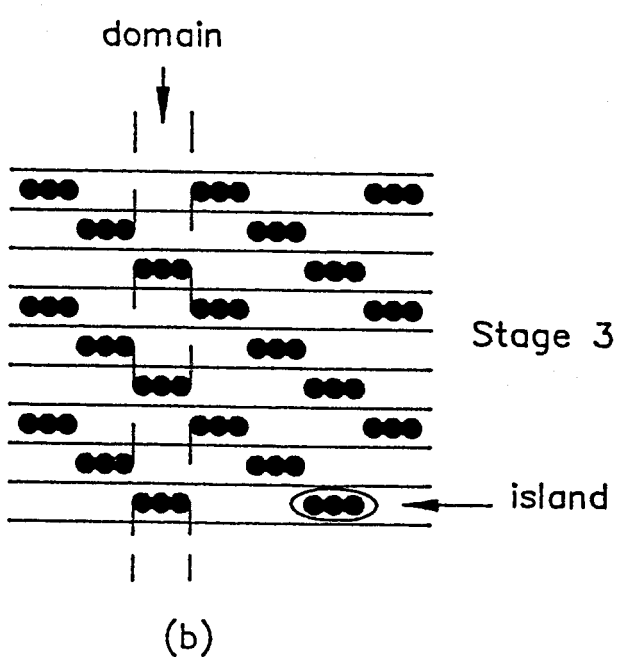

Fig. 1.5

Fig. 1.6 Stage transformations according to the Daumas-Hérold domain model of staging.

(a) Stage-2 to stage-3 transformation for a fully intercalated crystal.

(b) Stage-1 to stage-2 transformation for a partially intercalated crystal.

straight lines = host layers

filled circles = guest atoms

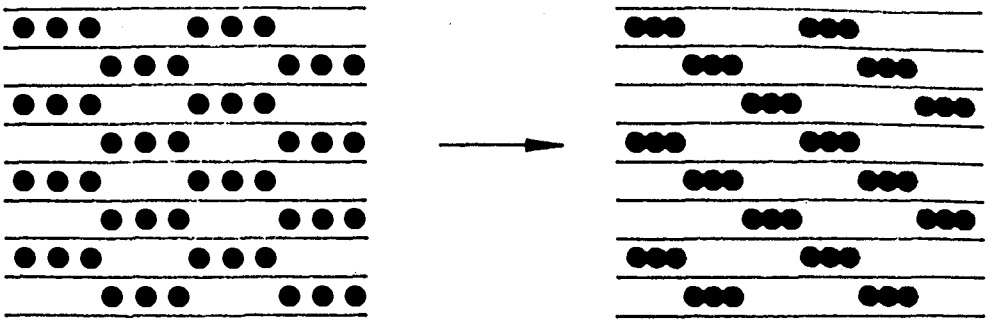

Stage 2

Stage 3

(a)

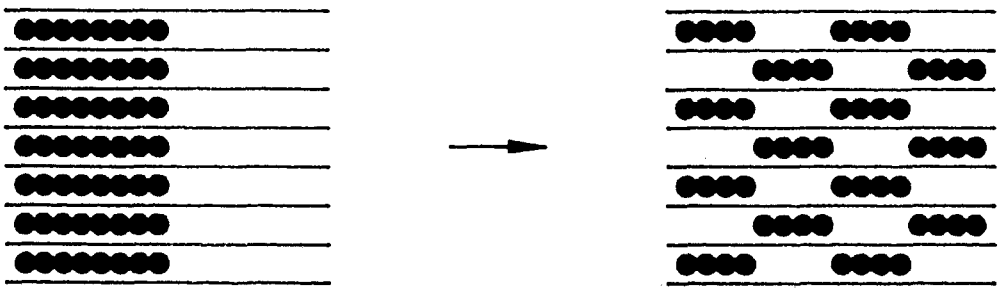

Stage 1 Empty Crystal

Stage 2

(b)

Fig. 1.6

Fig. 1.7 Elastic interactions of intercalant atoms.

(a) Local deformation of the host layers around a guest atom.

(b) Attractive interaction between the guest atoms within the same host gallery. (refs. 22 and 23)

(c) Repulsive interaction of guest atoms separated by a pure c-axis displacement. (refs. 22 and 23)

lines = host layers

filled circles = guest atoms

(a)

(b)

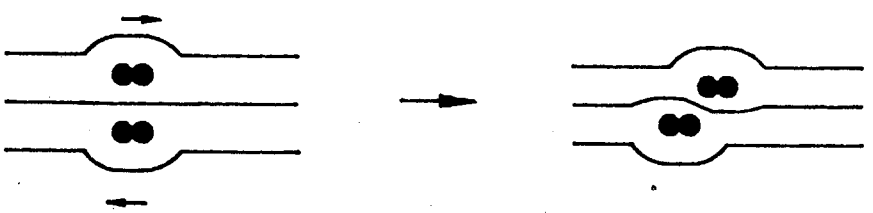

(c)

Fig. 1.7

Fig. 1.8 Three-dimensional Monte Carlo computer simulation of intercalation of a pristine host to stage-2.

Each column represents a stack of Van der Waals' galleries at a different time in the intercalation process. Time increases from left to right. The intercalant is shown as black areas in Van der Waals' galleries 1 to 10 in the crystal. Gallery 1 is next to the basal surface and gallery 10 is near the crystal center. The intercalant enters into the crystal from a reservoir at the left of each gallery.

(Courtesy of Dr. G. Kirczenow)

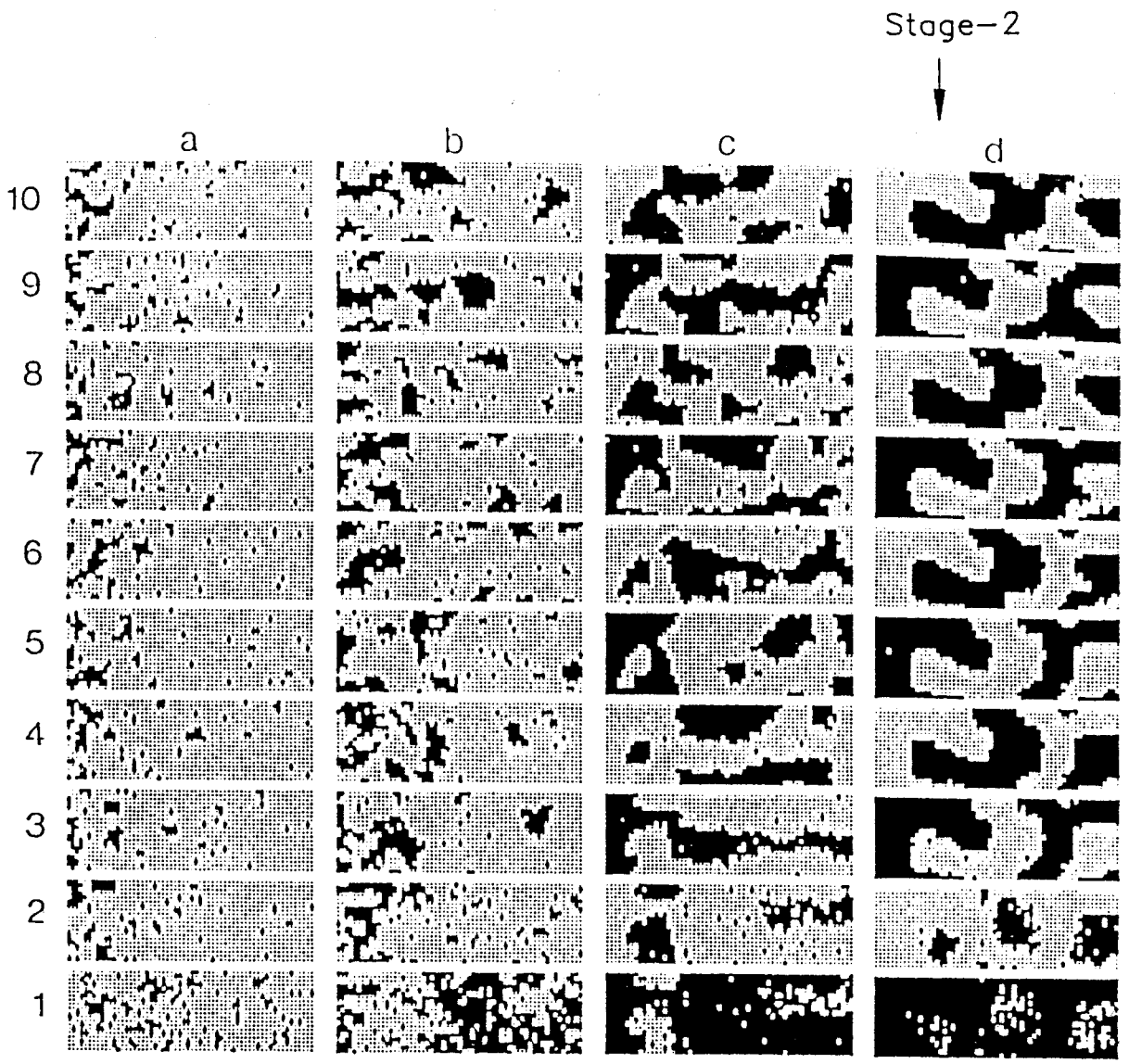

Fig. 1.8

Fig. 1.9 The atomic structure of TiS_2.

(a) The stucture of TiS_2.

(b) The $(11\bar{2}0)$ diagonal cross-section of the TiS_2 unit cell.

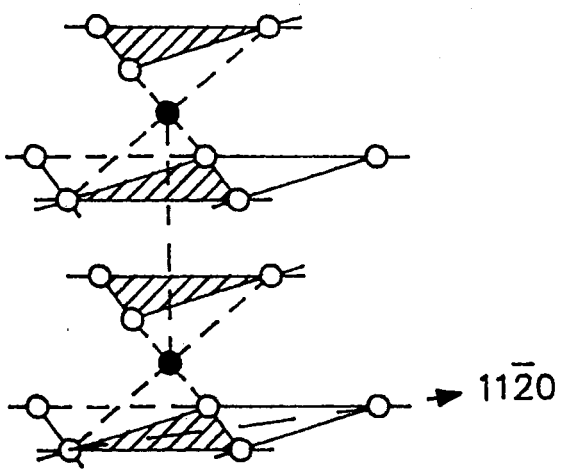

(a) $1T-TiS_2$

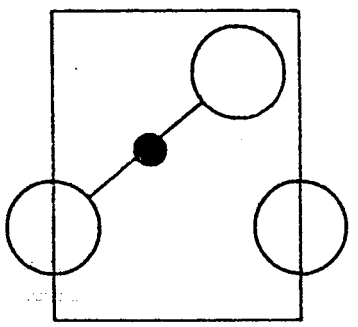

$a_o = 3.404 \pm 0.001$ Å

$c_o = 5.696 \pm 0.003$ Å

(b)

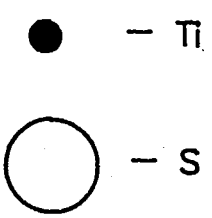

Fig. 1.9

Fig. 1.10 The atomic structures of stage-1 and stage-2 Ag/TiS_2.

(a) The $(11\bar{2}0)$ diagonal cross-section of $Ag_{0.42}TiS_2$ unit cell.

0.42 of the octahedral sites are occupied with Ag atoms.

(b) The $(11\bar{2}0)$ diagonal cross-section of $Ag_{0.20}TiS_2$ unit cell.

0.20 of the octahedral sites are occupied with Ag atoms.

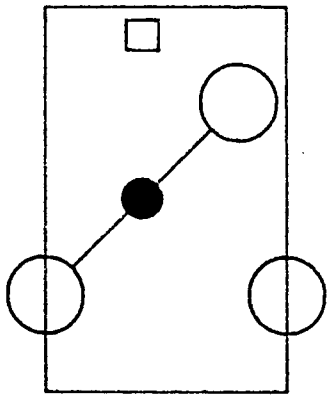

$a_o = 3.437 \pm 0.001$ Å

$c_o = 6.445 \pm 0.003$ Å

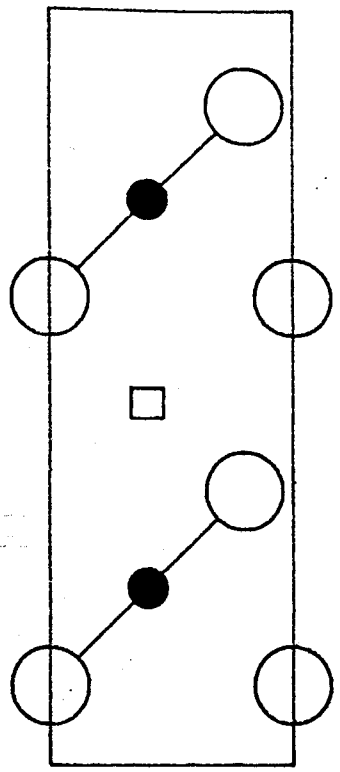

$a_o = 3.416 \pm 0.001$ Å

$c_o = 12.145 \pm 0.005$ Å

□ – Ag

○ – S

● – Ti

(a) (b)

Fig. 1.10

CHAPTER 2

INSTRUMENTATION

2.1 AUGER ELECTRON SPECTROSCOPY

In recent years Auger electron spectroscopy (AES) has become an extremely powerful tool in the investigation of surface composition. The principle of the Auger process is illustrated in Figure 2.1 (38,39). A sample is bombarded with an electron beam of several keV energy. This ionizes atoms, to a depth of about 1 μm below the sample surface, by ejecting an electron from an atomic core level A. The atom then relaxes by an electron from a level B filling the core hole. The energy difference between these two levels is transferred to an electron in a level C, which is emitted from the atom. This electron, known as the Auger electron, is named after Pierre Auger, who first discovered the process. The energy of the Auger electron, which depends on the three energy levels participating in the process, uniquely defines its parent atom. A specific Auger process is labelled 'ABC', and different transitions can occur for one atomic species. For example, the dominant Auger transitions for Ag, S and Ti are MNN, KLL and LMM respectively. The energies of the Auger electrons corresponding to these transitions are: E_{Ag} = 351 eV, E_S = 152 eV and E_{Ti} = 418 eV.

Auger electron energies lie in the range 0 - 2 keV and due to strong inelastic scattering which occurs at these energies, only electrons very near the sample surface can be ejected from the sample and contribute to the Auger spectrum. Figure 2.2 schematically shows the theoretical dependence of electron escape depths on the electron energy (40). Typical

escape depths of Auger electrons are 2 to 20 angstroms, and for this reason AES is extremely surface sensitive. Note that, ideally, the electron escape depths shown in Fig. 2.2 are independent of the material in which the electrons are travelling. Experimentally measured escape depths follow this so-called "universal curve" quite well, with only a small degree of scatter about the theoretical curve (40).

The measured energy spectrum consists of small peaks corresponding to Auger transitions superimposed on a large background. The peak positions are independent of the incident beam energy since they only depend of the atomic energy levels. The positions are also independent of temperature since the natural width of the Auger peaks is much greater than typical phonon energies.

The lateral resolution of AES, which is limited by the minimum diameter of the incident electron beam, can generally be kept as low as a few hundred angstroms. The sensitivity of AES is such that an atomic species with a concentration as low as 0.1% can be detected. All elements except hydrogen and helium can be analyzed since three occupied energy levels are required in the process.

2.2 ULTRA HIGH VACUUM

When using AES, all measurements are usually carried out under an ultra-high vacuum (UHV). The necessity of this is two-fold. First, Auger electrons emitted from the sample surface must not lose energy through scattering with gas molecules before entering the analyzer. Second, and most important, is to avoid contamination. Since only surface atoms are analyzed with AES, surface contamination must be kept to a minimum. At a

pressure of 10^{-6} torr, a monolayer of gas will accumulate on the sample surface in a matter of seconds (38, p. 18). This is obviously unacceptable. To avoid these problems, AES is done in an UHV of around 10^{-10} torr.

All samples analyzed must be handled with great care. Any materials entering the UHV chamber, such as a sample substrate or sample holder, must be kept very clean. Failure to do so may cause unwanted contamination and could result in degradation of the UHV.

2.3 SCANNING AUGER MICROSCOPE

Auger analysis performed in this thesis was done using a Perkin-Elmer model 595 Scanning Auger Microscope (SAM). A schematic of the system is illustrated in Figure 2.3. The sample chamber is kept under UHV by the use of a Diode Ion Pump. The incident electron beam is created by electrically heating a crystal of Lanthanum Hexaboride. A current of 2 A is used for this purpose and the crystal emits electrons which are accelerated toward the sample surface at several keV. The beam is then focussed onto the sample surface by a series of condenser and objective lenses. The diameter of the beam increases with the beam current as shown in Figure 2.4 (40), so one must sacrifice current (requiring longer data acquisition times) in order to improve the lateral resolution. All properties of the electron beam (energy, current, focusing) are operator controlled via a microprocessor.

The energies of the electrons emitted from the sample surface are measured with a cylindrical mirror analyzer (CMA). A CMA is shown schematically is Figure 2.5. Electrons leaving the sample enter an

aperture into the CMA. Here, two cylinders of different radii are positioned coaxially, with the outer cylinder at a negative potential relative to the inner cylinder. For a specific potential difference, only electrons with a well defined energy will be deflected into the exit aperture and contribute to the spectrum. As the potential difference between the cylinders is changed in discrete steps, the CMA analyzes different electron energies, and a full energy spectrum is obtained. The collection angle of the CMA in the SAM - 595 is about 42°. This angle is usually used since the instrument is then a second-order focussing device (38, p. 76). This collection angle effectively decreases the mean free path by a factor of cos42°.

The SAM is very versatile and can be operated in several different modes which include: mapping surface topography, surveys, Auger line scans, Auger maps, and depth profiling. These will, in turn, be described below.

2.3.1 Surface Topography

The SAM monitors surface topography by measuring either secondary electrons emitted from the surface or the current absorbed by the sample, as the incident electron beam is rastered over a selected area of the sample. The secondary electrons range in energy from 0 eV to the incident electron beam energy. Thus the escape depth of these electrons is not restricted to the outermost layers of the sample, and actually come from as deep as 100 Å below the surface (38, p. 186). The image, displayed on a screen, gives a visual picture of the surface topography with sub-micron resolution.

2.3.2 Surveys

A general procedure in Auger analysis is to first select an area of the sample of interest. This area is usually determined by a visual examination of the secondary electron image. An Auger survey is then done in which an energy spectrum, that is the number of electrons collected vs. energy (N(E) vs E), is measured. The spectrum consists of Auger peaks superimposed on a large background. The peaks tend to be quite small, however on the differentiated spectrum, dN(E)/dE vs E, they are more pronounced. For this reason the differentiated spectrum is the conventional way of displaying survey spectra. Elemental identification is obtained by comparing the observed Auger peak positions to the known peak positions of the different elements (41). The heights of the differentiated peaks, when divided by empirical "sensitivity factors" (41, p. 13), give quantitative information on the concentration of elements present on the sample surface. The sensitivity factors depend on such factors as the incident electron beam current and energy, the transition probability of the Auger transition involved, and the collection efficiency of the Auger electron analyzer.

Surveys may be performed over a large area of the crystal by rastering the incident electron beam, or in point mode in which the beam is stationary on a selected point of the crystal.

Survey spectra are an essential first step for determining which elements are present on or near the sample surface.

2.3.3 Auger Line Scans

In line scan mode, the electron beam is directed, in a point by point

fashion, along a straight line across the sample surface. Only those electrons (emitted from the sample) occuring at operator-selected Auger peak energies are analyzed. Since one element can have more than one Auger peak (41), the peaks selected are usually the strongest peak for a particular element. The result is a plot of the relative concentration (at each point) of the selected elements as a function of distance across the sample surface. One can do as many as five line scans at one time, giving two-dimensional information of the elemental concentration.

2.3.4 Auger Maps

A more effective method of obtaining two-dimensional information is with an Auger map. Again only electrons with specific Auger peak energies are analyzed. The electron beam is rastered, point by point, across an area of the sample surface, and the elemental concentration at each point is recorded. This is, in effect, just many line scans. The data are displayed as a multi-level grey scale picture on an oscilloscope screen, with different levels of grey corresponding to different concentrations. The result is a direct visual image, which can be more enlightening than a series of graphs that result from several line scans.

2.3.5 Depth Profiling

Depth profiling in AES is achieved by bombarding the sample with inert gas ions. The ions are usually inert so that they do not react chemically with the surface, and only "billiard ball" type collisions result. These ions have sufficient energy to knock off atoms from the sample surface. This process, known as sputtering, can be combined with

AES in order to measure elemental concentrations as a function of depth.

Sputtering in the SAM is obtained using a Differentially Pumped Ion Gun (DPIG). With the DPIG, inert gas atoms (usually argon) enter the ion gun through a precisely controlled leak valve. Here the atoms are ionized via collisions with energetic electrons. The resulting positive ions are then directed down a long slender tube toward the sample. The ion beam is focussed with a set of condenser and objective lenses, and the minimum beam diameter is about 200 μm. The sputtering rate depends of the material and can be adjusted by changing the ion beam current and/or energy. For example, the sputtering rate for Ag/TiS_2 is about 120 Å/min using an ion beam voltage of 3 kV and an emmision current of 25 mA.

Fig. 2.1 Energy level diagram describing the Auger process. This figure represents an ABC transition.

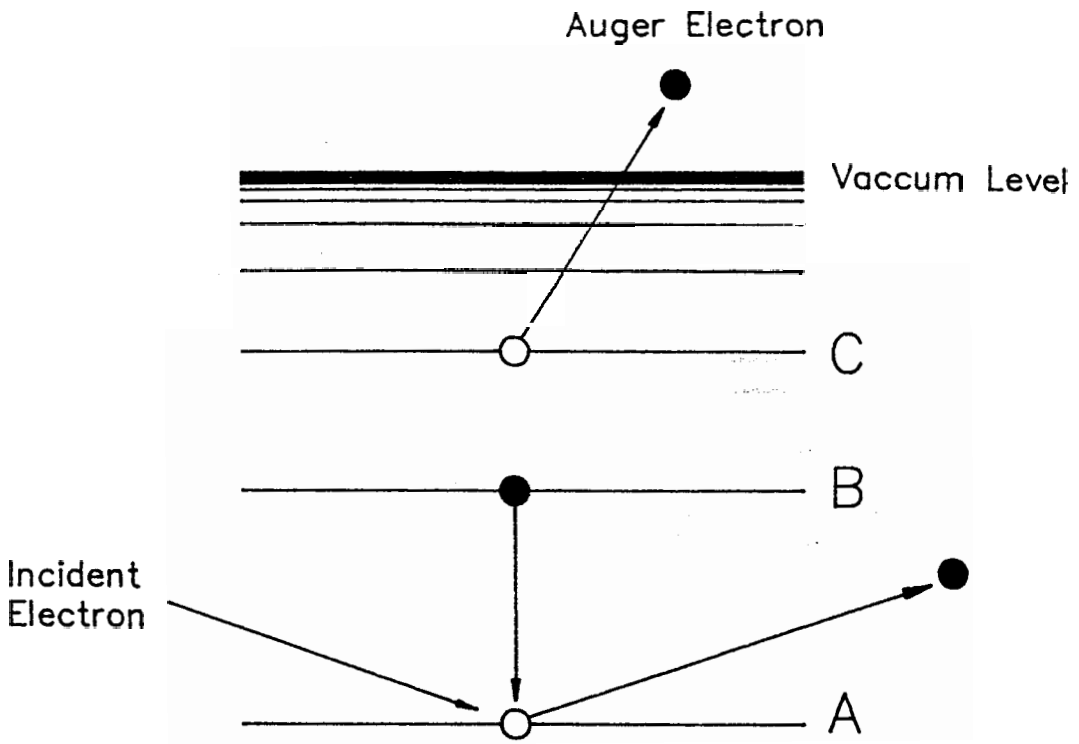

Fig. 2.1

Fig. 2.2 Schematic graph of the electron escape depth versus the electron energy (ref. 38).

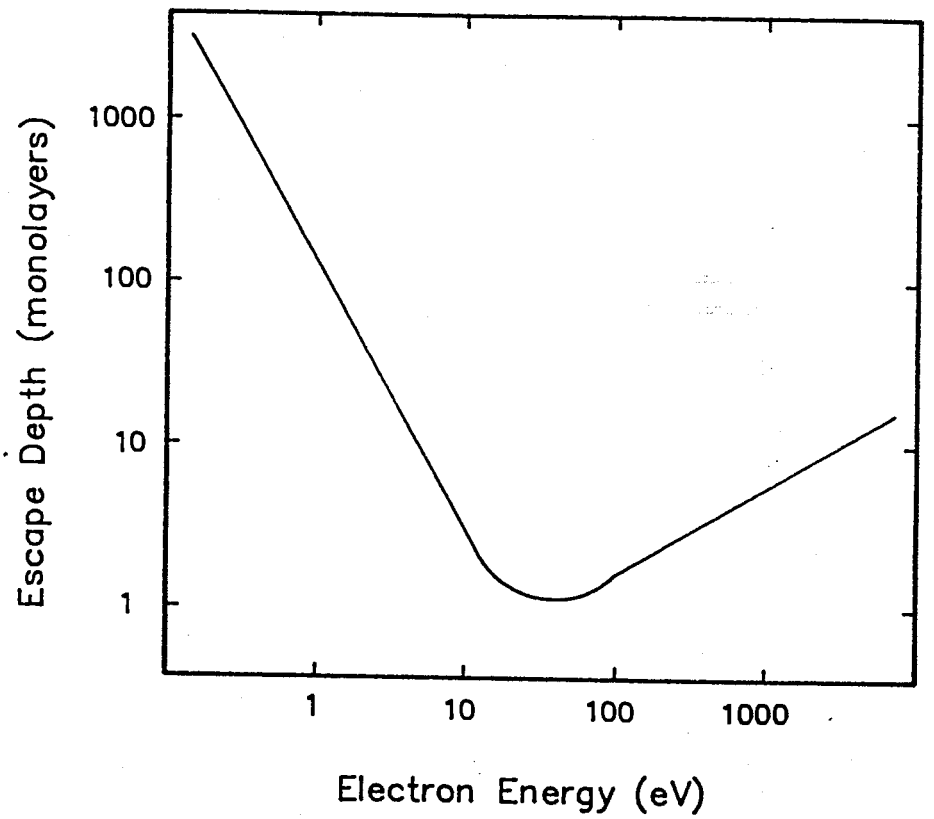
Escape Depth (monolayers)
1000
100
10
1
1
10
100
1000
Electron Energy (eV)

Fig. 2.2

Fig. 2.3 Schematic drawing of the SAM instrumentation. Shown are the coaxial electron gun, electron focussing lenses, and the cylindrical mirror analyzer (ref. 40).

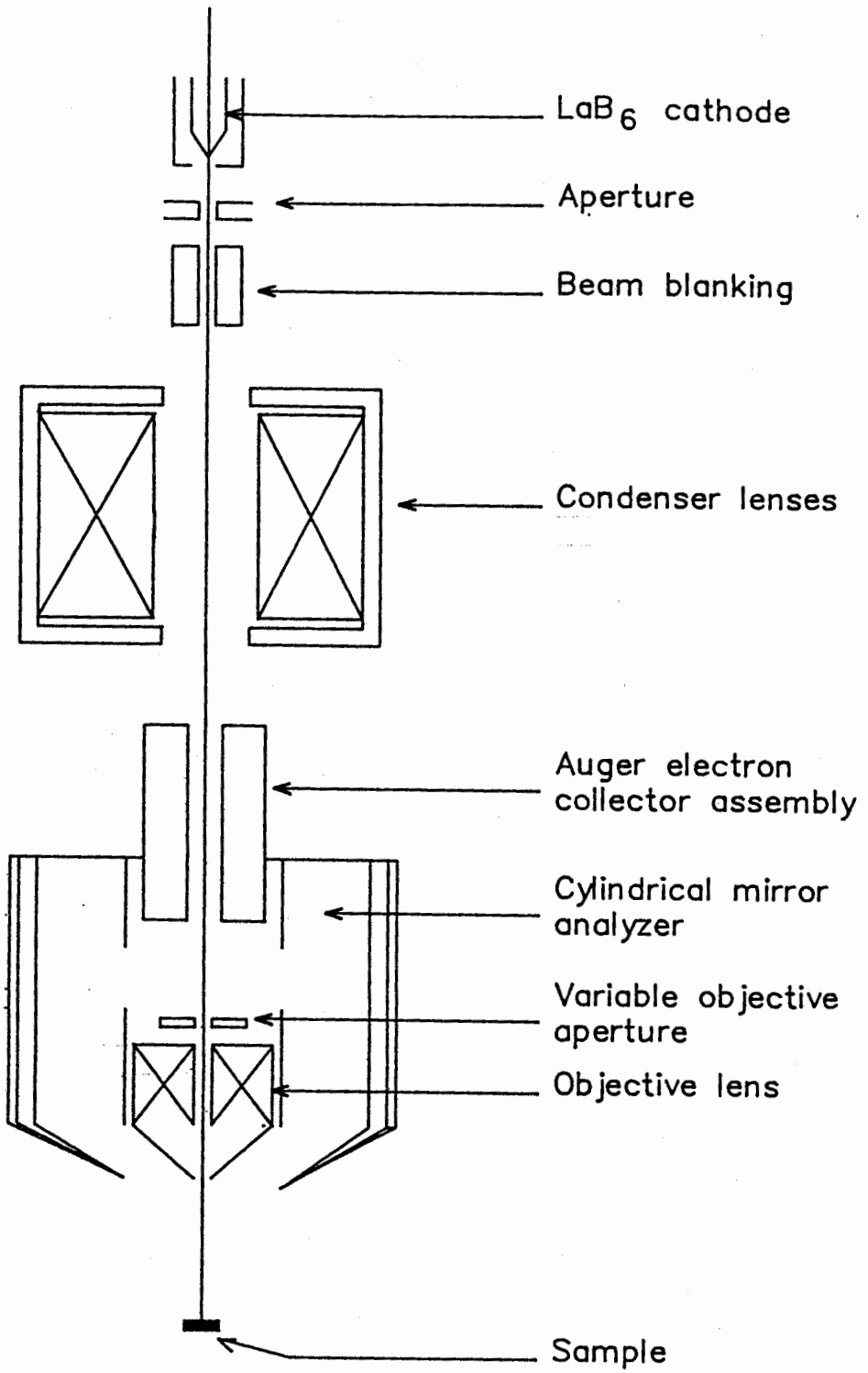
LaB6 cathode
Aperture
Beam blanking
Condenser lenses
Auger electron collector assembly
Cylindrical mirror analyzer
Variable objective aperture
Objective lens
Sample

Fig. 2.3

Fig. 2.4 Dependence of the electron beam diameter on the electron beam current in the SAM-595 (ref. 40).

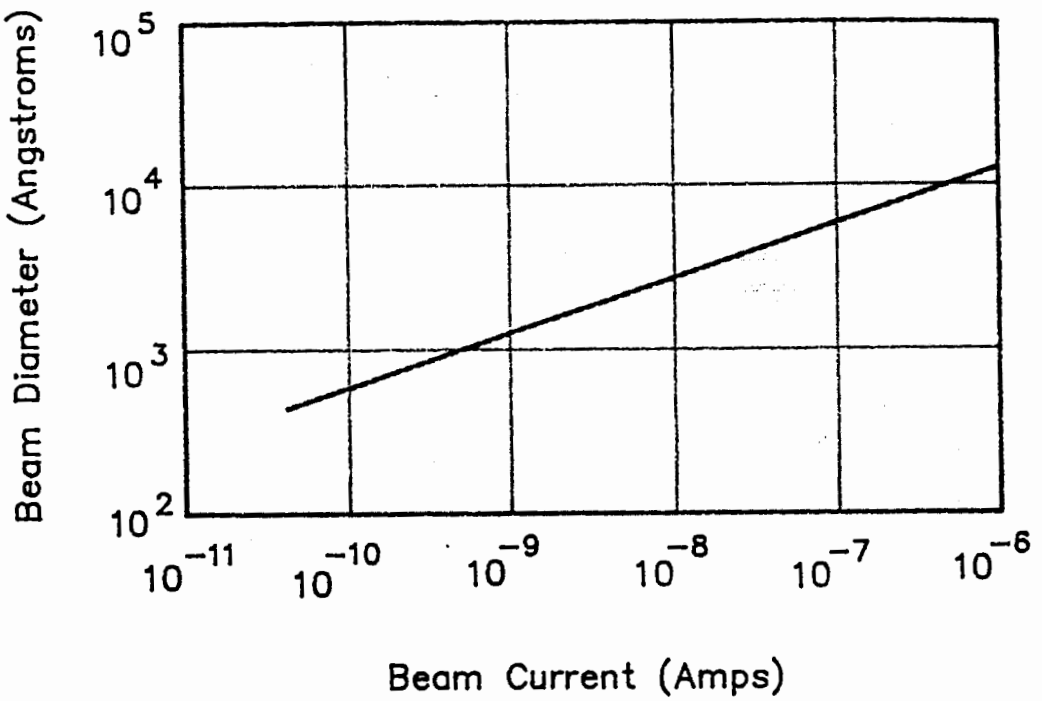
Beam Diameter (Angstroms)
10^5
10^4
10^3
10^2
10^{-11}
10^{-10}
10^{-9}
10^{-8}
10^{-7}
10^{-6}
Beam Current (Amps)

Fig. 2.4

Fig. 2.5 The trajectory of Auger electrons in the cylindrical mirror analyzer. The outer cylinder is at a negative potential relative to the inner cylinder.

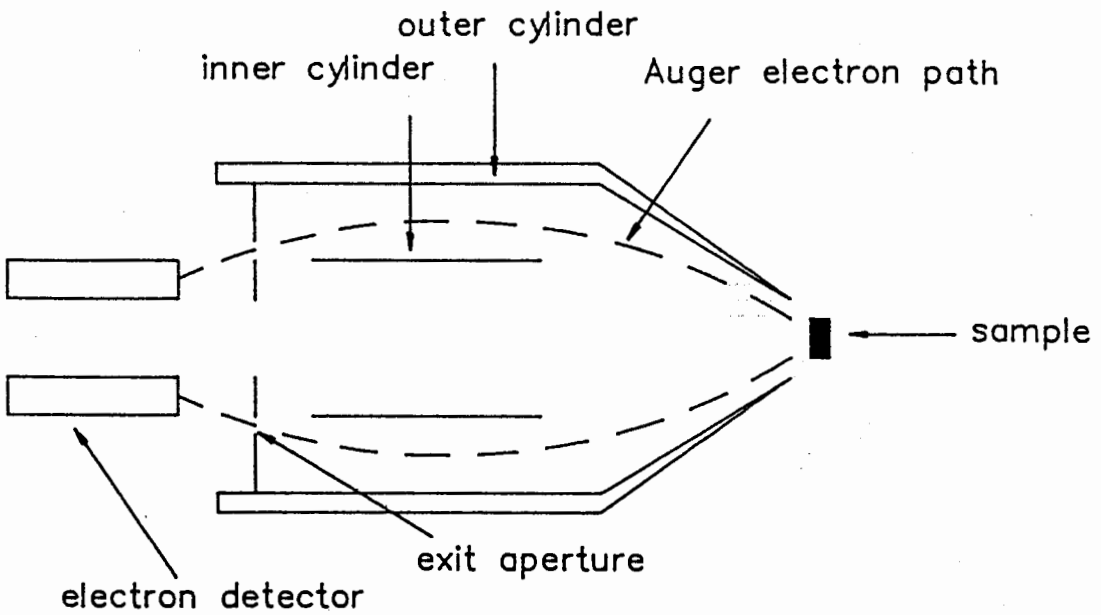
outer cylinder
inner cylinder
Auger electron path
sample
exit aperture
electron detector

Fig. 2.5

CHAPTER 3

SAMPLE PREPARATION

3.1 ELECTROCHEMICAL INTERCALATION OF TiS_2 WITH Ag

All TiS_2 crystals were intercalated with Ag by using an electrochemical cell depicted in Figure 3.1. The cell consists of a TiS_2 single crystal cathode and a piece of pure Ag metal as the anode. These are immersed in an electrolyte of 0.05M $AgNO_3$ in water. An open circuit voltage of about 100 mV is observed. Upon connecting the external circuit, intercalation proceeds via the following reactions:

$xAg \longrightarrow xAg^+ + xe^-$ at the anode,

$TiS_2 + xAg^+ + xe^- \longrightarrow Ag_xTiS_2$ at the cathode,

$xAg + TiS_2 \longrightarrow Ag_xTiS_2$ net reaction,

where x is the mole fraction of Ag.

By varying the external potential, different intercalation systems can be created. These systems are determined by the E vs. x dependence of Ag_xTiS_2 as depicted in Fig. 3.2. Here, E is the electrode potential and x is the mole fraction of Ag. From the figure:

(a) for $x \approx 0$, $E \approx 100$ mV and corresponds to an empty TiS_2 crystal.

(b) for $x \approx 0.2$, $E \approx 50$ mV and corresponds to stage-2.

(c) for $x \approx 0.42$, $E \approx 0$ mV and corresponds to stage-1.

(d) for x falling in between any of the above values, a mix of stages occurs.

These x values for stage-1 and stage-2 do not apply only for a uniformly itercalated crystal that has reached equilibrium. X-ray Fluorescence studies of the silver concentration for stage-1 and stage-2 during

intercalation and stage transformation gave similar x values (27).

The work in this thesis used different intercalation systems. Four of these of these, referred to as Types I, II, III, and IV will now be discussed in detail.

Type I: Stage-2 obtained by the conversion from stage-1.

With the external voltage set at V=0 (a short circuit), the intercalation of Ag into a crystal edge proceeds as shown in Figure 3.3(a). A band of stage-2 (x = 0.2) propagates in from the crystal edge followed by a band of stage-1 (x = 0.4). The three regions of the crystal, being stage-1, stage-2 and empty crystal, are separated by well defined fronts. The widths of the stage-1 and stage-2 regions are approximately equal, with each growing wider as intercalation continues. The speed of intercalation for thin (about 1 μm) crystals is several microns per hour. Figure 3.4 shows a picture of a TiS_2 crystal during this intercalation process. The picture was taken with reflected light under an optical microscope. The stage-1, stage-2 and empty crystal regions are clearly visible. If intercalation is stopped (i.e. open circuit) when the crystal appears as in Fig 3.3(a), the stage-1 region, which is unstable at room temperature (except for a fully intercalated stage-1 crystal), converts to stage-2 at a rate of several microns per hour. The resulting system, shown in Figure 3.3(b), is entirely stage-2, followed by the empty TiS_2 crystal. For uncleaved crystals the stage-2/empty crystal front is stable up to temperatures of about 150°C (42). (Results in this thesis indicate that partially intercalated, cleaved crystals are not stable). This stage-2 system was created by the conversion from stage-1.

Type II: Stage-1.

Again with V = 0, the intercalation is allowed to proceed beyond the configuration shown in Fig 3.3(a). As intercalation continues the bands of stage-1 and stage-2 grow wider until, eventually, approximately half of the crystal is stage-1 and the other half is stage-2. Then the stage-1 region grows wider at the expense of the stage-2 region, and after intercalation for a few days, the crystal is intercalated entirely to stage-1.

Type III: Direct stage-2 intercalation.

With V ≈ 50 mV, no stage-1 band is seen propagating in from the crystal edge, only a stage-2 band is observed, as is expected from the E vs. x curve in Fig. 3.2. Thus, the crystal intercalates directly as stage-2.

Type IV: Deintercalation to stage-2.

Again with V = 0, the system is intercalated to a configuration as is Fig. 3.3(a). Then setting V ≈ 160 mV the crystal begins to deintercalate. The deintercalation proceeds as a new stage-2 region propagating in from the crystal edge as shown in Figure 3.3(c). This new stage-2 region grows at the expense of the stage-1 region, until the stage-1 region has converted completely to stage-2 (Figure 3.3(d)). No further deintercalation occurs when using water as solvent; the system remains as stage-2 and cannot be emptied further. (When using acetonitrile as a solvent, complete deintercalation does occur (43)). The stage-2 system consists of two portions, one obtained from the conversion of stage-1 during intercalation (part 1 of the crystal in Fig. 3.3(d)) and the other from the conversion of stage-1 during deintercalation (part 2 of the crystal in Fig. 3.3(d)). In order to obtain a complete stage-2 system by

the conversion from stage-1 during deintercalation only, the system must be fully intercalated to stage-1 prior to deintercalation.

The motion of Ag within the host layers during intercalation has been extensively studied by Kaluarachchi and Frindt (20) using combinations of radioactive Ag^{110} and non radioactive Ag^{108}. Their results indicated that newly intercalated Ag atoms reside mainly near the edge of the crystal. These atoms move farther into the crystal only upon subsequent intercalation, and do not overtake previously intercalated atoms. Thus the atoms at the intercalation front were intercalated first and those near the crystal edge, last. No such work has been performed on deintercalation systems.

3.2 SAMPLE PREPARATION

Pure TiS_2 crystals, provided by Per Joensen, were prepared by the standard iodine-vapor-transport method (33,34). These crystals had lateral dimensions of 1 to 2 mm and thicknesses ranging from 10 to 100 μm. The stoichiometry of the crystals was determined by the c-axis spacing (44), measured by X-ray diffraction analysis. The crystals used for experiments were obtained from four separately prepared batches (batches K, L, M, and N). All crystals prepared had an average ratio of sulfur to titanium of $2 \pm 0.05 : 1$.

For crystals thicker than about 10 μm, intercalation can be extremely slow and the crystals tend to crack during the intercalation process (42). To obtain thinner crystals, the as-grown crystals were mounted on half-set 5 minute epoxy. Once the epoxy was fully cured, thin crystals were peeled

off (known as cleaving) with DRG Sellotape, resulting in a 1-3 μm crystal stuck to the tape. A single as-grown crystal can be cleaved many times. The cleaved crystals were removed from the tape immersing them in a bath of trichloroethylene for about 30 minutes. This bath dissolves the tape gum, releasing the crystals from the tape. The crystals were then washed in a fresh bath of trichloroethylene and then finally in methanol (in order to remove any residual tape gum), and then placed on 18 mm circular glass cover slips. It is very important to use a compatible combination of tape and solvent in which the solvent properly dissolves the tape gum. A poor combination can result in tape gum remaining on the crystals and ultimately can inhibit the intercalation process. The thicknesses of the cleaved crystals were measured using a Wild M 20 optical microscope with an interference attachment.

An intercalation cell, as described in Section 3.1, was constructed as shown in Figure 3.5. A copper wire is attached to the crystal (which is mounted on the glass cover slip) using Ag dag. The wire and dag are then covered completely with RTV Self-Leveling 734 Silicone Sealant, and only selected edges of the crystal were exposed. A hollow glass cylinder, 18 mm in diameter, was mounted on the cover slip with more RTV. Once the sealant was fully cured a piece of pure Ag metal was then draped over the edge of the cell and an electrical connection was made between the copper wire and the Ag metal. With an external voltage applied, the cell was filled with electrolyte and intercalation proceeded by one of the methods outlined in Section 3.1. Only the edges of the crystal exposed to the electrolyte can intercalate. Intercalation was continued for several hours or until the desired width of the intercalated region had been obtained. Once

intercalation was stopped, the electrolyte was removed and the cell was rinsed out with methanol and distilled water in order to remove any remaining electrolyte. The removal of the intercalated crystal from the cell, which is a delicate procedure, was done with the use of a scalpel, fine forceps, or even the freyed end of a toothpick, whichever instrument facilitated the removal of the crystal.

This sample preparation procedure was very tedious and many samples were destroyed at every stage in the process. However, through much practice, the number of successful samples greatly increased.

3.3 SAMPLE MOUNTING

The intercalated crystals have dirty surfaces due to the long and messy sample preparation procedure. To obtain Auger results on a clean surface, the intercalated crystals required cleaving. Small copper substrates, cut to an appropriate size for SAM sample holders, were cleaned in a bath of methanol. When dry, a small drop of 5 minute epoxy was put on the substrate and an intercalated crystal was placed on the half-set epoxy. When the epoxy was fully cured, the crystal was cleaved, in air, with scotch tape, and the half of the crystal remaining on the substrate was used for Auger analysis. The half remaining on the tape was usually discarded. The direction of cleaving was from the unintercalated region of the crystal to the intercalated region of the crystal since the crystals tended to cleave best in this direction. The epoxy is non-conducting so an electrical connection was made from an unintercalated edge of the crystal to the copper substrate using graphite dag. This was required to prevent electrical charging of the sample during Auger analysis. The substrate,

with the freshly cleaved crystal attached, was mounted on a 90° SAM sample holder, illustrated in Figure 3.6.

This entire process was performed with very clean instruments in order to avoid contaminating the sample and/or sample holder. This is essential when working with the ultra-high vacuum used in AES.

Cleaving the intercalated crystals was very difficult. The crystals are already very thin (about a micron) and the success rate of cleaving these crystals, such that a smooth surface was exposed was probably about one in five (at best). This was incredibly frustrating in that nearly 80% of crystals were effectively destroyed in the last step before Auger analysis. Patience was the only recourse; however, this was frequently lost.

3.4 THE CLEAVING ASSUMPTION

Before presenting the results, it is vital to discuss in more detail the cleaving of the intercalated crystals. This is important since the goal of this thesis is to infer bulk intercalant distributions using a surface probe. One must, therefore, be confident that the surface intercalant distributions can, in some way, infer the bulk distributions.

Consider a stage-2 domain model as shown in Figure 3.7(a). Upon cleaving at the gallery indicated, two new surfaces are created and the question arises: Where does the intercalant in the cleaved gallery go when the crystal is cleaved? At this point, the answer to the question will be assumed to be: <u>due to the symmetry of the cleaving process, it is expected that the intercalant in the cleaved gallery divides equally on an atomic scale upon cleaving</u>. This "cleaving assumption" is illustrated in Figure

3.7(b). Results expected from this assumption include:

(i) surface islands are, on average, one half the concentration of bulk islands. A surface island is defined as a Ag occupied region on the newly created surface.

(ii) the lateral size and shape of the surface islands is the same as the bulk islands.

(iii) the islands on one side of the cleaved gallery are in the same location as the islands on the other side of the cleaved gallery.

(iv) from a "macroscopic" point of view, that is on a scale comparable to the lateral island size, the area of the surface Ag occupied regions equals the area of the surface Ag unoccupied regions.

As can be seen, if the cleaving assumption is correct, surface analysis would yield directly the bulk intercalant domain structure. This cleaving model is assumed because on the surface (no pun intended) it seems to be the most realistic.

Other possible cleaving models are (a) that the surface islands of Ag are not stable and either redistribute on the crystal surface or leave the crystal surface entirely, or (b) that the Ag does not divide equally on an atomic scale upon cleaving, resulting in a complicated surface island structure.

A large part of the work in this thesis was spent proving that the observed surface results are related to the bulk domain structure. The cleaving assumption will be frequently referred to throughout the remainder of this thesis.

Fig. 3.1 Schematic of an Ag/TiS_2 electrochemical intercalation cell. The potential between the electrodes is controlled to obtain different intercalation systems.

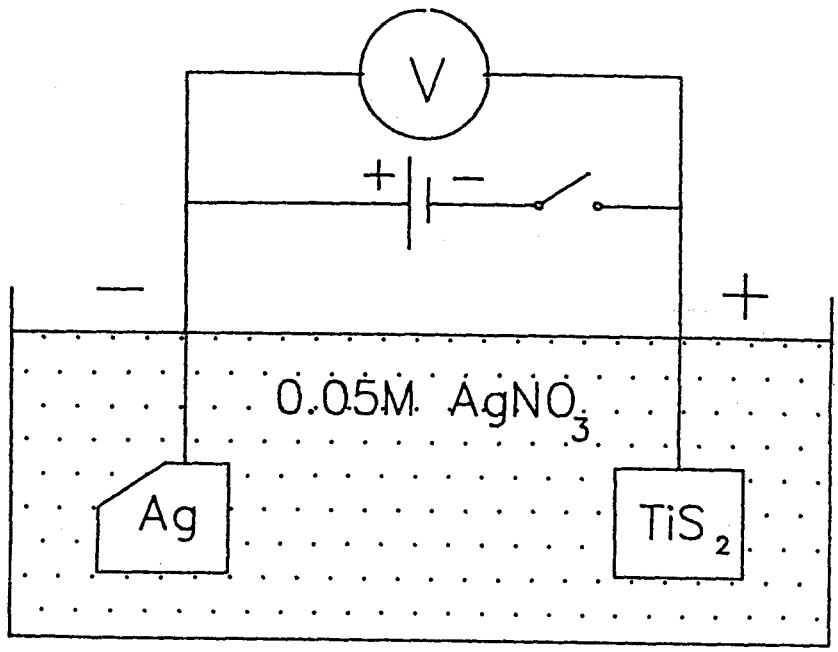

Fig. 3.1

Fig. 3.2 Approximate plot of the open circuit potential of an Ag_xTiS_2/0.1M $AgNO_3$/Ag electrochemical cell versus the Ag fraction, x. The different stages are shown (ref. 36).

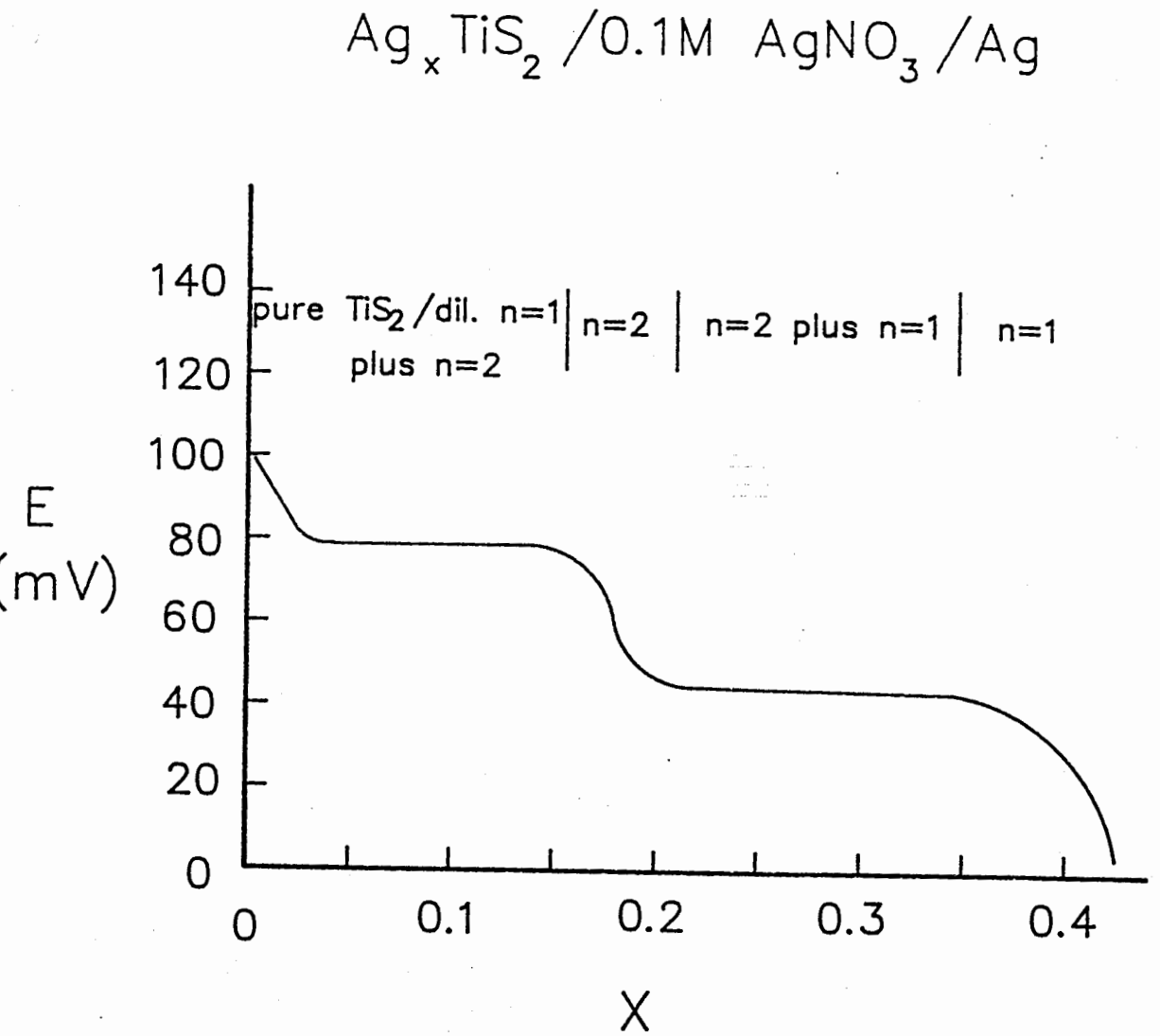
Ag_xTiS_2 /0.1M $AgNO_3$ /Ag
pure TiS_2 /dil. n=1 plus n=2
n=2
n=2 plus n=1
n=1
E (mV)
140
120
100
80
60
40
20
0
0
0.1
0.2
0.3
0.4
X

Fig. 3.2

Fig. 3.3 Schematic showing the different intercalation systems created in Ag/TiS_2 by varying the potential between the Ag and TiS_2 electrodes (see text).

(a) Short circuit intercalation.

(b) Conversion of stage-1 (from (a)) to stage-2.

(c) Partial conversion of stage-1 (from (a)) to stage-2 during deintercalation.

(d) Complete conversion of stage-1 (from (a)) to stage-2 during deintercalation. Part 1 of the stage-2 region was created during intercalation, while part 2 of the stage-2 region was created during deintercalation.

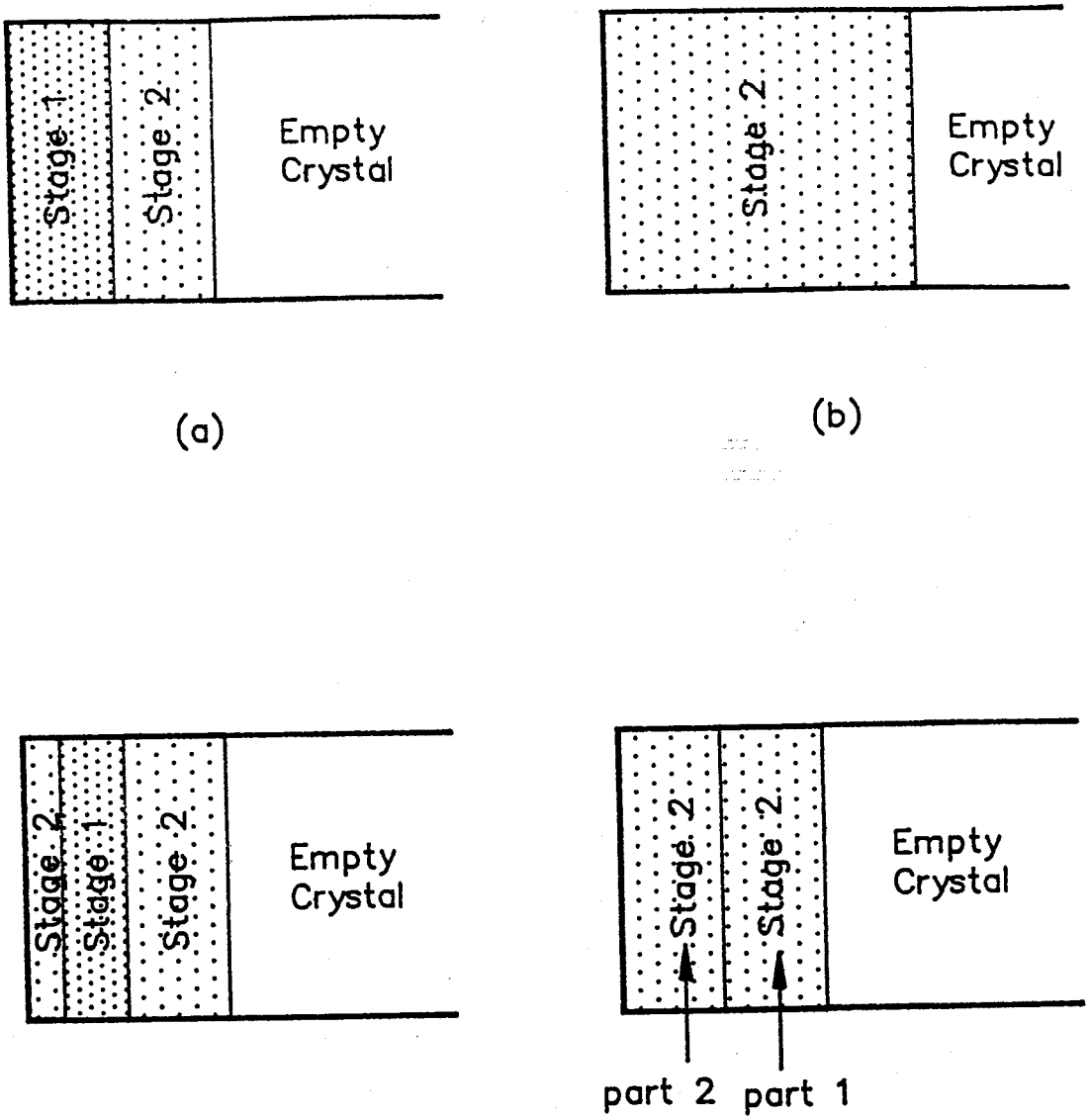
Stage 1
Stage 2
Empty Crystal
(a)
Stage 2
Empty Crystal
(b)
Stage 2
Stage 1
Stage 2
Empty Crystal
(c)
Stage 2
Stage 2
Empty Crystal
part 2
part 1
(d)

Fig. 3.3

Fig. 3.4 Optical photograph of a partially intercalated TiS_2 crystal (from ref. 42, with permission).

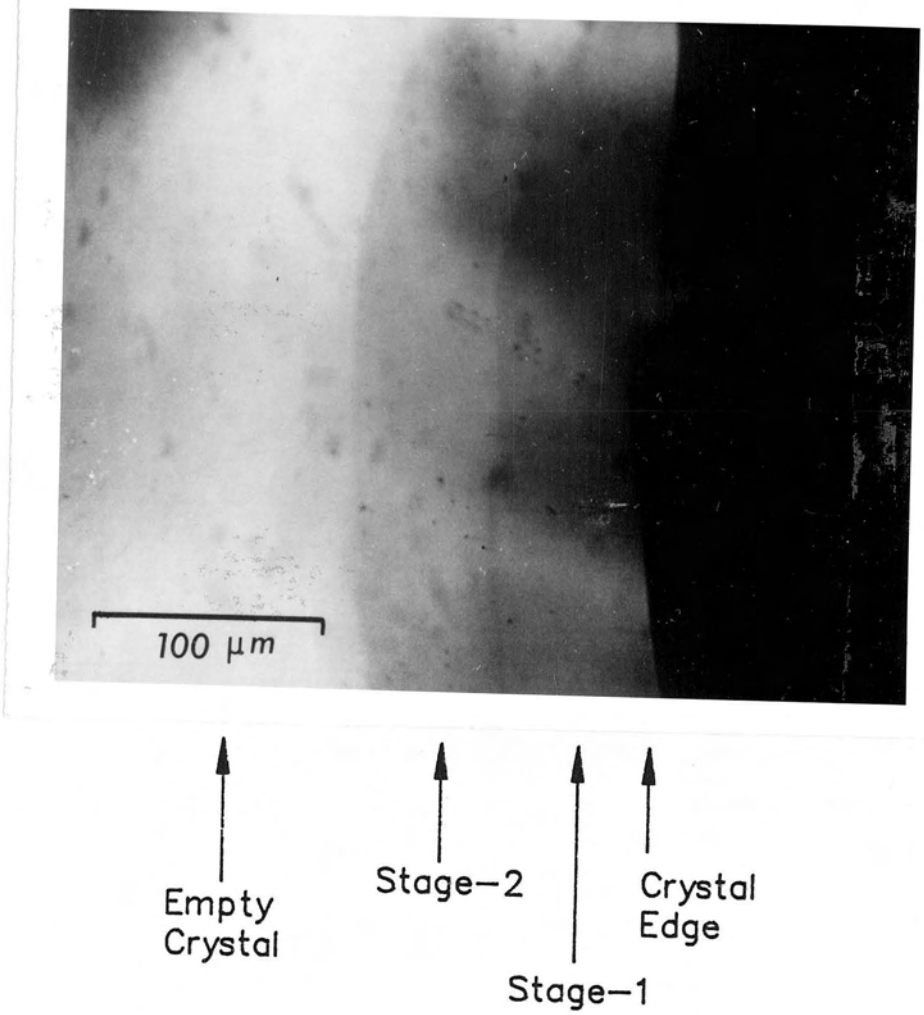

Fig. 3.4

Fig. 3.5 Schematic of the actual Ag/TiS_2 electrochemical cell.

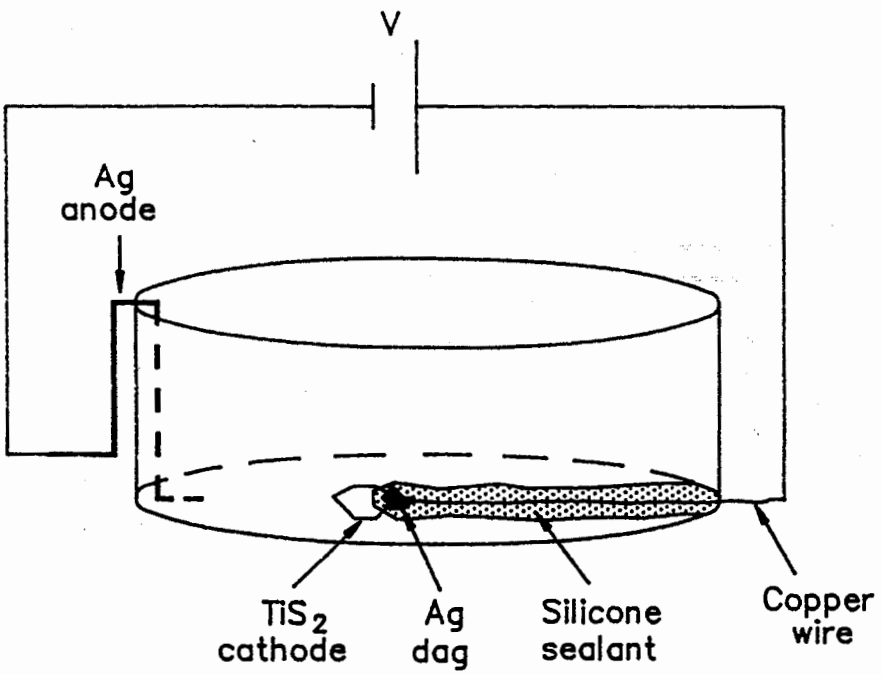

Fig. 3.5

Fig. 3.6 Ag/TiS_2 sample mounted on a SAM sample holder.

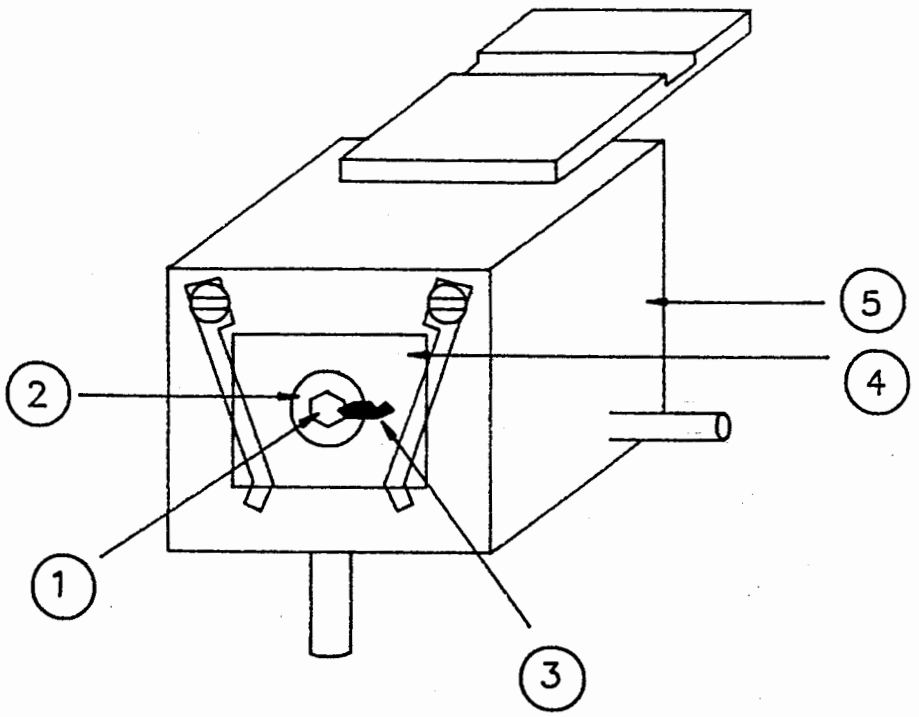

(1) Ag/TiS_2 crystal

(2) 5-minute epoxy

(3) Graphite DAG

(4) Copper substrate

(5) SAM sample holder

Fig. 3.6

Fig. 3.7 Schematic of the cleaving assumption.

(a) The stage-2 domain model. The crystal is cleaved in the gallery indicated.

(b) The resulting distribution of intercalant in the cleaved gallery is based on the cleaving assumption (see text).

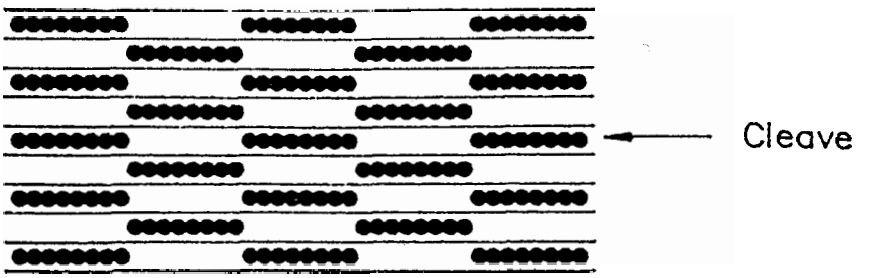

(a)

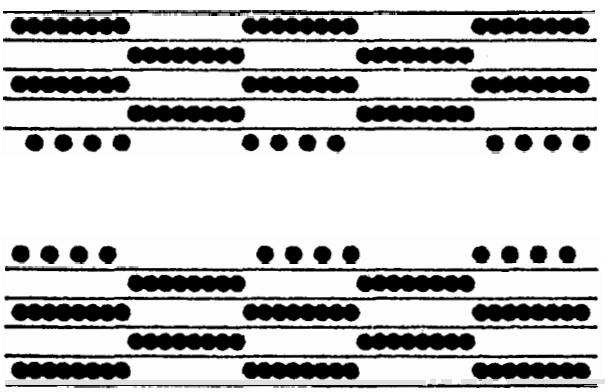

(b)

Fig. 3.7

CHAPTER 4

AUGER RESULTS

4.1 PRELIMINARY SET-UP

A freshly cleaved intercalated crystal, mounted on a SAM sample holder, was immediately inserted into the UHV chamber of the SAM. The sample was positioned in front of the electron beam, whose energy was set at 3 keV. The 90° sample holder positions the crystal so that its cleaved surface is normal to the incident electron beam. Precise sample movement was achieved with a set of three micrometers which could move the sample in the x, y, and z directions. This is illustrated in Figure 4.1. The electron beam current was set typically at about 20 nA, corresponding in a beam diameter of about 0.3 μm (see Fig. 2.4).

A selected portion of the crystal was positioned in front of the electron beam by monitoring the secondary electron image on the video screen. Figure 4.2 is a photograph of such an image, with the crystal edge and the intercalation front clearly visible. Increasing (decreasing) the magnification permits a smaller (larger) area of the sample surface to be analyzed.

4.2 AUGER SURVEYS

A typical Auger survey spectrum of the freshly cleaved surface of a stage-2 Ag intercalated TiS_2 crystal is shown in Figure 4.3. The spectrum is a plot of N(E)*E vs. E, where E is the electron energy and N(E) is the number of electrons with the energy E. As can be seen, the spectrum consists of a large continuous, sloping background upon which Auger peaks are superimposed. These peaks, when compared to the known positions of

peaks for different elements, are identified as the figure shows. The specific Auger peak transitions and energies of these peaks are (41):

Element	Auger peak energy (eV)	Auger transition
Sulfur	152	KLL
Carbon	272	KLL
Silver	351	MNN
Titanium	387 , 418	LMM , LMM
Oxygen	508	KLL

Even though oxygen does not appear in Fig. 4.3, it is included in the table since it is sometimes present in small amounts. The Ag peak is seen to be extremely small. Although great care was always taken to avoid contamination of the sample surface, carbon almost always seemed to be present in small amounts. Any samples with gross contamination were not examined further.

Figure 4.4 shows the differentiated survey spectrum. This view of the data makes the Auger peaks more pronounced, particularly the Ag. Surface stoichiometry can be determined approximately by the heights of the differentiated Auger peaks, divided by appropriate sensitivity factors. These factors for Ag, S, and Ti are 0.95, 0.9, and 0.45 respectively (41). From this Auger survey spectrum, the stoichiometry of the sample surface, ignoring carbon, is about $Ag_{.18}TiS_{2.5}$. This is not the expected $Ag_{.2}TiS_2$ since the stoichiometry method is very crude, particularly since the sensitivity factors are based on a homogeneous sample. Stage-2 Ag intercalated TiS_2 crystals are not homogeneous due to their layered

structure.

4.3 INTERCALANT DISTRIBUTIONS

Intercalant distributions on the cleaved surfaces of crystals were determined through combinations of Auger line scans and Auger maps. The position of a line scan or map was determined by inspection of the secondary electron image. These positions were chosen only where the secondary electron image showed a flat surface, void of any visible steps, cracks, or any other topographical features. To scan for a particular element an energy window is selected around the Auger peak of interest, and during the scanning procedure, only electrons in this window are counted. A detailed explanation of the parameters chosen for line scans and maps is given in Appendix A.

Different types of intercalation systems were analyzed. These types were described in Section 3.1 and for convenience, are repeated here.

Type I: intercalated to stage-2 via the conversion from stage-1.

Type II: intercalated completely to stage-1.

Type III: direct stage-2 intercalation.

Type IV: deintercalated to stage-2 via the conversion from stage-1.

4.3.1 Intercalation Into a Crystal Edge

Figure 4.5 is an Auger line scan showing the relative concentrations of S, Ti, and Ag as a function of distance as measured along a straight line across the surface of a stage 2 (Type I) crystal. The direction of this line scan was nominally perpendicular to the crystal edge (however, Auger maps show that the scan direction is most likely not exactly

perpendicular to the edge). The data were obtained by a series of point measurements taken 0.7 μm apart. As can be seen in Fig. 4.5, at a distance of about 30 μm from the crystal edge the Ag distribution consists of a series of maxima and minima on a scale of about 10 to 15 μm, and both the S and Ti distributions are clearly anti-correlated to the Ag distribution. Small-scale variations within the Ag and Ti distributions are considered to be noise. The anti-correlation of S and Ti with Ag shows that the Ag oscillations are not caused by contamination on the crystal surface. Any carbon or oxygen on the crystal surface was found to be distributed uniformly.

The cleaving assumption, discussed in Section 3.4, states that the Ag in the cleaved gallery divides equally on an atomic scale upon cleaving. The interpretation of this line scan data, in terms of the cleaving assumption, is that the Ag maxima correspond to surface islands of Ag with a concentration equal to one-half the bulk Ag island concentration (see Fig. 3.7(b)). This view is supported by the ratio, R, of the Ag maxima to the Ag minima from Fig. 4.5. The data in Fig. 4.5, when averaged over the four maxima and minima extending from 30 μm to the intercalation front gives R=1.7 $\pm$ 0.2. Theoretically, the Auger signal, I, from a layer of Auger emitting atoms m+1 layers below the crystal surface varies as (45)

$$I \approx N_{m+1} \prod_m (1-X_m+X_m \exp[-1/\sigma\cos(\theta)]) \qquad (4.1)$$

where: N_{m+1} is the concentration of atoms in the Auger emitting layer, σ is the escape depth of Auger electrons measured in monolayers, and θ is the angle (with respect to the crystal surface normal) at which the Auger electrons are collected. The product, $\prod_m$, is carried out over all m

atomic layers between the Auger emitting layer and the crystal surface, and X_m is the fraction of a monolayer in the atomic layer m. For the energy of the Ag Auger electrons the value of σ is about 3.9 ± 1 monolayers (38, p. 186), and for the SAM-595, Θ is 42 degrees. Referring to Fig. 3.6(b): each host layer consists of a S-Ti-S sandwich and so is equivalent to three atomic layers, and each atomic layer is one complete monolayer; the subsurface islands in stage-2 Ag/TiS_2 (i.e. $Ag_{.4}TiS_2$) are equivalent to 0.4 of a monolayer and the surface islands, due to the cleaving assumption, are equivalent to 0.2 of a monolayer. Using this model and summing the Auger signals from all islands within domains to obtain the maximum and minimum Ag Auger signals gives R=1.6 with an uncertainty of +0.5 and -0.2. Calculations using a model with no surface Ag (or with the surface island concentration equal to the subsurface island concentration) gives R=2.8 with an uncertainty of +1.2 and -0.5. Thus, the model based on the cleaving assumption provides the best agreement with the observed experimental ratio of 1.7. Note that the value of R provides information not just on the surface Ag, but also on the intercalant distribution a couple of galleries deeper into the crystal. The asymmetric uncertainties in the theoretical values of R are due to substituting the rather large uncertainty in σ into the exponential form of Eq. 4.1.

Similar ratios can also be calculated for sulfur and titanium where the escape depths of the Auger electrons are $\sigma_S \approx 2.5$ and $\sigma_{Ti} \approx 4$ (38). However, due to the large amount of these elements present (as compared to Ag) the ratios are not very sensitive to the different models. Theoretical values of R for S, Ti, and Ag, for the different models, along with the experimentally observed values are all shown below.

Model	R_{Ag}	R_S	R_{Ti}
1. no surface Ag	2.8	1.03	1.04
2. surface island conc. equal to bulk island conc.	2.8	1.23	1.12
3. surface island conc. one-half of bulk island conc.	1.6	1.09	1.04
experimental values	1.7	1.05	1.06

Table 4.1. Relative Auger intensities for cleaved Ag/TiS_2 surfaces. The ratios, R (defined in text), for different cleaving models, and the experimentally observed values. Model 3 agrees with the results.

Auger maps were used to determine the two-dimensional distribution of Ag on cleaved crystal surfaces. Either the Ag distribution can be measured directly or the S (or Ti) distribution can be measured and the Ag distribution inferred from its anti-correlation to the S (or Ti). The advantage of measuring the S distribution is that, due to its strong Auger signal as seen in Figs. 4.3 and 4.4, much shorter data acquisition times can be obtained. On the other hand the oscillations of the S signal, as seen in Fig. 4.5, are much smaller than the Ag oscillations. This results in a S map having less contrast than a Ag map. The need for short data acquisition times, which is discussed in Section 4.4, requires the Ag distribution to be inferred from a S map.

Figure 4.6(a) is a S map of another stage-2 (Type I) crystal. The map was obtained by a series of point measurements taken 1.7 μm apart in both directions. Light-colored regions correspond to a strong S Auger

signal and dark-colored regions correspond to a weak S Auger signal. The opposite is true for Ag since it is anti-correlated to the S. Thus Fig. 4.6(a) shows that the Ag distributions consists of a series of "channels" which extend from the crystal edge to the intercalation front. They are approximately perpendicular to the crystal edge. The width of the channels is about 5 μm and the period of the channels is about 10 μm. Figure 4.6(b) is a computer enhanced version of Fig. 4.6(a) and it clearly shows the channel-like structure. Some channels appear to meander and divide as they extend in from the crystal edge toward the intercalation front. Note that the area of the Ag occupied regions is approximately equal to the area of the Ag unoccupied regions, consistent with a stage-2 structure.

An Auger map of S should be accompanied by at least a Ag line scan in order to verify that the Ag distribution is truly anti-correlated to the S distribution. Figure 4.7(a) is a S map showing three channels. This map region is just beside the map region of Fig. 4.6(a). Figure 4.7(b) is a line scan whose position is indicated in Fig. 4.7(a). This line scan, which is certainly of poor quality when compared to the line scan of Fig. 4.5, does indeed show that Ag and S are anti-correlated. Unfortunately, there are problems in obtaining both a good quality map and line scan in the same region of the crystal. These problems are addressed in Section 4.4.

In terms of a channel configuration, the line scan data in Fig. 4.5 can now be explained further. Even though the line scan was nominally perpendicular to the intercalated edge of the crystal, the development of the Ag maxima and minima as the beam progresses in from the crystal edge can be realized by a small misalignment of the crystal and as the crossing

of the line scan over channels which may curve and divide as intercalation proceeds from the crystal edge. This is consistent with the fact that the Ag maxima and minima in Fig. 4.5 are wider than the channels in Fig. 4.6(a). This type of channel distribution was also observed in samples intercalated directly as stage-2 (Type III samples).

4.3.2 Intercalation Into Two Adjacent Edges of a Crystal

As was mentioned in Section 3.3 the cleaving direction of the intercalated crystals was from the unintercalated region toward the intercalated region, so the direction of the channels is approximately parallel to the direction of cleaving. To show the channels are not an artifact of the cleaving direction, Ag was simultaneously intercalated into two adjacent edges of a crystal, the angle between the edges being 60 degrees. When cleaving such a crystal, one cannot simultaneously cleave in a direction perpendicular to both intercalated edges. Figure 4.8 shows a S map of such a stage-2 (Type I) crystal. The data were obtained by point measurements taken 2 μm apart in both directions. Fig. 4.8 consists of three separate maps, one of each of the adjacent edges and the third being the corner where the two edges meet. Channels are seen to be present on both edges, however, they do not appear in the corner region. The interpretation of this corner effect is that channels growing from each edge interfere with each other during the intercalation process and destroy the channel-like structure. Figure 4.9 shows the secondary electron images of the map regions of Fig. 4.8. The images show that the crystal surface contains no features which could account for the observed channel structure.

Further evidence of this type of corner effect is shown in Figures 4.10(a) and 4.10(b) for a crystal with a corner angle of 120°. Fig. 4.10(a) is a schematic of a crystal intercalated as stage 2 (Type I). It shows the crystal edge, the intercalation front, and where the channels should and should not appear, according to expected "interference" of channels at corners. If a line scan is done in the position indicated, channels should begin to appear at about 110 μm from the crystal edge (as measured along the line scan direction). Fig 4.10(b) is the line scan obtained. Ag and S oscillation start at about 90 μm from the crystal edge, which is in reasonable agreement with 110 μm. The Ag and S are anti-correlated, as expected. The reason for the decrease in intensity of the Ag oscillations as the intercalation front is approached is unknown. The weak period in the Ag beyond the front is considered noise.

4.3.3 Deintercalation From a Crystal Edge

Stage 2, Type IV samples (deintercalated from stage-1 to stage-2) also show the channel-like structure as shown by the S map in Figure 4.11(a). The dark band down the center of the map is caused by beam effects (discussed in Section 4.4) resulting from a previous line scan. This line scan data is shown in Figure 4.11(b) and the data are well correlated with the map features. Thus deintercalation of the stage-1 region of a crystal occurs with the stage 2 channel configuration.

4.3.4 Three-Dimensional Intercalate Distributions

A complete channel domain model requires evidence of channels deeper in the crystal, not just on the exposed cleaved surface. The ratio, R, of

Ag maxima to Ag minima calculated from line scan data does provide evidence of the intercalant distribution a couple of galleries below the surface. Further evidence is given by observing channels at two different levels in a crystal. The crystal whose Auger maps are shown in Figure 4.8 was re-cleaved. A Sulfur Auger map of the new exposed surface is shown in Figure 4.12. The map region is approximately below the upper map region of Fig. 4.8, and shows the channel structure deeper in the crystal. It was not possible to determine whether or not these channels were spatially correlated (or anti-correlated) to those in the previously exposed gallery.

If it were possible, somehow, to remove only the surface islands of Ag, then any line scan data initially showing features similar to Fig. 4.5 would be predictably altered. First, the Ag maxima would become Ag minima and vice versa (likewise for S and Ti). Second, the new value of R for Ag would become ≈ 2.8. Several attempts were made to remove the surface Ag on crystals by very lightly sputtering the crystal surface with Ar^+ ions. While it may seem futile to attempt to remove a sub-monolayer of Ag from the surface by bombarding it with heavy ions, attempts were made nonetheless. The results were inconclusive and generally a mess, indicating that sputtering was far too violent a procedure. This was expected from the outset, but it was certainly worth a try. Other attempts were made to remove the surface Ag by chemical reactions. We know of no reactions that could create a Ag compound that would be volatile and thus fly off the crystal surface. However, one reaction attempted was to expose the cleaved surface to HCl vapor, the idea being that AgCl might form on the surface. This soluble salt could then be washed away. The results, again, were inconclusive. Auger analysis on samples which were exposed to

the HCl vapor, but not subsequently washed, revealed no Cl Auger signal, indicating that the reaction to produce AgCl was not occurring. Samples exposed to the vapor and then washed in distilled water and/or methanol showed gross carbon and oxygen contamination and were, therefore, of no use.

4.3.5 Intercalant Distributions Showing No Domain Structure

Not all samples tested showed a channel configuration. More often than not, the measured Ag distribution was spatially constant in the intercalated region. A S map of such a region is shown in Figure 4.13. Possible reasons for these frequent results will be addressed in Chapter 7 (cleaving at unintercalated regions being the most obvious) . The only consolation is that when any non-constant Ag distributions were observed, the results were always in a channel configuration.

4.3.6 Stage-1 Samples

Analyzing samples intercalated entirely to stage-1 (Type II) involved cleaving problems. As was stated in Section 3.3, the intercalated crystals were cleaved in the direction of the unintercalated region of the crystal to the intercalated region of the crystal. The reason for this is that unintercalated crystals cleave easier (creating a smoother cleaved surface) than intercalated crystals. For a stage-1 sample, where the entire crystal is intercalated to stage-1, there exists no large unintercalated regions in the crystal. So the cleaving process is very difficult and many samples do not cleave sufficiently well in order to create a smooth, clean surface. In fact, of all the stage-1 samples made, <u>none</u> of them cleaved well enough

for surface analysis. This was frustrating, and after making about 50 to 100 stage-1 samples with no success, no more were attempted.

4.4 ELECTRON BEAM EFFECTS

Up to this point, Auger results have been presented with little or no mention of how the electron beam may affect the sample surface. It was known from the beginning of Auger analysis that the beam affects the Auger signals, and this section is dedicated to examining these effects.

Figure 4.14(a) is a schematic of a cleaved stage-2 crystal surface. Two line scans were done, the horizontal one first, shown in Figure 4.14(b), followed by the vertical one, shown in Figure 4.14(c). This sample showed no evidence of channels. The horizontal line scan shows virtually constant Ag, S, and C distributions. The vertical line scan also shows constant distributions, except where it crosses the previous horizontal scan. Here the S and Ag signals decrease and the C signal increases. It is fairly obvious that the electron beam attracts carbon to the sample surface, creating a peak. This carbon build-up attenuates the Ag and S signals. This type of beam effect can be seen in the Auger maps in Figures 4.7(a) and 4.11(b), where the S signal is attenuated in positions where the electron beam was previously situated. This effect, common to almost all electron microscopes (46), made it difficult to obtain good quality line scans and maps in the same region of the crystal.

Auger data is reproducible on the same region of a crystal but only for short periods of time. Figure 4.15 shows a series of line scans taken at the same place on the crystal but at different times (Figures 4.15(a) was shown previously in Fig. 4.10(b)). Figures 4.15(a) and 4.15(b), taken

30 minutes apart, are effectively identical, showing the same Ag and S distributions. In a line scan done a few hours later, shown in Figure 4.15(c), the distributions are still similar but the oscillations near the intercalation front are less pronounced. One day later (Figure 4.15(d)) the distributions are nearly constant. So Auger data is reproducible only over a period of hours. For this reason short data acquisition times are required and this is why S Auger maps were used to infer the Ag distributions.

The disappearance of the Ag and S oscillations with time are thought to result from either, (i) extensive carbon build-up to the point where any Ag island structure is so far from the surface (below the deposited carbon) that Auger analysis cannot see the islands above the noise levels, or (ii) surface diffusion of Ag, destroying the channel structure near the surface. Initially, surface diffusion of Ag was thought to be the most likely candidate, however, two points disfavor this idea. The first is that if surface Ag diffuses to a constant distribution with time then eventually Auger analysis should "see through" the surface Ag and the subsurface Ag distribution should be analyzed. If this happened the Ag maxima should eventually become minima and vice versa (according to the DH model), and the ratio, R, for Ag should increase to ≈ 2.8 (Section 4.3). No such observations were seen. The second point that disfavors surface Ag diffusion is concerned with the observation of structure that appears optically on the crystal surface weeks after cleaving, and will be discussed in Chapter 5.

Fig. 4.1 Sample orientation in the SAM. The directions of sample movement are indicated.

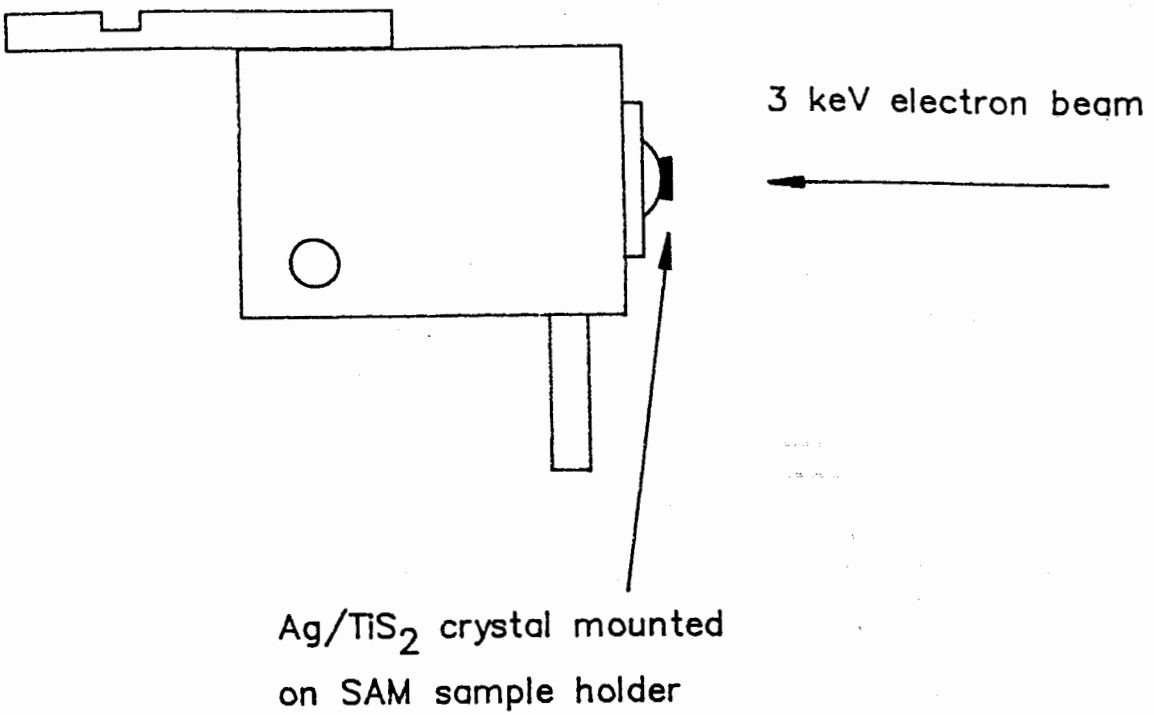
3 keV electron beam
Ag/TiS2 crystal mounted
on SAM sample holder
Z
Y
X

Fig. 4.1

Fig. 4.2 Secondary electron image of a stage-2 partially intercalated crystal in the SAM. Visible are the crystal edge and the intercalation front.

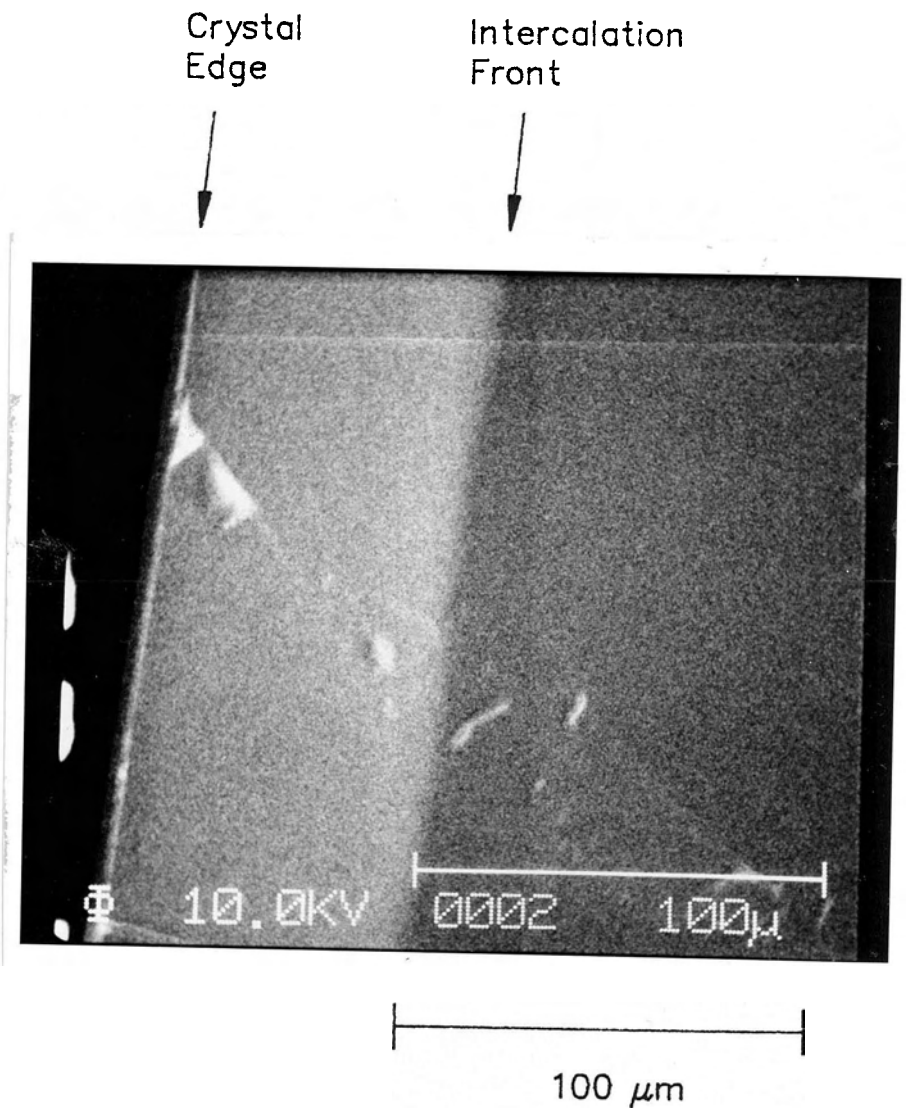

Fig. 4.2

Fig. 4.3 Auger survey spectrum of stage-2 crystal. The elemental peaks are labelled.

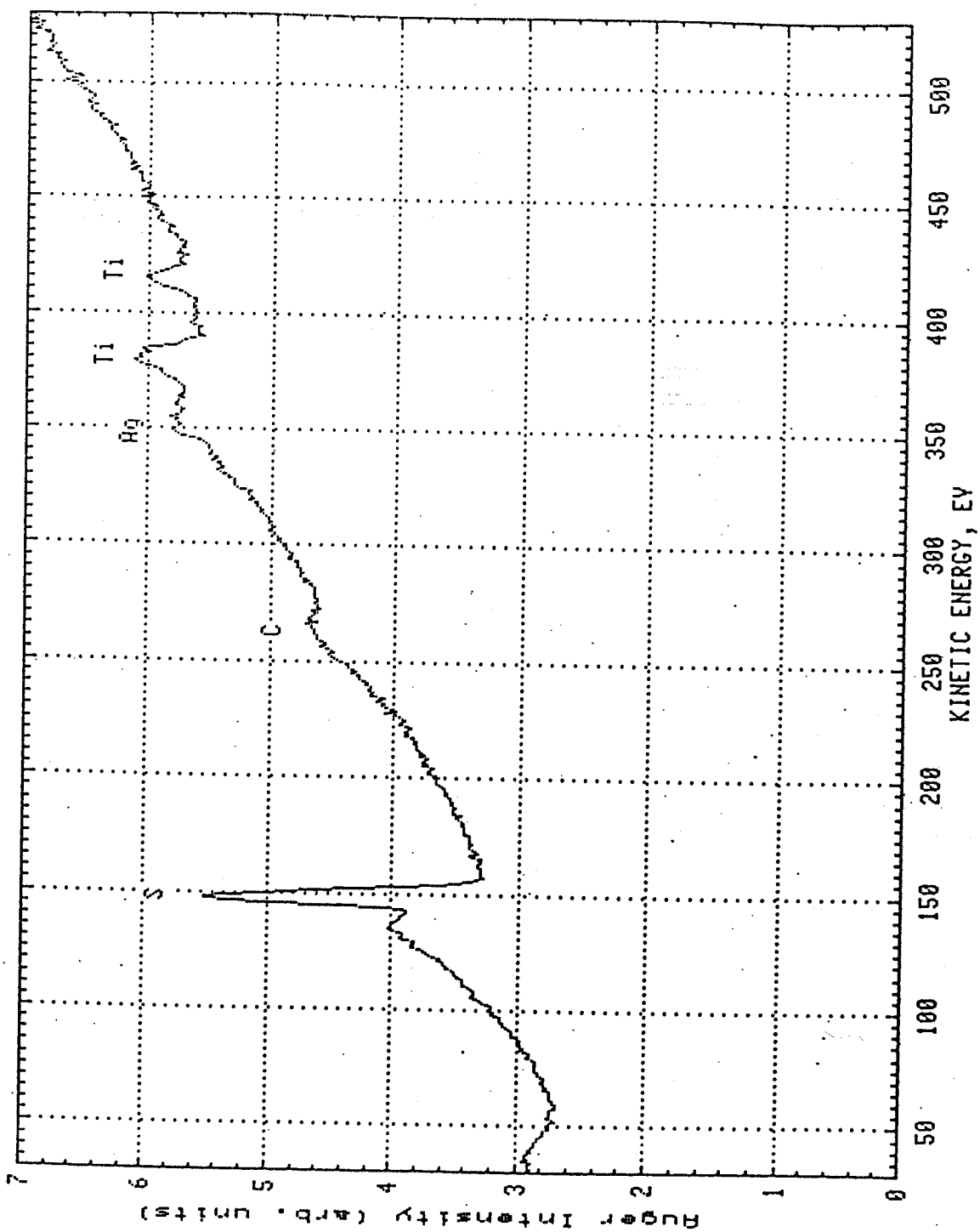

Fig. 4.3

Fig. 4.4 Differentiated Auger survey spectrum of Fig. 4.3.

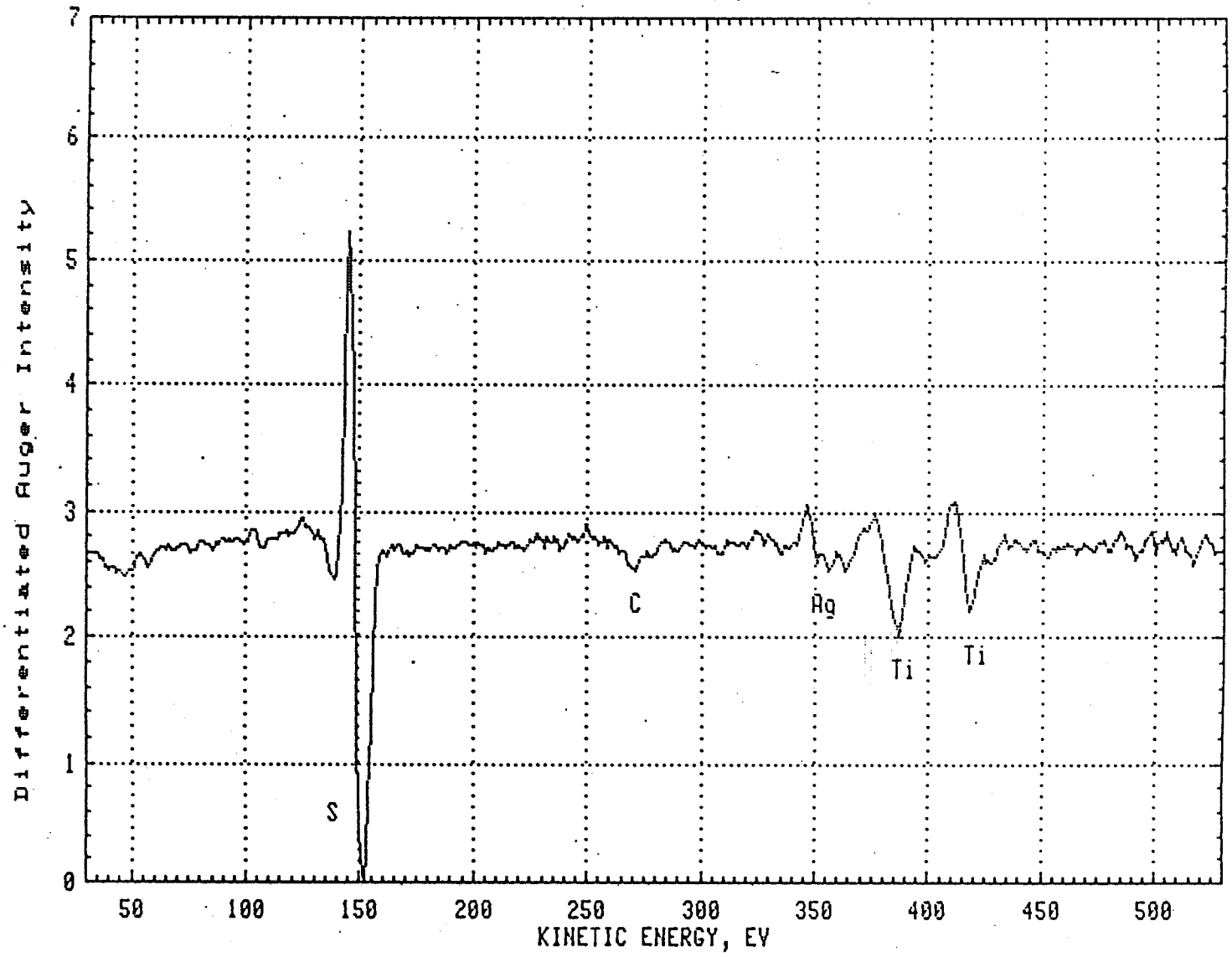
Differentiated Auger Intensity
7
6
5
4
3
2
1
0
50
100
150
200
250
300
350
400
450
500
KINETIC ENERGY, EV
S
C
Ag
Ti
Ti

Fig. 4.4

Fig. 4.5 Auger line scan across the surface of a stage 2 Type-I crystal. The crystal edge is at -5 μm and the arrow indicates the position of the intercalation front, as seen in the secondary electron image. (Data taken by P. Joensen)

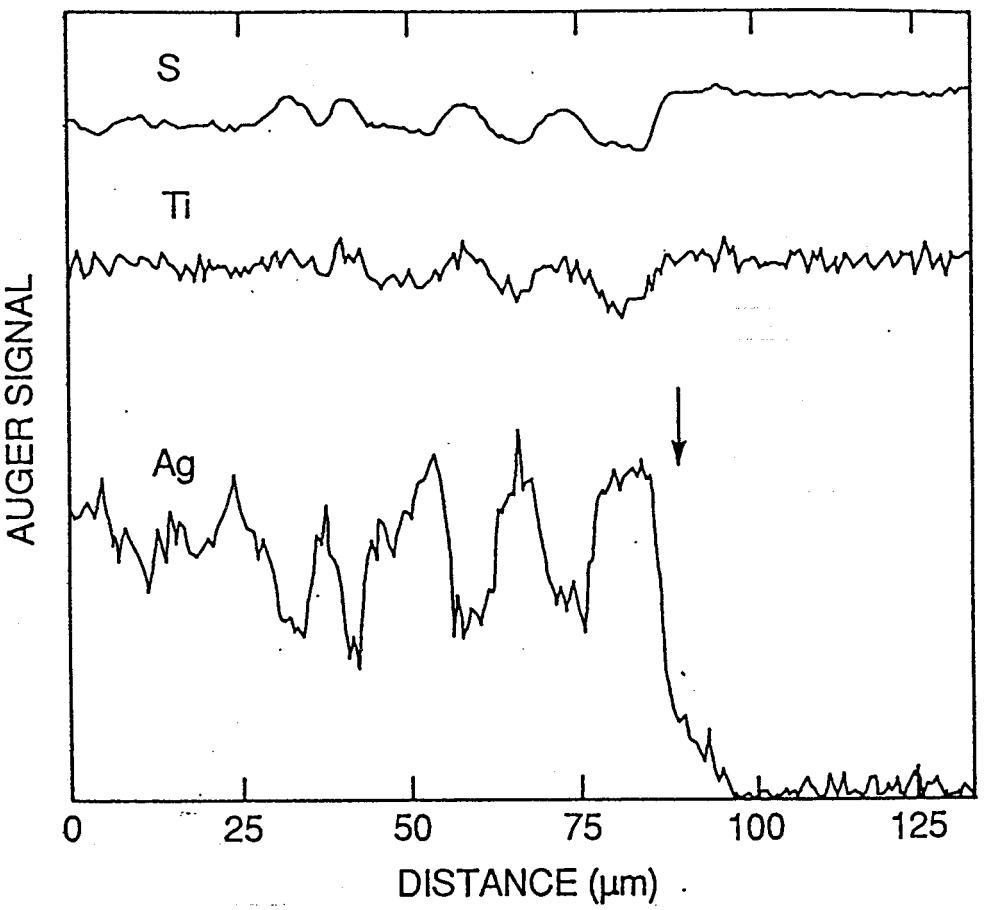

Fig. 4.5

Fig. 4.6 Auger maps showing "channel" structures.

(a) Sulfur Auger map of a stage 2, Type-I crystal. The intercalation front and the crystal edge are shown. The dark horizontal band across map is due to electron beam effects (see Section 4.4)

(b) A computer enhanced version of (a). This clearly shows the intercalant structure in the intercalated region.

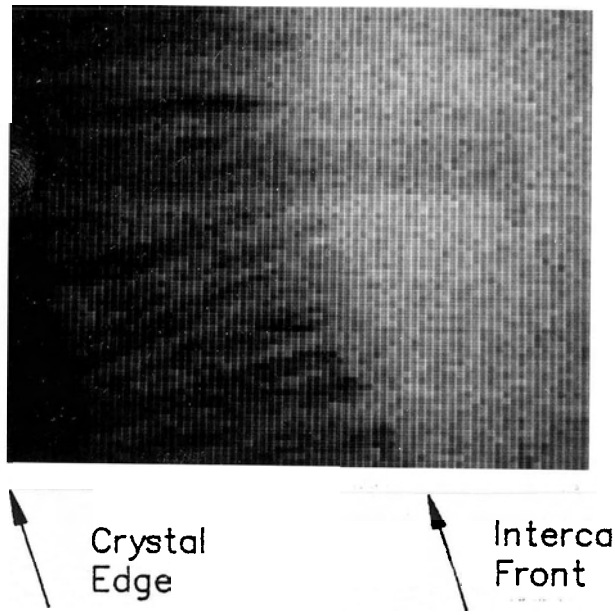

(a)

20 μm

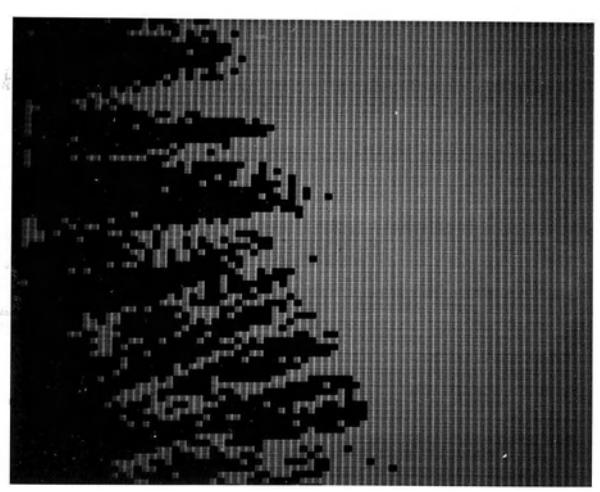

(b)

Fig. 4.6

Fig. 4.7 Auger map and line scan showing "channel structures".

(a) Sulfur Auger map of a stage-2, Type-I crystal. The position of the line scan for (b) is shown: the orientation of the line scan was horizontally to the right (at the position indicated by the arrow), and the start and finish of the line scan is indicated by the horizontal bar at the top edge of the photograph. The bright regions correspond to a strong S signal. The crystal edge just below the bottom of the photograph and is nearly parallel to the line scan direction. The dark square in the upper right region of the photograph is due to electron beam effects caused by a previous Auger map.

(b) Auger line scan for Ag in the map region of (a). The sulfur signal in (a) and silver signal in (b) are clearly anti-correlated. Note the different scale for the map and the line scan.

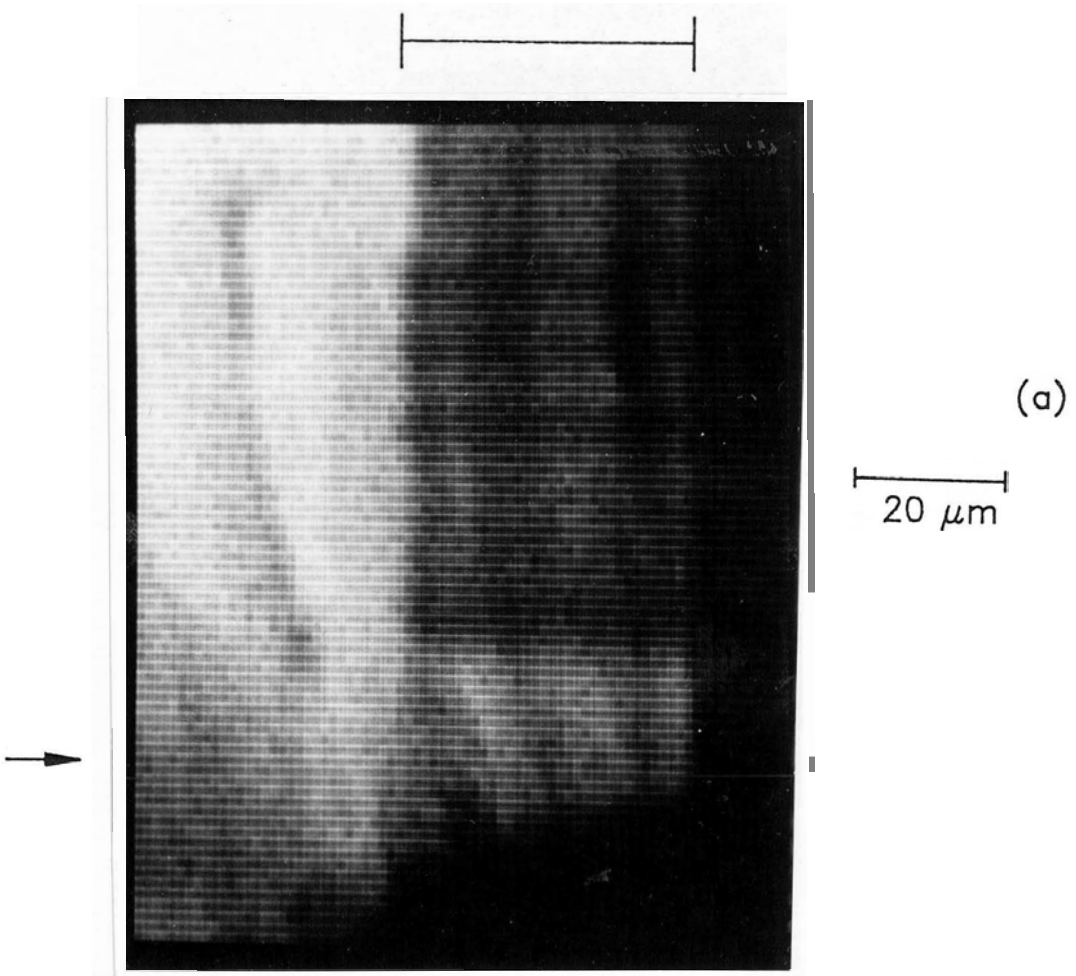

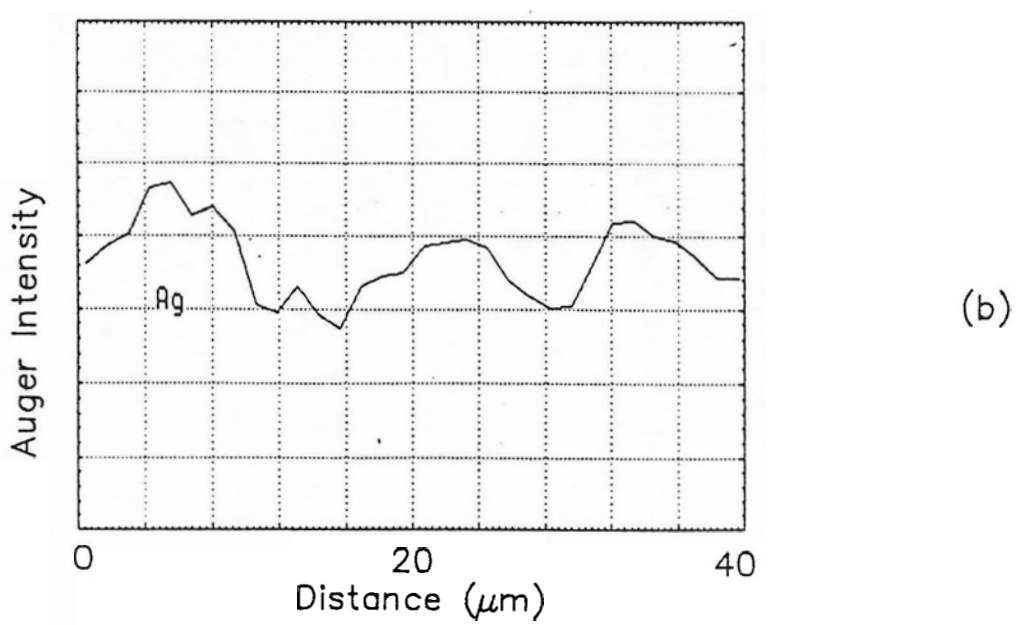

Fig. 4.7

Fig. 4.8 Three sulfur Auger maps on the same surface of a stage-2, Type-I crystal. Channels are seen at the crystal edges (a) and (b), but not in the corner region (c) where the two edges meet.

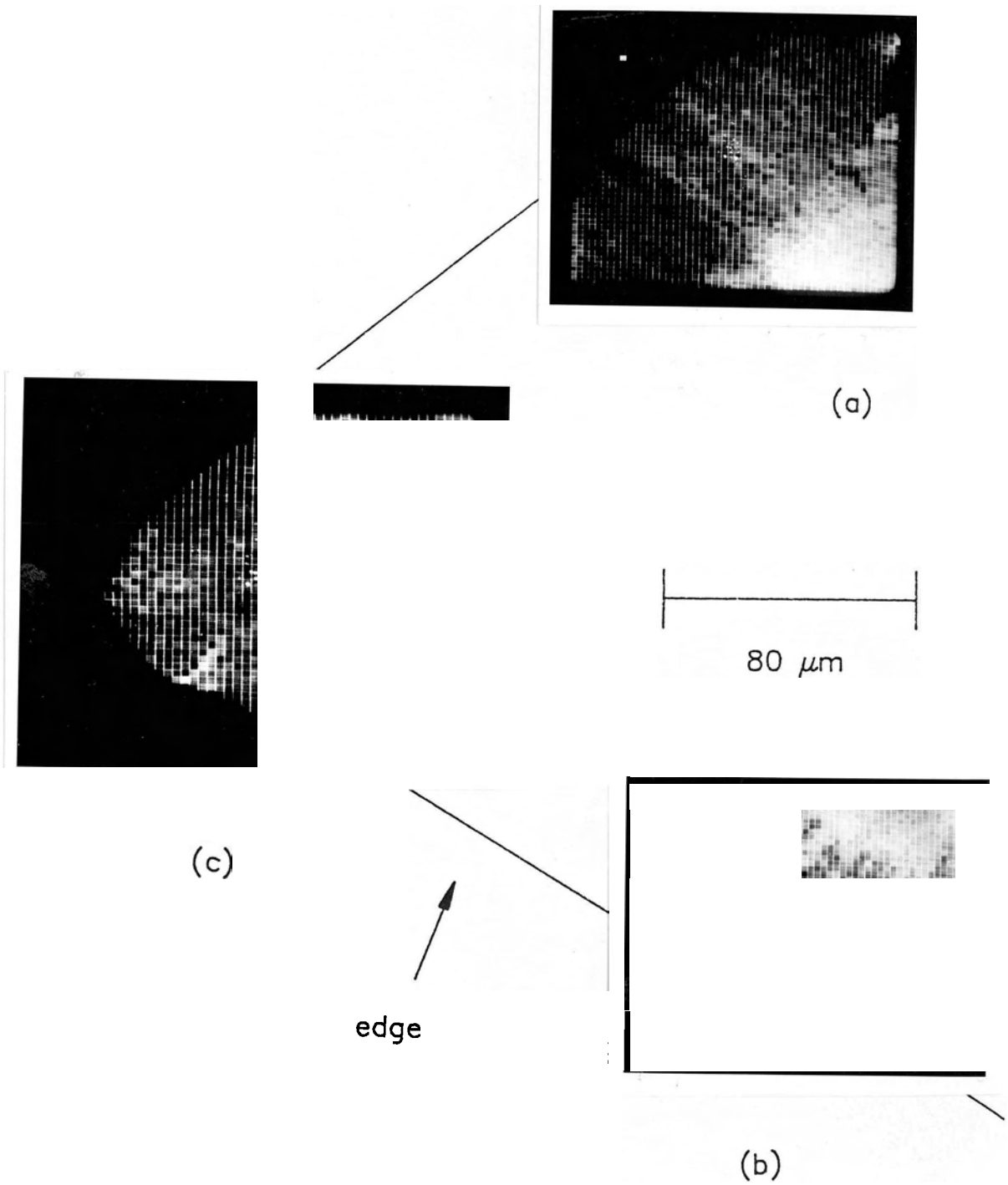

Fig. 4.8

Fig. 4.9 Secondary electron images of the Auger map regions of Fig. 4.8. No channel like features are visible.

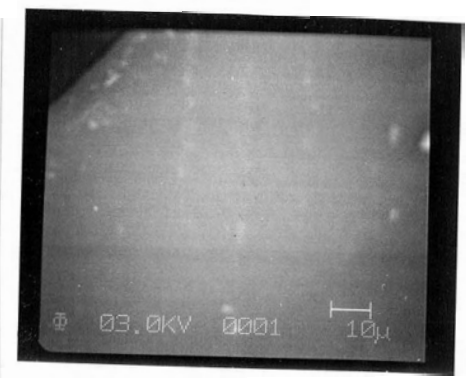

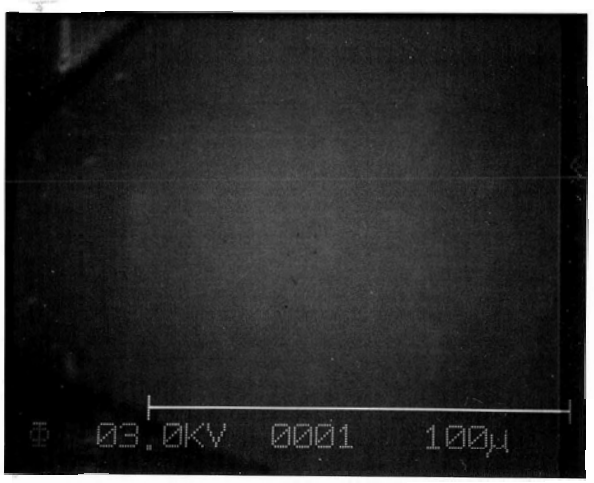

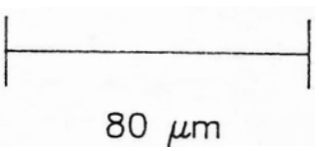

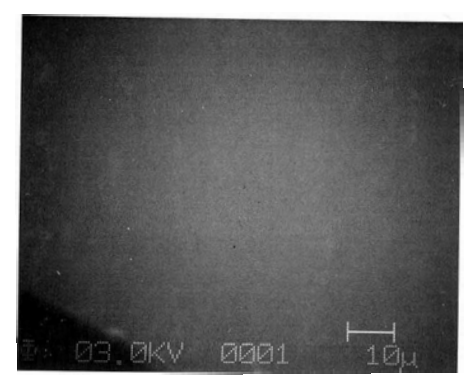

Fig. 4.9

Fig 4.10 A crystal schematic along with Auger line scan data near a corner region.

(a) Schematic of a real, partially intercalated stage-2 (Type-I) crystal showing where channels should occur near a corner region.

(b) Auger line scan whose position is shown in (a).

(a)

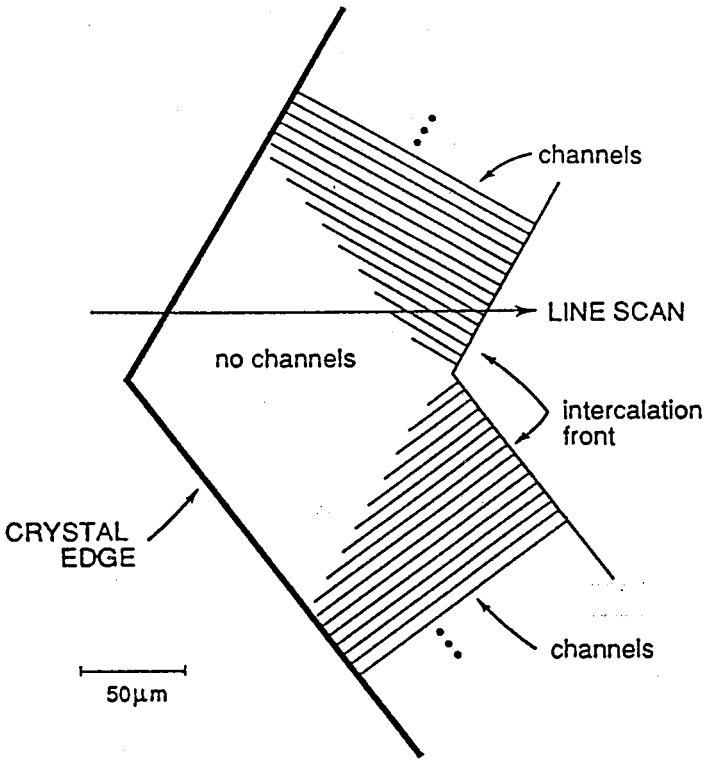
channels
LINE SCAN
no channels
intercalation front
CRYSTAL EDGE
channels
50μm

(b)

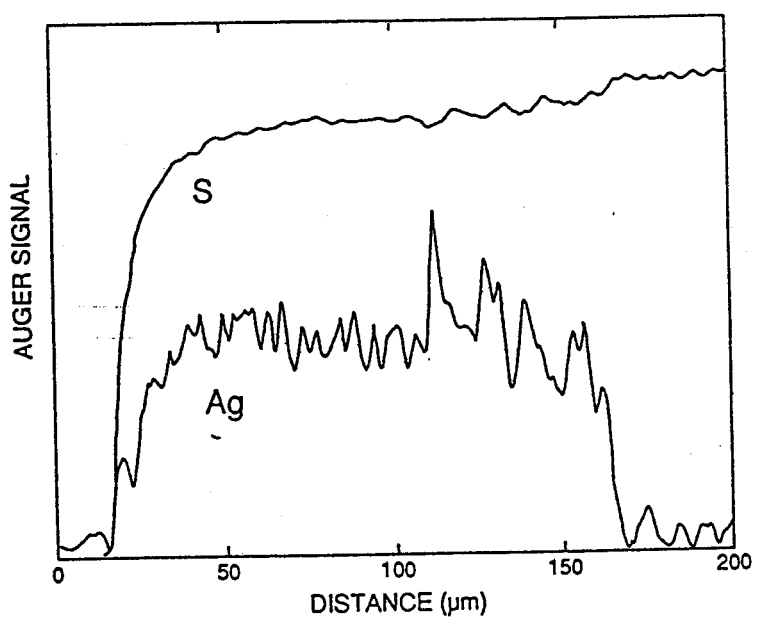
AUGER SIGNAL
S
Ag
0
50
100
150
200
DISTANCE (μm)

Fig. 4.10

Fig. 4.11 Auger map and line scan showing channel structures for a stage-2 deintercalation crystal.

(a) Sulfur Auger map of a stage-2, Type-IV (deintercalation from stage-1 to stage-2) crystal showing channels.

(b) Auger line scan in the map region (indicated by the dark vertical band down the middle of the map). The line scan data correlate with the map features.

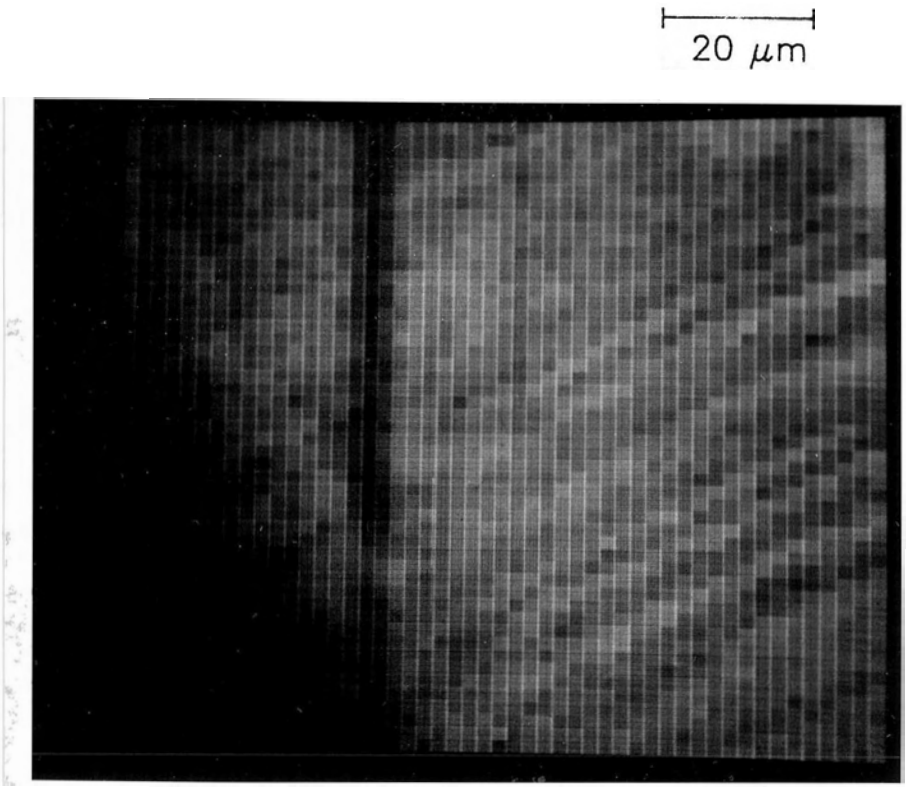

(a)

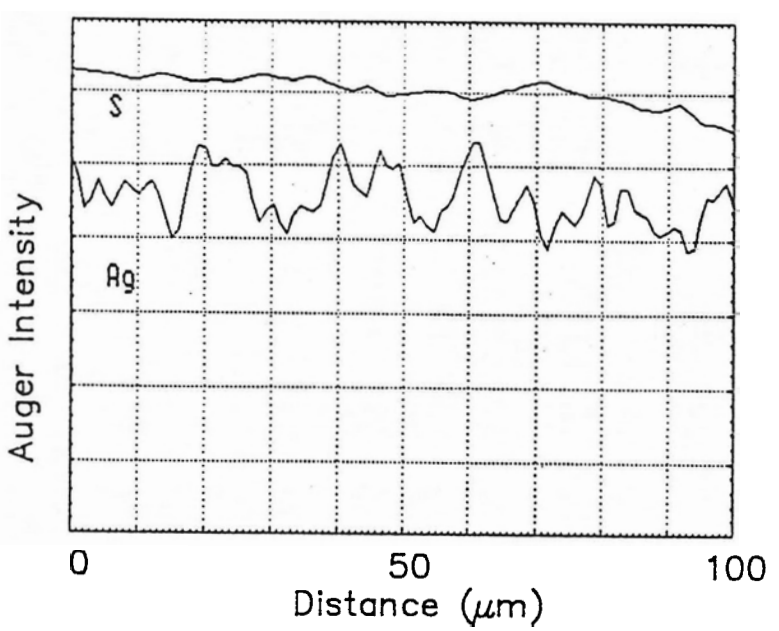

(b)

Fig. 4.11

Fig. 4.12 Sulfur Auger map of the sample shown in Fig. 4.8 after re-cleaving.

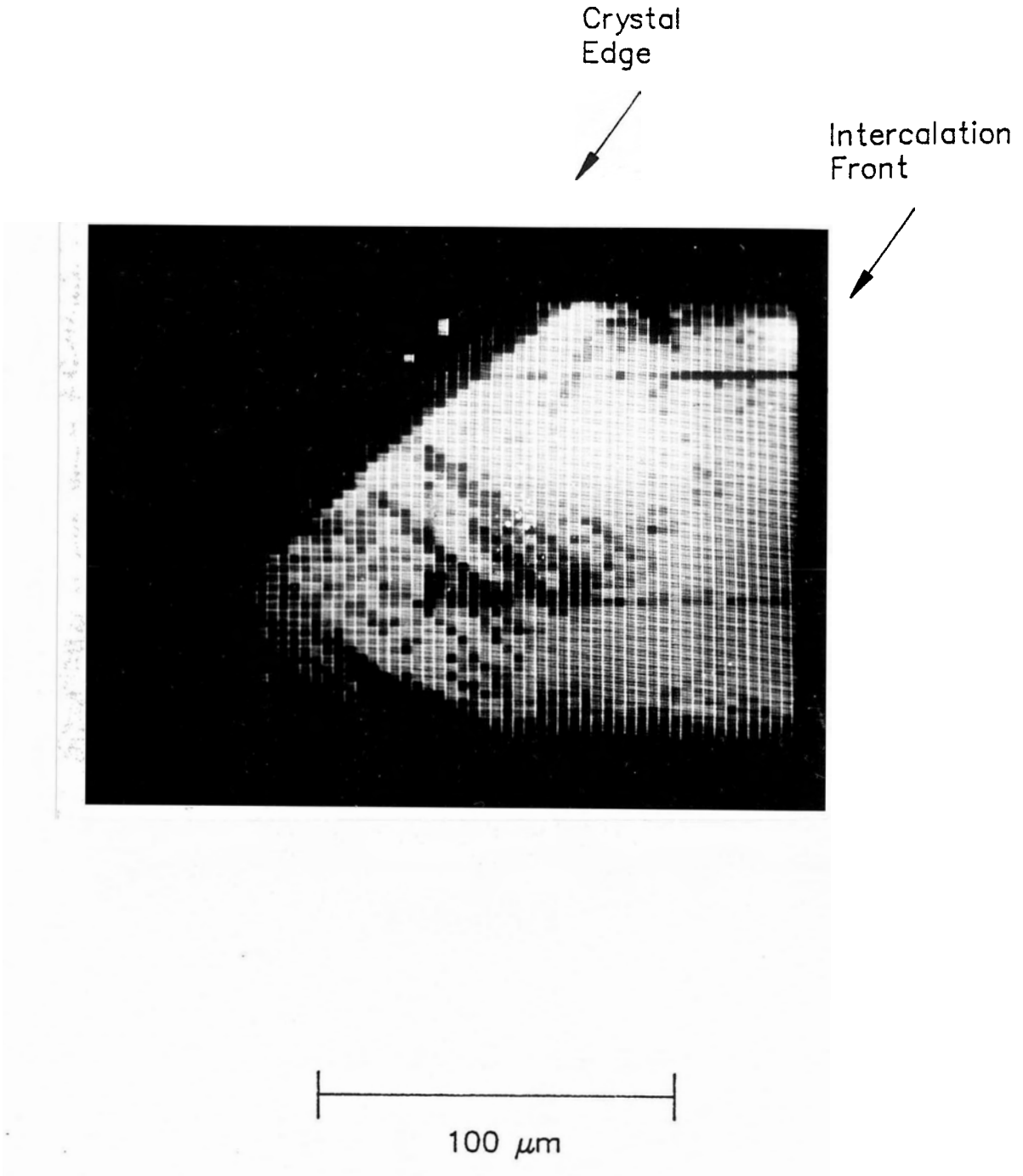

Fig. 4.12

Fig. 4.13 Sulfur Auger map showing no structure in the intercalant distribution.

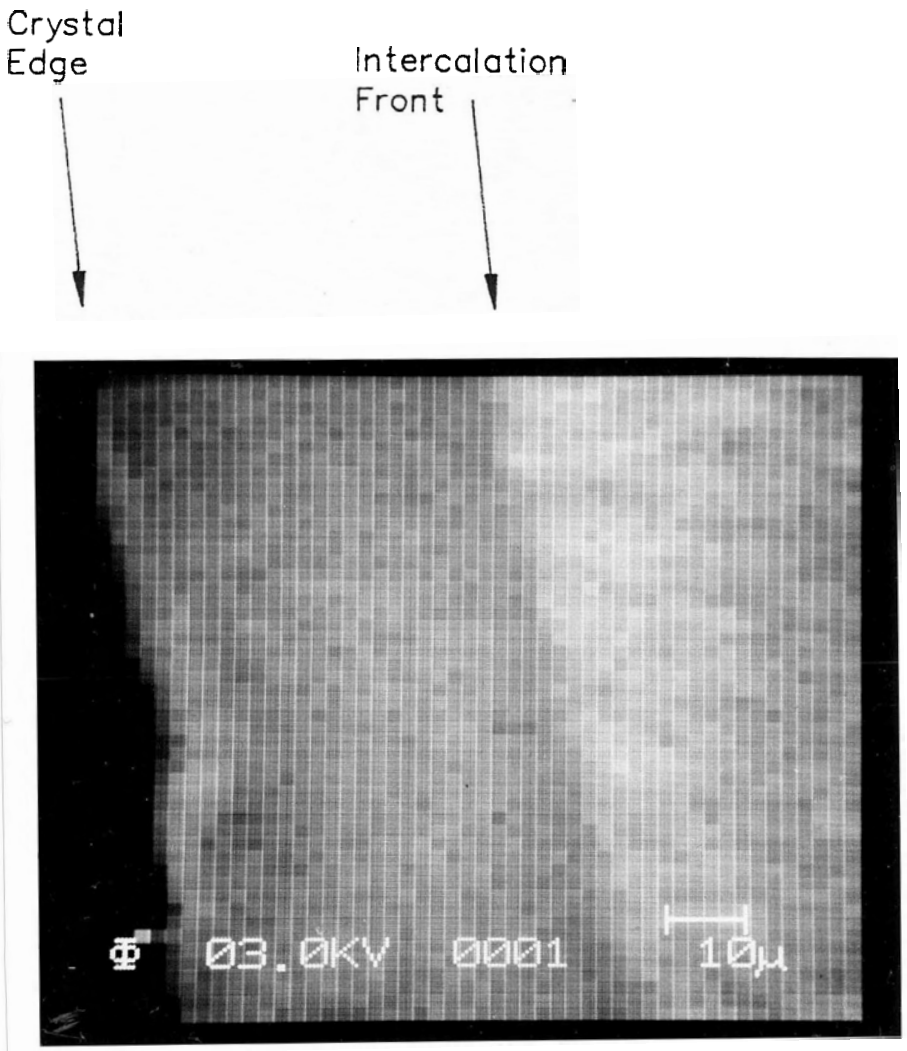

Fig. 4.13

Fig. 4.14 Auger line scans showing electron beam effects.

(a) Schematic of a crystal showing the positions of two Auger line scans. The horizontal line scan was done first.

(b) Horizontal line scan.

(c) Vertical line scan showing the electron beam effects caused by the horizontal line scan.

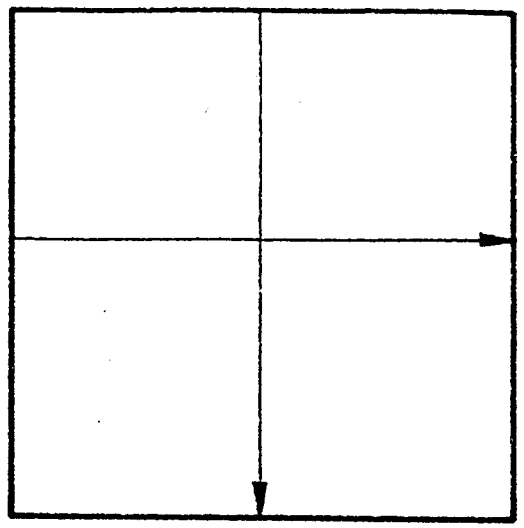

(a)

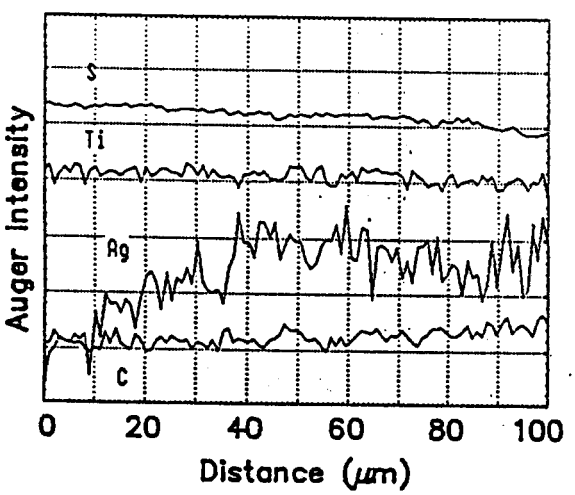
S
Ti
Ag
C
Auger Intensity
0
20
40
60
80
100
Distance (μm)

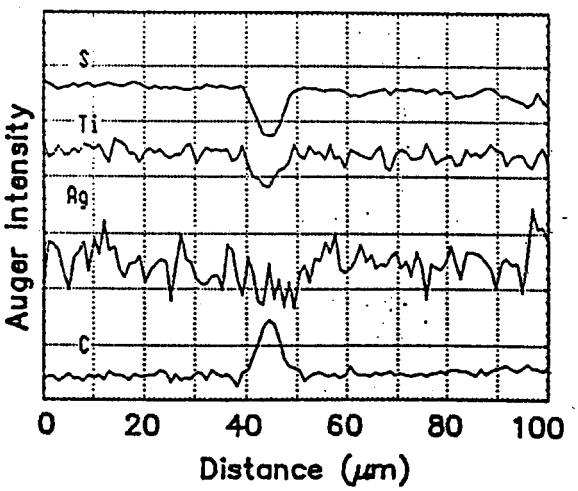
S
Ti
Ag
C
Auger Intensity
0
20
40
60
80
100
Distance (μm)

(b)

(c)

Fig. 4.14

Fig. 4.15 Time evolution of Auger line scan data.

(a) Initial line scan done immediately after cleaving. The crystal edge is at about 20 μm and the intercalation front is at about 160 μm.

(b) Line scan done 30 minutes after (a). The crystal edge is at about 15 μm and the intercalation front is at about 160 μm.

(c) Line scan done 3 hours after (a) The crystal edge is at about 30 μm and the intercalation front is at about 170 μm.

(d) Line scan done 24 hours after (a). The crystal edge is at about 50 μm and the intercalation front is at about 190 μm.

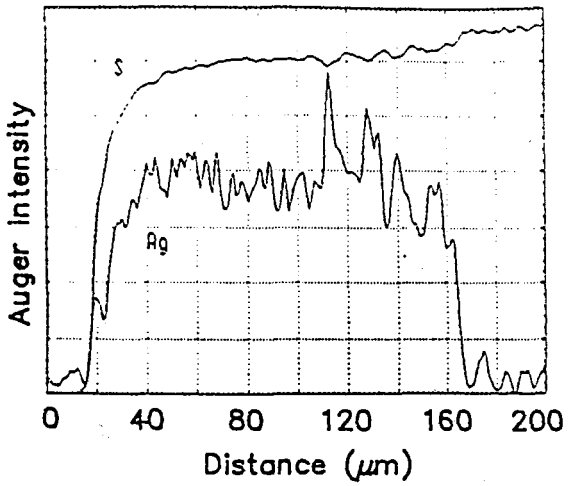
S
Ag
Auger Intensity
0
40
80
120
160
200
Distance (μm)

(a)

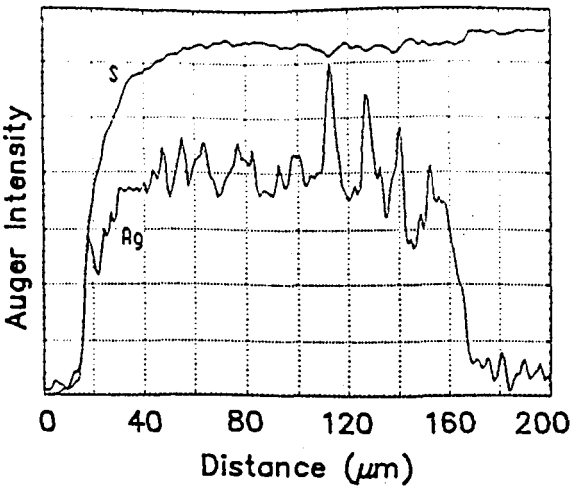
S
Ag
Auger Intensity
0
40
80
120
160
200
Distance (μm)

(b)

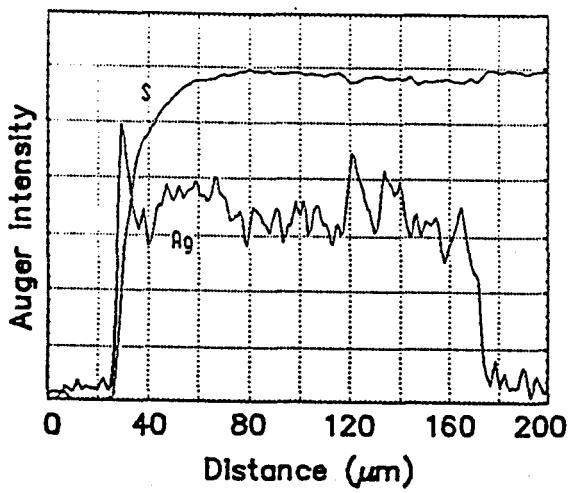
S
Ag
Auger Intensity
0
40
80
120
160
200
Distance (μm)

(c)

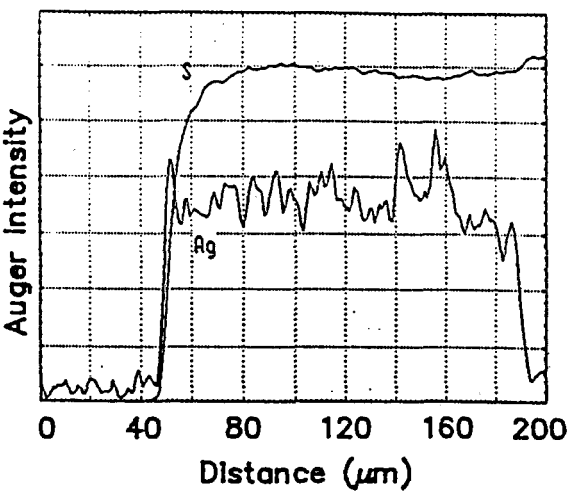
S
Ag
Auger Intensity
0
40
80
120
160
200
Distance (μm)

(d)

Fig. 4.15

CHAPTER 5

OPTICAL OBSERVATION OF SURFACE DECORATION OF INTERCALATED CRYSTALS

5.1 MOTIVATION FOR OPTICAL OBSERVATION

At the onset of this research project, it was assumed that all intercalant distributions on cleaved surfaces would be determined by Auger analysis, due to the simplicity and versatility of the technique. However, quite often after Auger analysis the crystal surfaces were examined under an optical microscope using high magnification. The reason was to confirm that the surfaces of the cleaved crystals possessed no topographical features which could account for the observed channel structure. Basically this was just a verification of the secondary electron images obtained in the SAM. As expected, the regions were featureless and at that point the samples "put on the shelf" and not examined further. Once in a while the samples analyzed in the SAM were not observed optically until a couple of days, or even a week, later. What was seen optically after a week or two was entirely unexpected.

All optical observations were done with reflected light using combinations of an Olympus model FH microscope and a Reichert model MeF2 microscope. The results will be shown in Sections 5.2 and 5.3 and all attempts to explain the results will be deferred until Section 5.4.

5.2 SURFACE DECORATION OF INTERCALATED CRYSTALS

5.2.1 Surface Decoration Patterns

As was mentioned in Section 4.4 the electron beam in the SAM affected the sample surface in a way that carbon was attracted to the position of

the electron beam on the sample surface. This effect, in turn, altered the strength of the Auger signals. A week or two after Auger analysis, it was found that the exact positions of Auger line scans and Auger maps could be seen optically. They appeared as dark regions on the sample surface - dark lines for line scans and dark squares for maps. The regions appeared faint at first and got darker with time until they were essentially black. This turned out to be very useful for determining the exact position of the line scans and maps. Other features soon began to appear in the intercalated region, whether the electron beam previously was situated in these areas or not. What appeared were dark regions approximately 5 μm wide and spaced 10 μm apart, extending from the crystal edge to the intercalation front. Figure 5.1 shows how such a surface appeared for a stage-2, Type IV (deintercalation from stage-1 to stage-2) crystal. The dark square region is the location of an Auger map and dark, straight, narrow lines within this square are the locations of Auger line scans. This Auger map region is from the map shown in Figure 4.11(a). The dark bands within the map region, extending from the crystal edge to the intercalation front, were found to correlate with the dark regions in the Auger map of Fig. 4.11(a). Thus the channels seen with Auger maps, after a couple of weeks of being exposed to air, were now an optically visible decoration pattern! Figure 5.2 is a photograph under lower magnification showing the entire crystal edge. The surface decoration appears everywhere - except in the corner region, again confirming the Auger results of the "corner effect" discussed in section 4.3.

Knowing that the surface decoration patterns correlated well with the Auger results, Auger analysis at this stage was practically abandoned.

Intercalated crystals were cleaved and left for a couple of weeks, waiting for the decoration pattern to become optically visible. The ease of optical observation and the fact that the entire intercalated region could be examined all at once made Auger practically obsolete. Throughout the remainder of this section, optical results will be presented, some of which would have been nearly impossible to obtain using the SAM.

A stage-2 (Type I) crystal, mounted on 5 minute epoxy, was cleaved. One half of the crystal remained on the epoxy and the other half on DRG Sellotape. Immediate optical observation of the two halves of the crystal revealed featureless surfaces. The two halves were left in air for a couple of weeks and then again examined optically. Figures 5.3(a) and 5.3(b) show the resulting two halves of the crystal. Fig. 5.3(a) is a photograph of the mirror image of one surface and Fig. 5.3(b) is a photograph of the other surface. The information in these figures is incredible. First, the decoration pattern appears on both sides of the cleaved crystal and the pattern is the same on both sides (the similarity is very clear on the photographic negatives). This very strongly supports the cleaving assumption, namely that the Ag in the cleaved gallery splits equally (on an atomic scale) upon cleaving. Second, the decoration patterns do not always extend continuously from the crystal edge to the intercalation front. Instead, in the region of the arrows, they extend from the crystal edge to, what appears to be, a cleavage step nearly parallel to the crystal edge. At the step, the pattern contrast reverses so that the dark regions become light and the light regions become dark. The patterns then extend from this step to, what appears to be, another cleavage step, and again the contrast reverses. This is exactly what the

DH model predicts for a stage-2 system if the steps represent a height corresponding to an odd number of TiS_2 layers. No contrast reversal would be expected if the steps correspond to an even number of TiS_2 layers.

5.2.2 Cleavage Step Heights and "Correlation Lengths"

The height of cleavage steps, where a decoration pattern constrast reversal is seen, is important in determining the distance, perpendicular to the c-axis, over which the intercalant forms a "perfect" domain structure; this distance, in some sense, corresponds to a correlation length.

Consider a perfect DH domain model for a stage-2 system. The islands in one gallery are anticorrelated to those in an adjacent gallery, and this is repeated throughout the entire crystal. In a real stage-2 system, this perfect domain structure would not be expected to exist through the entire crystal; small deviations in a perfect domain structure over a small c-axis distance could be magnified over a large c-axis distance and effectively destroy the long-range order of the domain structure. The question being posed is: Given an island distribution in one gallery, how many odd (even) numbered galleries must one go away from the first until the island distribution is no longer anticorrelated (correlated) to the first? Observing the decoration patterns in two different galleries (via a cleavage step) and measuring the step height provides information on this question.

An attempt to measure the cleavage step heights shown in Figs. 5.3(a) and (b) was done using the beam polarization interferometer on the Reichart microscope. With this attachment, the field of view consists of a set of

interference fringes superimposed on the sample surface. Across a step, a fringe shift equal to the spacing between fringes corresponds to a step height of $\epsilon/2$, where ϵ is the wavelength of the radiation. The wavelength of the radiation used was $\epsilon \approx 5000$ Å, and no fringe shift across the steps was observed. Due to the width of the fringes it was estimated that 0.1 of a fringe shift should be measurable, so that the step height is < 250 Å, or about 40 host layers.

Figure 5.4 shows a surface decoration pattern on the surface of another stage-2 (Type I) crystal. Again cleavage steps nearly parallel to the crystal edge appear to be present, and the decoration patterns appearing in the different galleries show less correlation (or anti-correlation) than in Fig. 5.3. For this reason one would expect that the cleavage step heights on this crystal would be greater than those of Fig. 5.3. Attempts at mesuring the step heights using the polarization interferometer revealed no fringe shift again, indicating that the cleavage step height are less than 250 Å.

The above results of the observed fringe shifts seems to indicate that the correlation length, l, is less than 40 host layers (about 250 Å). More sensitive techniques of measuring the cleavage step heights are obviously in order, such as Scanning Tunneling Microscopy (STM).

STM employs a sharp tungsten tip which is brought very near a sample surface. An applied voltage between the tip and the sample causes electrons to quantum mechanically tunnel from the tip to the sample, and the tunneling current is very sensitive to the distance between the tip and the sample. Controlled movement of the tip is achieved by the use of piezoelectric materials. Monitoring the tunneling current as the tip is

"walked" across the sample surface, gives the surface topology on an atomic scale, in particular, surface steps equivalent to one atomic layer can be measured. A detailed explanation of the operation of STM is available elsewhere (47). While STM would be ideal for measuring small cleavage step heights, the microscope available to us has the drawback that the tungsten tip has the capability to move only about 500 Å. Therefore, in order to measure the height of a particular cleavage step, one must be able to position the tip to within about 500 Å of the step. This was not possible. The positioning of the tip could only be done to within about 10,000 Å, far too large of a distance for what was required. While some random cleavage step heights were measured (see Chapter 7), the tip could not be placed accurately enough to measure a particular step height.

5.3 INTERCALATION THROUGH A PINHOLE

5.3.1 Pinholes and Staging

A pinhole is a naturally occurring hole or depression in TiS_2 crystals that occurs during the crystal growth. The size of these pinholes is usually very small, about a micron or less. Our surface decoration observations of intercalation through a pinhole indicates that stages similar to those occurring in the intercalation process into a straight crystal edge occur around the pinhole.

The domain pattern for stage-2 crystals is drastically affected by the geometry of the crystal edge through which intercalation proceeds. This is evident from the absence of channels in corner regions, as shown previously in Figs. 4.8 and 5.2. Therefore, intercalation through a pinhole, where the intercalation proceeds radially, could show very

different domain structures. In particular, a stage-2 parallel channel structure cannot exist since it would require domains of stage-2 intermixed with domains of stage-1 near the pinhole and domains of empty crystal near the intercalation front. This is clear from the topology of a stage-2 channel structure. It is not obvious what type of intercalate distribution would be expected from a pinhole given that channels exist at a crystal edge. A seemingly natural topology would be of a radial structure of some sort.

5.3.2 Natural Pinholes versus Artificial Pinholes

Naturally occurring pinholes cannot be made intentionally during the crystal growth procedure and the number of pinholes in crystals varies from crystal batch to crystal batch. The pinholes, in general, do not extend through the entire crystal (from surface to surface), and often cannot be seen with an optical microscope. This makes the procedure of observing domain structure very difficult. First, since is is not known if pinholes exist in a crystal (due to their small size) one must intercalate the crystals and hope to identify the pinholes from the existence of circular intercalation fronts. Second, if intercalation through the pinhole does occur, then subsequent cleaving of the crystal can "remove" the pinhole since it may not extend throughout the entire crystal. Due to these problems it was felt it that would be easier to work with artificial pinholes and attempts to create them were done by vaporizing a small hole in a crystal using a pulsed ruby laser. These attempts were abandoned due to the lack of power and the excessive size (about 100 μm) of the pinholes created. Pinholes made by focussed argon ion sputtering were about 80 μm

in size. These large sizes were considered unacceptable so natural pinholes were used and the problems associated with these were accepted and dealt with through patience.

5.3.3 Decoration Patterns from Pinholes

TiS_2 crystals were intercalated to stage-2 (Type-I) and the existence of pinholes was determined through the appearance of circular intercalation fronts. Crystals showing these fronts were subsequently cleaved and many times the pinhole was not very deep and it was peeled away. Cleaved crystals that resulted in the pinhole being "split" (which were very rare), were left for a week or two, waiting for an optical intercalate pattern to become visible. Fig. 5.5 is such a pattern. The pinhole appears as a dark triangle, with a lateral dimension of about 10-15 μm, in the center of the figure. The triangular shape is consistent with the hexagonal symmetry of TiS_2 crystals. The intercalated region is circular in shape, with a radius of about 100 μm, and is centered about the pinhole. As would be expected from the decoration patterns discussed in Section 5.2.1, the dark areas in the intercalated region correspond to the presence of Ag. While the decoration pattern is definitely radial, there are some features which seem to be inconsistent with a stage-2 domain model.

(1) There is no decoration pattern in the immediate vicinity of the pinhole. Dark regions only appear at distances of about 30 μm from the pinhole.

(2) In the outer areas of the intercalated region, where dark regions do occur, the area of the dark regions is less than the area of the light regions (a stage-2 domain

model, based on the conversion from stage-1 during the intercalation process, requires them to be equal). This is obvious since the radial structures become narrower as the intercalation front is approached.

In addition, the pattern does not seem to be particularly regular, in contrast with the patterns seen from intercalation from a crystal edge. One feature that is comparable to these other patterns are the widths of the radial structures, which tend to be of the order of 5-10 μm.

5.4 DISCUSSION OF OPTICAL RESULTS

5.4.1 Introduction

The optical results in Sections 5.2 and 5.3 were presented without any explanation for why the initial intercalate distributions seen with Auger analysis become optically visible. The Auger data in Chapter 4 indicated that the Ag occupied regions on the surfaces of freshly cleaved crystals are equivalent to 0.2 of a monolayer. This section addresses the issue of why the pattern formed by a sub-monolayer of Ag on the surface of a Ag intercalated TiS_2 crystal becomes optically visible with time.

5.4.2 Auger Data of Decoration Patterns

The reason the positions of Auger line scans and Auger maps become optically visible in time (Fig. 5.1) is likely related to the electron beam induced deposition of carbon in the ultra high vacuum system. Carbon contamination, stated in section 4.4, is associated with almost all electron microscopes. The carbon contamination then is somehow enhanced with time and becomes optically visible. Very little time was spent trying

to understand this enhancement since determining the reason for the visibility of the decoration patterns was of prime importance.

With regard to the visibility of the decoration patterns, one conclusion that can be drawn immediately is that they are related to the intercalated portion of the crystal since the patterns only appear in the intercalated regions of crystals and are not seen on unintercalated regions.

The first step was to determine whether the patterns were a property of the bulk crystal or merely a surface effect. Fig 5.6 is a photograph of the crystal surface shown in Fig. 5.1 after it had been brushed very lightly with the frayed end of a toothpick (a toothpick is somewhat of a crude instrument, but a single hair from a camel's hair brush provided the same results). The upper part of the figure is where the brushing occurred and is seen to be featureless, with only a clean crystal surface being exposed. This indicates that the patterns are on the surface only, and do not extend into the bulk of the crystal.

The next step was to determine the elemental composition of the patterns. This was easily done with Auger surveys and Auger line scans. Fig. 5.7(a) is the differentiated Auger survey of an intercalated region of a crystal showing an optically visible decoration pattern. The crystal surface examined is that of Fig. 5.1. From these figures, the relative elemental concentrations are very different than the usual surveys obtained from freshly cleaved, intercalated crystals. First, and most prominent, is that the crystal surface is contaminated with large quantities of carbon and oxygen. This is expected since the surface was exposed to air for many days. In addition, the S and Ti signals are weak and the silver signal is

very strong. The ratio of the S to Ti peak heights from the differentiated survey is about 3.5. This is smaller than the same ratio obtained from a clean crystal surface, which has a value of about 5.3. This relative increase in the Ti signal could be caused by the surface contamination since the mean free path for Ti Auger electrons is greater than that of S Auger electrons (see Chapter 4), resulting in the S signal being decreased by a larger amount.

Fig. 5.7(b) is the differentiated survey of the region of the crystal in Fig. 5.6 that was brushed off. Carbon and oxygen contamination still exist on the surface. Note that the oxygen and Ag signals are weaker, especially the Ag. The ratio of the S to Ti peak heights from the differentiated survey has increased to a value of about 4, which is consistent with the fact that the amount of contamination on the crystal surface has decreased. These observations indicate that the optically visible features in the intercalated region seem to be associated (mainly) with a large amounts of Ag and O on the surface which in turn attenuates the S and Ti signals.

A line scan done approximately parallel to the edges of the crystal shown in Fig. 5.1, is shown in Fig. 5.8. The Ag signal oscillates and the Ag peaks were found to correspond to the dark positions of the decoration pattern. The S and C Auger signals correlate with the Ag while the oxygen is anti-correlated to all three. No Ti signal was measured in the line scan since its signal from the Auger survey was so weak. This line scan data is quite complicated since oxygen seems to play the most important role in causing the elemental oscillations (it anti-correlates to the other elements).

Another method to determine the elemental concentration in a sample is X-ray Fluorescence (XRF) (48). XRF differs from Auger in that it measures the concentration of elements to a depth of about 1 μm below the sample surface, therefore, it is more of a bulk, rather than surface, measurement. XRF results from regions of samples showing decoration patterns revealed little, or no, Ag in the bulk of the initially intercalated portion of the crystal. This is unusual since XRF measurements on freshly intercalated crystals show strong Ag signals (20).

5.4.3 Spontaneous Deintercalation

The results of Auger and XRF studies on the crystals showing surface decoration patterns indicate that the crystals are no longer intercalated since there is little bulk Ag and, at the same time, a large amount of Ag is present on the surface. A plausible explanation for this is that the intercalated crystals have deintercalated.

Evidence that the crystals deintercalate is also provided by X-ray diffraction. Fig. 5.9 shows an X-ray diffractogram of a crystal before and after deintercalation. The data was collected using a Phillips diffractometer, using as X-ray wavelength of 1.54 Å. As seen in the figure, before the decoration pattern is visible there exists the stage-2 peak at 14.6° (from the intercalated region of the crystal) and the empty crystal peak at about 15.6° (from the unintercalated region of the crystal). After the decoration pattern becomes visible, the only peak in the diffractogram is the empty crystal peak. The shift of this peak to higher angles, compared to the empty crystal peak before deintercalation, is due to an offset in the diffractometer.

Note that this spontaneous deintercalation was only observed for partially intercalated, stage-2, cleaved crystals. Partially intercalated uncleaved crystals, or fully intercalated stage-2 crystals were not observed to spontaneously deintercalate.

The optical visibility of the surface decoration pattern implies that at least some of the deintercalated Ag migrates to the crystal surface that is directly above the previously intercalated region of the crystal. Furthermore, the Auger work shows that this Ag prefers to migrate to, and reside, in regions where there was 0.2 of a monolayer of Ag immediately after cleaving (Fig. 5.8).

5.4.4 Summary

From the results of sections 5.4.2 and 5.4.3, the proposed sequence of events that leads to the surface decoration pattern is:

(i) A TiS_2 crystal is intercalated to stage-2, with the domain structure being in the form of channels.

(ii) The stage-2 intercalated crystal is cleaved, exposing Ag on the newly created surface. The Ag occupied regions are in the form of channels with a local concentration of 0.2 of a monolayer. This is supported by the Auger data (Chapter 4) on freshly cleaved, intercalated crystals. The location of the Ag in the channel regions is stable. Ag does not diffuse onto other regions of the crystal surfaces (see Section 4.4 and also Section 5.4.5), however, the Ag may locally diffuse and form small Ag clusters which cannot be detected optically.

(iii) When the cleaved crystals are exposed to air and left for days, or weeks, they deintercalate.

(iv) The Ag deintercalating from the crystal edge is mobile and "crawls" onto the crystal surface. This Ag diffuses across the crystal surface, and its final location must somehow depend on the pre-existing surface Ag since the diffusion stops at the intercalation front. Therefore, it is proposed that the Ag diffuses, and nucleates at Ag previously on the surface (at channel locations). This process continues until deintercalation stops, and by this time, the amount of Ag on the crystal surface is large enough to make it optically visible. Why the deintercalating Ag prefers to reside at channel locations can be explained by using a combination of the domain model, charge transfer, and the cleaving assumption (Section 3.4). From the cleaving assumption and the domain model, in regions containing no Ag surface islands there is Ag in the first gallery below the surface which transfers charge to the surface layer, causing the surface host layers in these regions to be negatively charged. These charged surface regions repel any deintercalating Ag diffusing across the surface. In contrast, in regions where there is surface Ag, there is no Ag in the first gallery below the surface, so the surface layers in this region are effectively neutral. Therefore, these surface regions allow deintercalating Ag to donate charge to the surface S layer and create a Ag/S compound on the surface which is then neutral and stationary.

5.4.5 Loose Ends

It is appropriate now to discuss a point mentioned in Section 4.4 - that the Auger results on freshly cleaved crystals are only reproducible over a period of several hours. As was mentioned this was not thought to

be due to surface diffusion of Ag. One reason, discussed in that section, was that if the surface Ag diffused to a uniform layer, then Auger line scan analysis could "see through" the surface layer and be able to analyze the Ag distribution in the first gallery below the surface. The Ag Auger intensities in the line scan data did not indicate this effect. The other reason is that the surface decoration patterns become visible after a period of days (or weeks) after cleaving and correlate well with the Auger channels seen almost immediately after cleaving. If surface diffusion of Ag did occur within hours after cleaving, the decoration patterns would not be expected to correlate with the Auger data, or even appear at all.

One remaining point to address is the unusual elemental oscillations of the line scan data of Fig. 5.8. The "usual" line scan data obtained immediately after cleaving shows the S signal to be anticorrelated to the Ag signal, whereas this one shows the Ag and S signals to be correlated! A likely reason for this is that surface Ag reacts with the surface sulfur, or even sulfur in the atmosphere, and forms a silver sulfide on the surface. This could occur in conjunction with titanium oxide formation as well, creating complicated surface distributions.

One other interesting result is that, in some cases, the Ag composing the decoration pattern condensed into minute silver crystallites. Under a Scanning Electron Microscope, the crystallites appeared triangular, which indicates that they are "growing" on the TiS_2 surface in the [111] direction. This was confirmed by X-ray diffraction and also by previous studies of Ag on TiS_2 surfaces (49).

Fig. 5.1 Optical photograph of a surface decoration pattern of a stage-2 deintercalated crystal. The crystal edge and intercalation front are shown. The dark square is an electron beam effect from an Auger map. The dark features within the map region (which are barely visible) were found to correlate with the Auger map data, shown in Fig. 4.11(a).

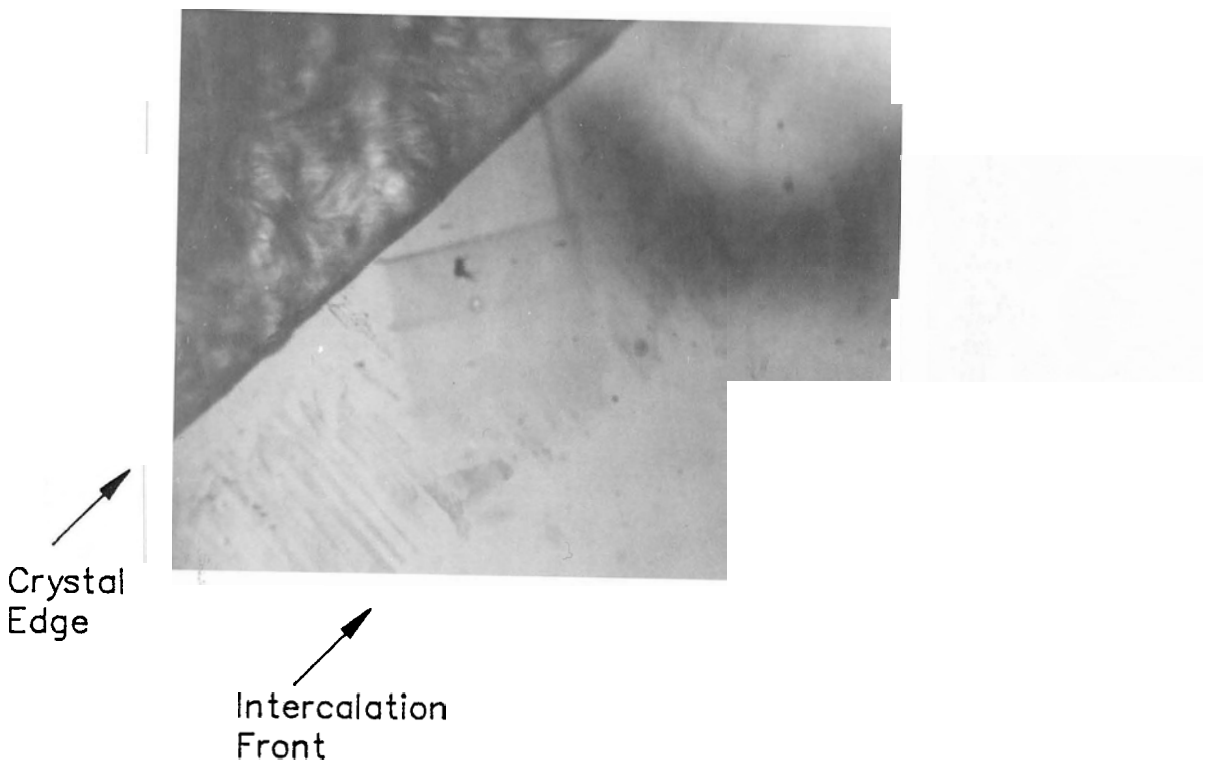

Fig. 5.1

Fig. 5.2 Low magnification optical photograph of the surface decoration pattern of the same surface as in Fig. 5.1. This photograph shows the entire crystal edge along with the corner region (lower left portion of the photograph).

Fig. 5.2

Fig. 5.3 Optical photographs showing decoration patterns on both surfaces created by cleaving. The crystal was intercalated as stage-2, Type-I. Both of the surfaces created by cleaving the crystal are shown. The regions of interest are indicated by the arrows. The mirror image of one surface is shown in (a) and the other surface is shown in (b). The decoration patterns are the same on the two surfaces. The decoration pattern contrast reverses across cleavage steps parallel to the crystal edge, in agreement with the stage-2 domain model (see text).

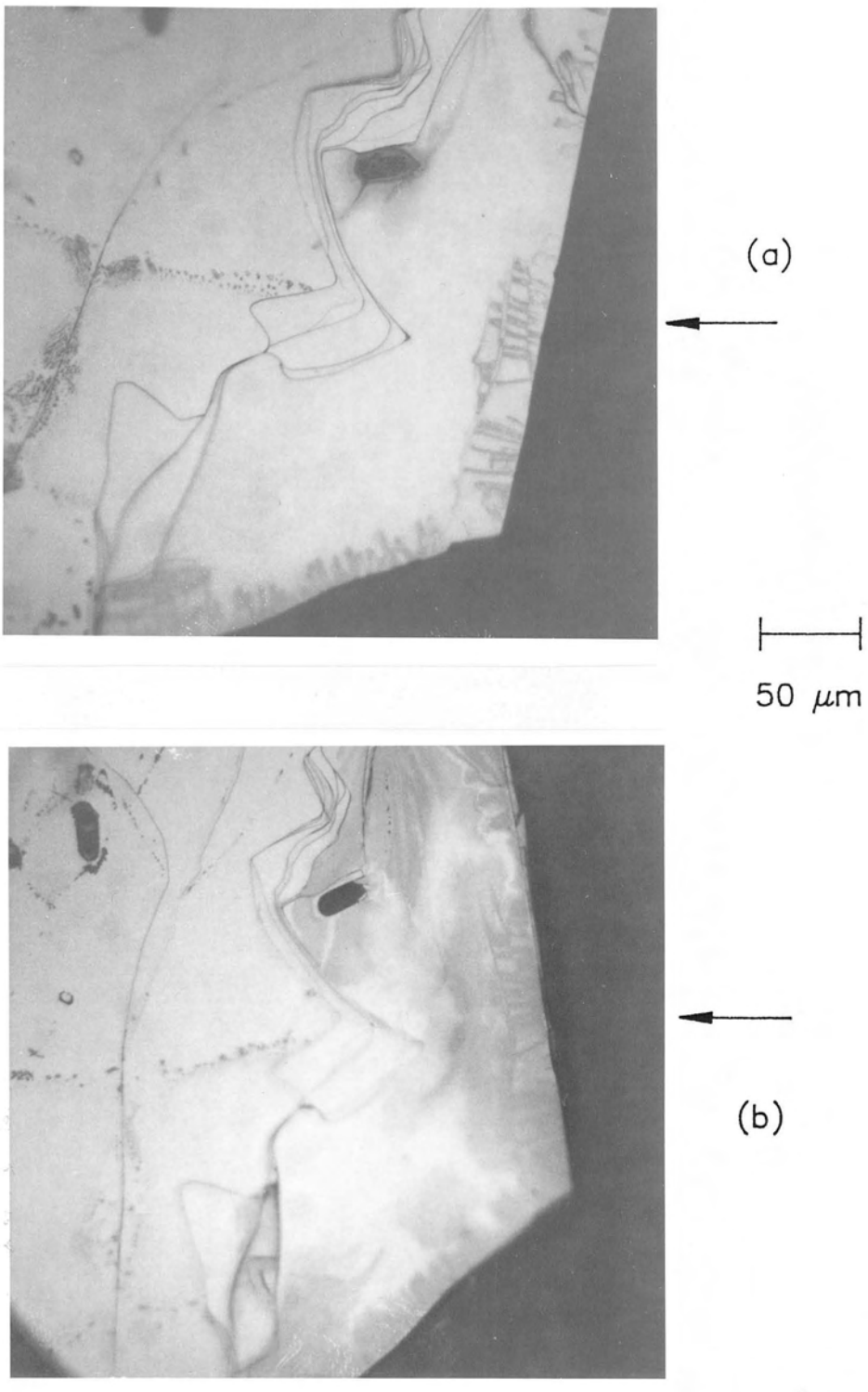

Fig. 5.3

Fig. 5.4 Optical photograph of a surface decoration pattern near a cleavage step. The crystal was intercalated as stage-2, Type-I. Cleavage steps are parallel to the crystal edge. There is little correlation between the patterns on either side of the steps.

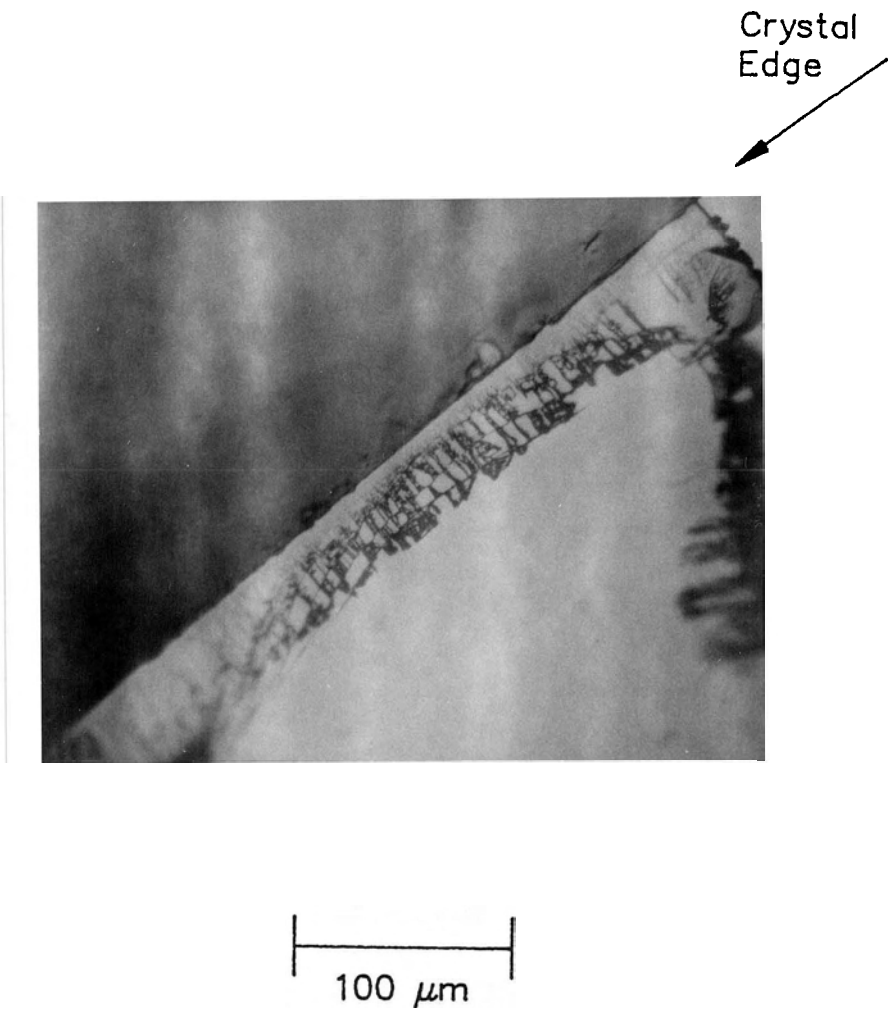

Fig. 5.4

Fig. 5.5 Optical photograph of a surface decoration pattern of a crystal intercalated through a natural pinhole. The crystal was intercalated as stage-2, Type I. The pinhole is the dark triangle in the center of the photograph. The decoration pattern consists of radial structures.

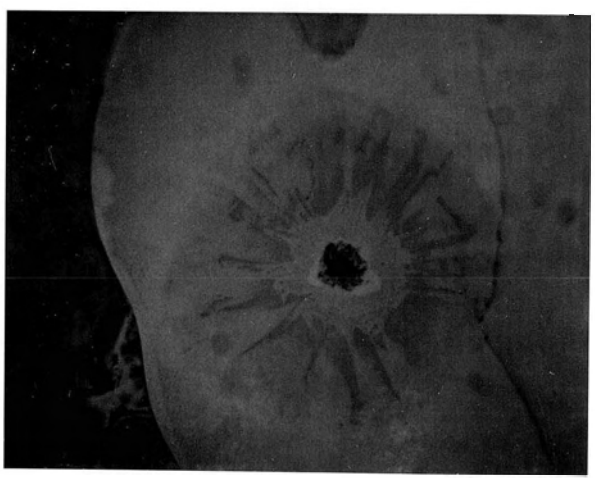

100 μm

Fig. 5.5

Fig. 5.6 Optical photograph of a surface decoration pattern that has been lightly brushed away. This crystal surface was shown previously in Fig. 5.1. The part of the crystal in the top portion of the photograph has been lightly brushed off, removing the decoration pattern. **No pattern ever re-emerged** after the brushing.

Fig. 5.6

Fig. 5.7 Differentiated Auger survey of a surface decoration pattern.

(a) Differentiated Auger survey of a decoration region of the crystal shown in Fig. 5.1. The Ag, C, and O signals are strong and the Ti and S are weak as compared to a survey on a clean surface of an intercalated crystal (see Fig. 4.3 for example).

(b) Differentiated Auger survey of the region of the crystal shown in Fig. 5.6 that was brushed off. The peak heights are very different as compared to the survey in (a).

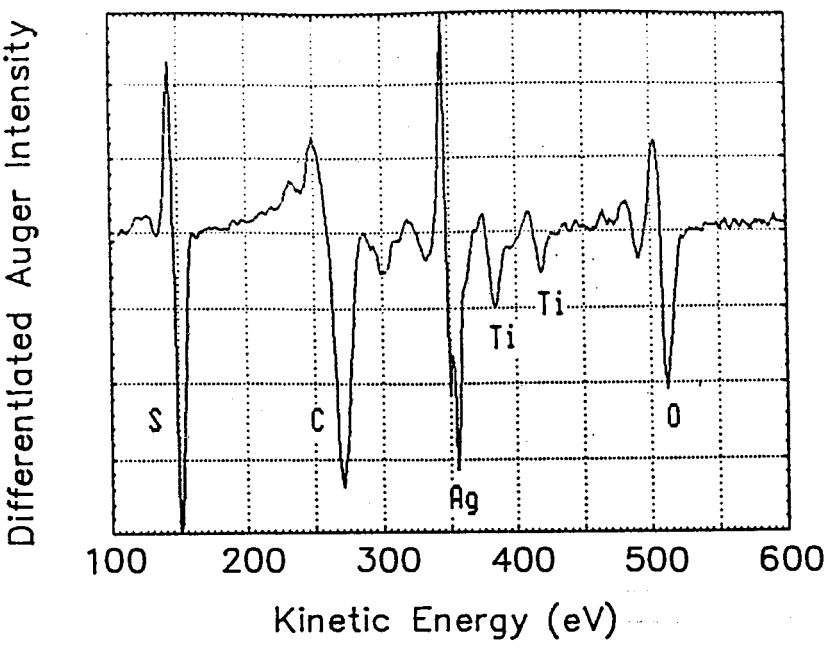
Differentiated Auger Intensity
S
C
Ag
Ti
Ti
O
100
200
300
400
500
600
Kinetic Energy (eV)

(a)

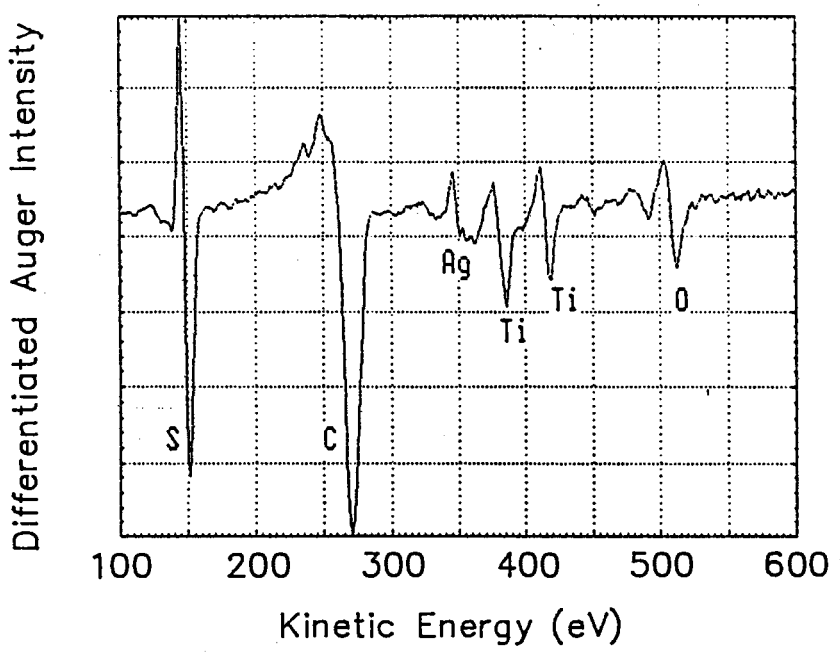
Differentiated Auger Intensity
S
C
Ag
Ti
Ti
O
100
200
300
400
500
600
Kinetic Energy (eV)

(b)

Fig. 5.7

Fig. 5.7 Differentiated Auger survey of a surface decoration pattern.

(a) Differentiated Auger survey of a decoration region of the crystal shown in Fig. 5.1. The Ag, C, and O signals are strong and the Ti and S are weak as compared to a survey on a clean surface of an intercalated crystal (see Fig. 4.3 for example).

(b) Differentiated Auger survey of the region of the crystal shown in Fig. 5.6 that was brushed off. The peak heights are very different as compared to the survey in (a).

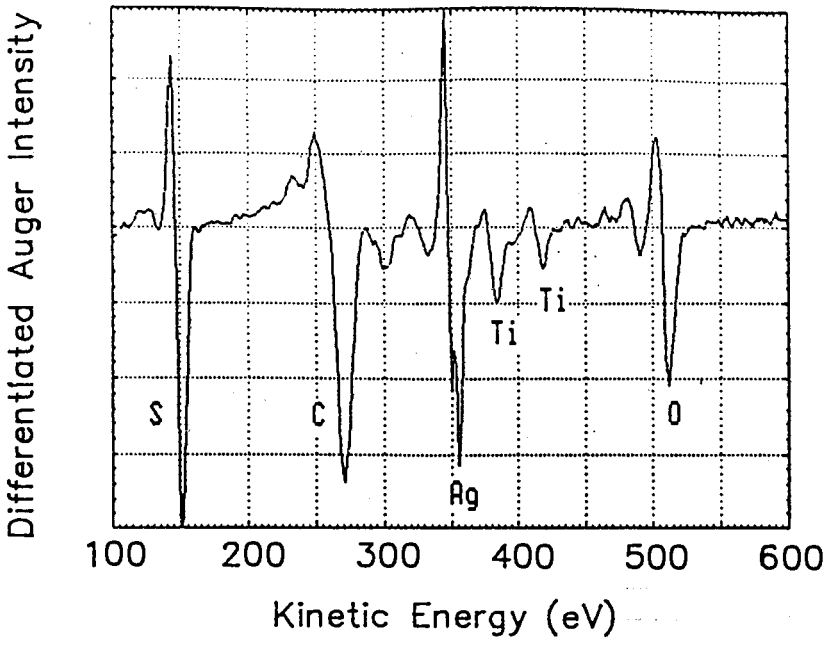
Differentiated Auger Intensity
S
C
Ag
Ti
Ti
O
100
200
300
400
500
600
Kinetic Energy (eV)

(a)

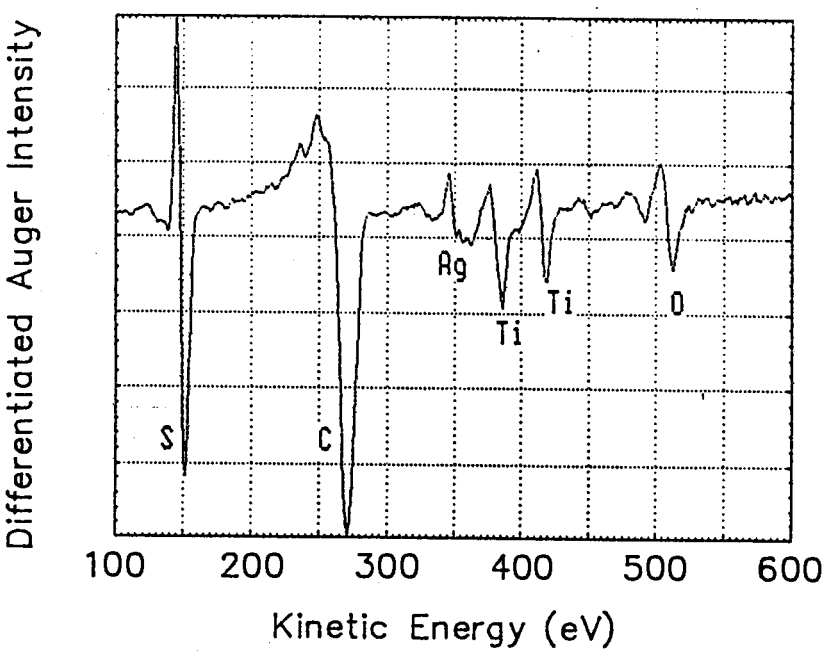
Differentiated Auger Intensity
S
C
Ag
Ti
Ti
O
100
200
300
400
500
600
Kinetic Energy (eV)

(b)

Fig. 5.7

Fig. 5.8 Auger line scan across a surface decoration pattern.

The line scan done nearly parallel to the edge of the crystal shown in Fig. 5.1. The Ag peaks are found to correlate with the dark regions in the surface decoration pattern. Note that S and C are correlated with the Ag and the O is anti-correlated to all three.

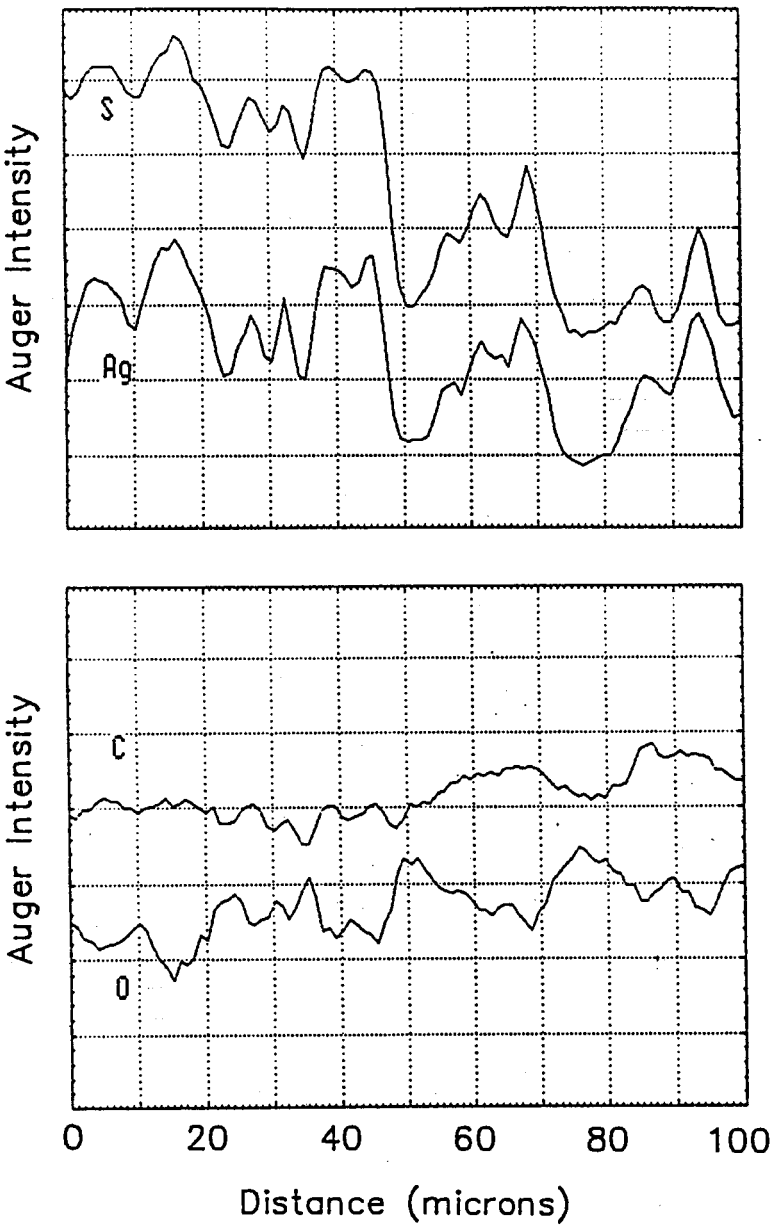
S
Ag
Auger Intensity
C
O
Auger Intensity
0
20
40
60
80
100
Distance (microns)

Fig. 5.8

Fig. 5.9 X-ray diffractograms taken before and after spontaneous deintercalation.

Curve 'a' was taken before deintercalation and curve 'b' was taken after deintercalation. The stage-2 and empty crystal peaks are both in (a), but only the empty crystal peak is present in (b). The shift of the empty crystal peak to a higher angle in (b) is due to an offset in the diffractometer (data taken by P. Joensen).

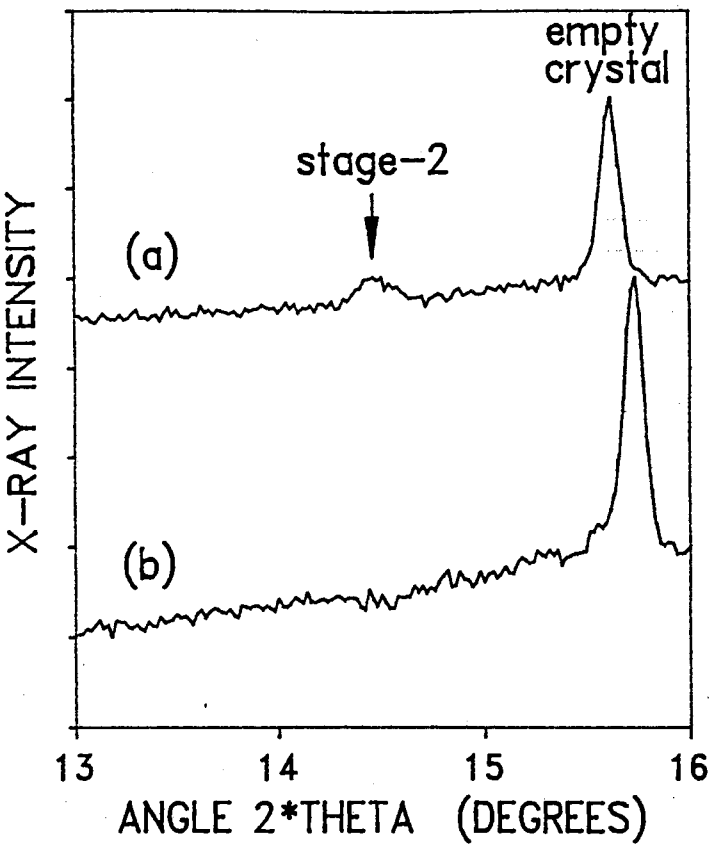
empty
crystal
stage–2
(a)
(b)
X–RAY INTENSITY
13
14
15
16
ANGLE 2*THETA (DEGREES)

Fig. 5.9

CHAPTER 6

MONTE CARLO SIMULATIONS OF INTERCALATION

6.1 INTRODUCTION

The results in Chapters 4 and 5 give experimental details of the macroscopic structure of partially intercalated, stage-2 Ag intercalated TiS_2. The observed structure was in the form of narrow finger-like regions, or channels, which extended from the intercalated crystal edge to the intercalation front. The channels were about 5 μm wide and were spaced about 10 μm apart. A seemingly natural next research step would be to obtain some sort of theoretical understanding of the dynamics of channel formation for Ag_xTiS_2. No analytical model of intercalation kinetics as yet exists so, rather than trying to develop one, Monte Carlo computer simulations of intercalation were performed.

Monte Carlo algorithms are so widely used that only a brief description will be given here. The idea is that one starts with a certain configuration of interacting particles whose total energy is E_i. The configuration is then hypothetically changed, in a random fashion, to another configuration whose energy is E_f. If $E_f \leq E_i$, the system is changed to the new configuration; if $E_f > E_i$ then the system is changed to the new configuration with a probability of $\exp(-(E_f - E_i)/kT)$. Here, k is Boltzman's constant and T is temperature. This procedure is then repeated for as long as one wishes.

By the above description, the Monte Carlo algorithm is quite simple. The most difficult aspect is the determination of how the particles interact, ie. the interaction energy. In addition, once the interactions

are known, a single simulation may take a very long time to run on a computer, in some cases months, depending on the size of the interacting system one wants to describe.

6.2 THE MONTE CARLO MODEL OF INTERCALATION

6.2.1 The Crystal

Setting up an intercalation model that can be used in a Monte Carlo algorithm has been done previously by Kirczenow (see Chapter 1) and more recently by Weber and Butz (50). The idea is that a "crystal" is composed of a 3-dimensional array of allowed sites as shown in Fig. 6.1. The dimensions of the crystal are N_x by N_y by N_z and periodic boundary conditions are applied in the y and z directions. As with Weber and Butz, the lattice of allowed sites is a triangular lattice, which represent the octahedral sites in the TiS_2 galleries - the allowed sites for Ag occupancy (see Fig. 6.2) . The nearest neighbor in plane spacing is 3.4 Å and the nearest neighbor out of plane spacing is 5.7 Å. The intercalate enters the crystal via a reservoir situated at the x=1 edge of the crystal. Once inside the crystal, the intercalate can move only in-plane, since experimentally the intercalate does not pass through the host layers. The edge at $x=N_x$ can be left free so that once a particle reaches that edge it has the opportunity to leave the crystal, or the edge can be clamped. The case of a free edge eliminates the possibility of particles being reflected from that edge, possibly altering the formation of domains early in the intercalation process. Further details of the crystal and reservoir will be given in Sections 6.2.2 and 6.3.1.

6.2.2 The Model Hamiltonian and Reservoir

The interaction of intercalate atoms in a crystal are dominated by elastic and electrostatic effects. The elastic effects are treated in the Safran Hamman model (22). This model, described briefly in Chapter 1, provides an attractive intralayer interaction and a repulsive interlayer interaction. The equation which gives the elastic interaction energy between two spatially separated elastic dipoles is (22):

$$V_{el}(r,z) = -P^2(a_3 r^2 - 2z^2)/4\pi C_{44}(a_3 r^2 + z^2)^{5/2} \qquad (6.1)$$

where: $a_3 = C_{33}/C_{44}$,

C_{33}, C_{44} = elastic constants of host material,

P = elastic dipole strength of an intercalated atom,

r = in plane separation of the dipoles,

z = c axis separation of the dipoles.

Equation 6.1 results from treating the crystal as an anisotropic elastic continuum. Also, the theory deals with particle-particle interactions only, thereby neglecting interference effects.

Electrostatic interactions arise from the charge transfer between the guest and the host upon intercalation. These interactions are always repulsive and are labelled $V_{est}(r,z)$.

With these interactions, the model Hamiltonian is:

$$H = \Sigma V_{el}(r,z) + \Sigma V_{est}(r,z) \qquad (6.2)$$

where the sums are over all pairs of intercalate particles in the "crystal", ignoring double counting.

Equation 6.2 gives the interaction for every two particles <u>in</u> the crystal. How particles enter the crystal is determined by the external reservoir. The reservoir is treated as with Kirczenow (24). Referring to Fig. 6.2; every x=1 site, where y is odd, is a reservoir site. These sites are shown as filled circled in the figure. At any given time, a reservoir site is occupied with a probability

$$P_{rs} = e^{-(E_{rs}-\mu)/kT}/(1+e^{-(E_{rs}-\mu)/kT}) \qquad (6.3)$$

where: E_{rs} = the energy of the intercalate atoms in the reservoir,

μ = the chemical potential of the reservoir with respect to the crystal,

k = Boltzmann's constant

T = temperature.

Particles may only enter the crystal from the reservoir. Once in the crystal, particles do not interact with the particles in the reservoir.

6.2.3 Model Parameters for Ag_xTiS_2

From the above discussion, there are numerous parameters in the Hamiltonian. These parameters should have values which, at least approximately, correspond to Ag intercalated TiS_2. The parameters to determine include P, C_{33}, C_{44}, $V_{est}(r,z)$, E_{rs}, μ, and T. Some of these parameters can be estimated by the known properties of TiS_2. However, to simplify the problem somewhat, the following assumptions are made:

i) Only the octahedral sites are considered. The tetrahedral sites are completely ignored.

ii) Since only stage-1 and stage-2 have been observed is Ag/TiS_2, the interlayer interactions are most likely "short ranged" (as compared to graphite, for example). Therefore, only nearest neighbor interlayer interactions are considered. This is not necessarily true for intralayer interactions, where up to 4^{th} nearest neighbor interactions will be considered.

iii) In the Ag occupied regions of stage-1 and stage-2 Ag/TiS_2, the Ag forms a $\sqrt{3}a_o$ x $\sqrt{3}a_o$ superlattice at about 250 K. This type of superlattice is shown if Fig. 6.2. This superlattice is "fuzzy" at room temperature. It will be assumed that the superlattice does exist (perfectly) at room temperature.

iv) The electrostatic interactions are strongly screened by the host TiS_2, so only nearest neighbor intralayer electrostatic interactions are considered.

The model parameters are now estimated using the above assumptions

along with known experimental data:

(a) From neutron scattering experiments on TiS_2, the elastic constants were determined from phonon dispersion curves (51). The approximate values are:

$$C_{33} \approx 55 \times 10^9 \text{ N/m}^2$$

$$C_{44} \approx 18 \times 10^9 \text{ N/m}^2$$

(b) Kaluarachchi (42) has shown that the stage-2/empty crystal front is "stable" at room temperature, but starts to move into the crystal at about 150°C. This corresponds to an activation energy of the atoms at the front of about 36 meV. Given that the superlattice exists, then an atom at the front has an average of 0 nearest neighbors (nn), 1.5 second nn, 0 third nn and 0 fourth nn. Therefore, using equation 6.1 with the values of C_{33} and C_{44} above gives

$$1.5*V_{el}(\sqrt{3}a_o,0) = -0.036 \text{ eV},$$

where a_o is the nn separation of 3.43 Å. Solving this gives $P \approx 6$ eV.

Another independent way of determining P is by the c-axis expansion of TiS_2 upon intercalation. It has been estimated that P for lithium is about 3.3 eV (52). Also P is proportional to the increase in volume upon intercalation (53) so that

$$P_{Li}/\delta V_{Li} = P_{Ag}/\delta V_{Ag}. \qquad (6.4)$$

Now $\delta V \propto \delta c$ since there is very little change in the a spacing of TiS_2 upon intercalation. Using equation 6.4 with: P_{Li}=3.3 eV, δc_{Li} for $Li_{.4}TiS_2$ is about 0.4 Å (54), and δc_{Ag} for $Ag_{.4}TiS_2$ is about 0.75 Å, gives P≈6 eV, in agreement with the above value.

(c) At this point the elastic parameters are known (although there are some problems which will arise shortly), and there remains the electrostatic and reservoir parameters to obtain. To estimate the electrostatic parameters, one must turn to the applied voltage vs. Ag fraction curve. This was shown previously in Fig. 3.2 and is shown again, with added details, in Fig. 6.3.

Referring to Fig. 6.3: Between x=0.33 (a "perfect" $\sqrt{3}a_o x \sqrt{3}a_o$ superlattice, stage-1 phase) and x=0.4 there is a sudden drop in the curve. The voltage change of this drop is about 0.045 V. This indicates that at x=0.33, the energy difference to add another Ag atom is 0.045 eV. Where does this atom go? It must fill in the vacancies in the superlattice. Therefore, as an approximation, 0.045 eV is three times the nearest neighbor interaction energy. So from equation 6.2,

$$3[V_{el}(a,0) + V_{est}(a,0)] = 0.045 \text{ eV}.$$

Using the known elastic parameters gives

$$V_{est}(a,0) \approx 0.14 \text{ eV}.$$

To obtain the interlayer electrostatic parameter, again one must refer to Fig. 6.3. Between x=0.17 ("perfect" stage-2 with

a $\sqrt{3}a_o x \sqrt{3}a_o$ superlattice) and x=0.2 there is also a sudden drop in the curve. The voltage change is about 0.03 V. So at this point the energy difference to add an additional atom at x=0.17 is 0.03 eV. Where does the atom go? It must start to fill the empty galleries so that a stage-1 starts to form. The atom interacts with 2 nn interlayer sites, but each site is occupied with a probability of 1/3. Therefore,

$$(2/3)*[V_{el}(0,c) + V_{est}(0,c)] = 0.03 \text{ eV}. \qquad (6.4)$$

Now the aformentioned problem arises. Using c=5.7 Å, then from Eq. 6.1, $V_{el}(0,c) \approx 0.25$ eV. Therefore, $V_{est}(0,c)$ must be negative, which corresponds to an attractive interaction between two identically charged particles. This is obviously unrealistic and some changes must be made. This inconsistency is most likely due to a failure of the Safran Hamman model. Recall that this model assumes an elastic continuum. This cannot be realistic when dealing with atomic scale interactions lengths. However, the Safran Hamman model may be sufficient for the intralayer interactions since the values of P calculated from two independent methods agree quite well. This intralayer agreement may be due to the fact that TiS_2 layers are relatively stiff as far as intercalation compounds are concerned. This stiffness would cause the layers to appear as more of a continuum as compared to, say, graphite. The solution to this inconsistency problem will be to use the Safran Hamman model for intralayer

interactions and equation 6.4 for interlayer interactions.

(d) E_{rs} is a parameter about which virtually nothing is known. For this reason it will be left as a free parameter. The chemical potential can be adjusted as appropriate in order to change the equilibrium properties of the intercalation. Most often, μ will be set to zero, since this corresponds to a short circuit intercalation cell.

(e) The temperature will normally be set to room temperature since this was the temperature used for all experiments.

This completes the parameter estimation. These parameters are meant to represent a starting point for the simulations, and their values will be adjusted in order to (hopefully) obtain channel-like domain structures.

6.3 INTERCALATION SIMULATIONS

6.3.1 Computer Program Details

A version of the computer program written is shown in Appendix B. The following provides a brief algorithm of the program.

Lattice sites are given the value 1 if they are occupied and 0 if they are not. The reservoir sites behave just as the lattice sites except that they do not have a definite occupancy. They are instead occupied at all times according to the probability given by Eq. 6.3. So starting from a given initial condition of the lattice site occupancy, an occupied site is chosen at random along with a random direction for movement. If the nearest neighbor site in this direction is occupied then another occupied site is chosen at random, otherwise a trial move to this empty nearest

neighbor site is hypothetically made. The energy of the system before and after the hypothetical move is calculated from Eq. 6.2. This hypothetical move is then actually made (or not) according to the Monte Carlo algorithm described is Section 6.1. This procedure is continued for a given number of user defined steps. One Monte Carlo Step (MCS) is defined as one trial move. Due to the number of MCS used to complete a simulation, a more useful measure of time is one million Monte Carlo steps (MMCS).

Throughout the following sections, the starting configuration of the crystal is an empty crystal, unless otherwise stated.

6.3.2 Short Circuit Intercalation

6.3.2.1 Channel Formation

Intercalation simulations with μ=0 mimic a short circuit intercalation cell. Since the short circuit cell was the most commonly used experimental intercalation method, most simulations were performed under these conditions.

In order to avoid being tedious when quoting parameter values, the procedure used will be that only parameters that are changed from simulation to simulation will be mentioned in the text. All other parameters that remain unchanged will be shown in the figure captions. Also, all simulations in this section start from an initial configuration corresponding to an empty crystal.

As a start, the parameter values were chosen as the values stated in Section 6.2.3. That is: C_{33}=55x10^9 N/m^2, C_{44}=18x10^9 N/m^2, P=6 eV, T=293 K, $V_{est}(a,0)$=0.14 eV, the total nearest neighbor out of plane

interaction at 0.045 eV, and μ=0. The only parameter remaining is E_{rs}. As was mentioned this has been left as a free parameter and its value remains somewhat arbitrary. But initially, since the simulation will be done at room temperature, E_{rs} is taken to be 0.025 eV (the "energy" of room temperature). The size of the lattice is N_x=60, N_y=60, and N_z=6. Recall that periodic boundary conditions are applied in the y and z directions. The results of the simulation are shown in Fig. 6.4. Each column shows the 6 galleries of the crystal at a particular time. A dark circle indicates that a lattice site is occupied. The reservoir is in contact with the left edge of each gallery and is not explicitly shown. The right hand edge of each gallery is "free", allowing particles to leave the crystal at that edge. This method of presentation will be used for all simulation figures unless otherwise stated. Columns a-f correspond to the intercalant distribution in the crystal after 2, 4, 6, 8, 10, and 20 MMCS respectively.

As can be seen in the figure, early in the intercalation process (column a) each gallery starts to fill with intercalant and a fairly flat intercalation front exists. The density of intercalant in the intercalated region is quite uniform except for some small, local, high-density regions. As intercalation progresses, these high density regions become larger and start to extend farther into the crystal (columns b and c) and visual evidence of stage-2 regions appear. These stage-2 regions are channel-like in nature and merely "grow" farther into the crystal with increasing intercalation time (columns d, e, and f). A stage-1 band is always present near the crystal edge. There are two channels per gallery and the corresponding "wavelength", or lengthscale, is 30 lattice spacings. These channels show a striking similarity to the channels observed

experimentally.

It is very interesting that intercalation channels formed so readily in the simulations. Besides the similarities to the experimentally observed domain structure mentioned above, there are obvious differences as well. These include: the local in-plane density of intercalant is 1 rather than the observed 0.4. Also the channel spacing is 30 x 3.4 Å ≈ 100 Å as compared to the experimentally observed 10 μm; a factor of 1000 difference.

Another possible difference concerns the regions of particle transport during intercalation. Although it was never explicitly monitored during simulations, it seems likely that the particle transport occurs along the edges of channels. This is about the only place for transport to occur since in the middle of a channel there are few vacant sites available for particle movement. Transport along channel boundaries is contrary to the idea that the transport occurs in the middle of a channel (since experimentally about 60% of the octahedral and 100% of the tetrahedral sites are vacant for such transport). This type of mid-channel transport is indicated from experimental radioactive tracer results (20). A failure of mid-channel transport in the simulations may be caused by the neglect of the tetrahedral sites (see Chapter 7).

6.3.2.2 Lengthscale versus Crystal Size

To ensure that the periodic boundary conditions are not "forcing" a particular lengthscale, the size of the crystal was doubled in the y direction (N_y=120), while keeping all other parameters fixed (also N_x was changed to 40, although, given that the x=40 edge is unclamped, this change

would not affect the lengthscale in the y direction). The results are shown in Fig. 6.5. All 6 galleries are shown, but only at one time; 22.5 MMCS. There are 4 channels per gallery, giving a lengthscale of 30 lattice spacings. So it appears that the crystal size has little, or no, effect on the lengthscale.

6.3.2.3 Channel Dependence on Reservoir Energy

Since the only completely arbitrary parameter in the model is E_{rs}, it is worthwhile to vary this parameter; in essence to observe how sensitive the channels are to its value. So with all other parameters remaining fixed, E_{rs} was varied from 0.025 eV to -0.025 eV. There was effectively no change in the channels. As E_{rs} was changed, the lengthscale varied between 24 and 30 lattice spacings but not in any systematic fashion, indicating that the changing scale was most likely a fluctuation. For example, Fig. 6.6 shows a simulation for E_{rs} = -0.025 eV. The 6 galleries are shown after 22.5 MMCS. This figure is to be compared to Fig. 6.5.

Since the properties of the channels did not appear to change by varying E_{rs} between 0.025 and -0.025 eV, E_{rs} was kept at the value of 0.025 eV for all remaining simulations.

6.3.2.4 Channel Dependence on P and V_{est}

In Section 6.2.3, the elastic and electrostatic parameters for Ag_xTiS_2 were estimated from experimental data. Needless to say, these were only estimates, and different values should be attempted. In this Section, the elastic dipole strength, P, and the nearest neighbor intralayer electrostatic repulsion, V_{est}, are varied in a systematic fashion in order

to explore a small portion of the "phase diagram" of channel existence. Since there are a tremendous number of simulations involved, for the sake of brevity, only a limited number will actually be shown.

With E_{rs}=0.025 eV, V_{est} was increased slightly to 0.145 eV and P was changed from 6 to 5.25 eV (recall Fig. 6.5 shows the channel formation at V_{est}=0.14 eV, P=6 eV). This increase in V_{est} and reduction in P relates to an overall decrease in the intralayer attraction. The intercalant distribution in 3 consecutive galleries of the crystal, after 30 MMCS, is shown in Fig. 6.7 column a. As can be seen the channels do not exist. In fact, no discernible intercalate distribution pattern is evident. This lack of channels is not surprising since a decrease in the intralayer attraction would decrease the probability of large islands of intercalant forming. Note, however, that a $\sqrt{3}$ x $\sqrt{3}$ superlattice (or an x=1/3 superlattice) exists in the occupied regions. (For a more magnified look at this type of superlattice (and an x=2/3 superlattice), see Fig. 6.15). To attempt to recover channel domains, V_{est} was then decreased to the values 0.1120, 0.1100, 0.1095, 0.1080, 0.1050, and 0.0950 eV. The intercalant distributions for each value of V_{est} are shown in Fig. 6.7 columns b-g respectively. Each distribution shows 3 consecutive galleries of the crystal after 30 MMCS.

Referring to Fig. 6.7: when V_{est} is reduced to 0.112 eV still no channels exist, but x=1/3 and x=2/3 superlattices coexist. At V_{est} = 0.110 eV there is a "hint" that some sort of channel structure is on the verge of forming. At the same time there are x=1/3 and x=2/3 superlattices that exist, along with high density x=1 regions. However, at V_{est}=0.1095 eV, the channel structure is definitely evident and the

lengthscale is about 60 lattice spacings. Both superlattices still exist, but the distribution is mainly the high density x=1 form. A further decrease in V_{est} merely solidifies the channel structure, decreases the lengthscale down to about 20 lattice spacings at V_{est}=0.095 eV, and eliminates the superlattice ordering.

This transition from channels to no channels occurs quite sharply. The transition occurred for V_{est} between about 0.112 and 0.1095 eV. Along with the value of P=5.25 eV, the transition occurs when the total nearest neighbor intralayer interaction energy changes by about 3%. (It is interesting that this same transition occured when E_{rs} was set at -0.025 eV). The transition appears to be depend on the formation of x=1 regions, since the onset of channels occurs with the onset of high density regions.

Another property of the intercalating systems that changed with V_{est} was the concentration of intercalant in the crystal. This dependence is shown in Fig. 6.8 where the concentration is plotted vs. V_{est}. The concentration was measured after 30 MMCS in each case. There is a drastic increase in the concentration right near the transition point ($V_{est}\approx$0.110 eV). Therefore, the creation of channels is accompanied by an increase in the intercalant concentration. However, a word of caution. Recall that the far edge of the crystal is free, allowing intercalant to leave the crystal, so the above concentration is not necessarily a measure of the total amount of intercalant that has entered the crystal, but a measure of the density of the intercalant in the intercalated region.

To obtain additional transition points, different values of P were

then attempted, combined with varying V_{est}. All of these transitions were also very sharp. The transition points are plotted on a P. vs. V_{est} curve shown in Fig. 6.9(a). As is seen by the figure, the points can be connected by a smooth line. Above the line, channel domains form, below the line they do not.

6.3.2.5 Channel Dependence on Temperature

Naturally, if a simulation at room temperature produces channel structures, then an increase in temperature should eventually destroy them. This is expected due to the increased amount of disorder with temperature.

The starting parameters were P=5.25 eV, V_{est}=0.095 eV, and T=293 K. It is worth noting that with this parameter set, the channels are very "rigid" (see Fig. 6.7 column g). The temperature was then increased, keeping all other parameters constant. The intercalant distributions as a function of temperature are shown in Fig. 6.10 columns a-g for temperatures of 325, 450, 550, 650, 675, 700, and 725 K respectively. Three consecutive galleries per simulation are shown and the duration of each simulation was 30 MMCS. The figure indicates that at around 725 K the channels have disappeared. This high temperature is required since the channels were so "rigid" to begin with. Note from the figure that the lengthscale tends to increase with temperature until the channel-like structures finally disappear.

The intercalant concentration in the crystal as a function of the temperature at which the crystal was intercalated is shown in Fig. 6.11. Each data point was obtained after 30 MMCS. There does not appear to be any sharp transition associated with the disappearance of channels in this

case.

6.3.2.6 Channel Dependence on Interlayer Interactions

Intercalation channels seem to appear readily in the intercalation simulations. However, channels, or finger-like, structures also appear in two dimensional diffusion systems (55), that is without any coupling in the third dimension, but only if an external driving field exists. Therefore, since no external driving field is present in our simulations, one would expect the intercalation channels to disappear if the interlayer interactions were "turned off". In the simulations, the temperature was restored to room temperature and simulations were done with varying interlayer repulsion energies. The expected disappearance of channels does occur and is shown in Fig. 6.12. The intercalant distributions as a function of the interlayer repulsion are shown in columns a-f for interlayer energies of 0.045, 0.035, 0.025, 0.015, 0.005, and 0.0 eV respectively. The remaining parameter values are in the figure caption. Three consecutive galleries are shown for each simulation and the time for each simulation was 30 MMCS. Besides the disappearance of channels as the interlayer interactions are turned off, the lengthscale also increases. The lengthscale for the interlayer interaction at 0.005 eV is about 60 lattice spacings, or about 200 Å.

6.3.3 Intercalation at a Non-Zero Chemical Potential

Equation 6.3 relates P_{rs}, the probability that a reservoir site is occupied, to the value of the chemical potential, μ. As μ is decreased, P_{rs} is decreased and so the reservoir has fewer occupied sites. This has

the effect of decreasing the equilibrium concentration of the intercalate in the crystal. For example, experimentally, if an external voltage of 0.05 V is applied to the Ag/TiS_2 intercalation cell, stage-1 no longer appears at the crystal edge during intercalation, and only a stage-2 band is present (see Fig. 6.3 and Chapter 3). This voltage corresponds to a chemical potential of μ = -0.05 eV.

The simulations in this section were done with the interlayer repulsion reset to 0.045 eV.

From the results of μ=0 simulations, a stage-1 region does exist at the intercalating crystal edge. So reducing μ should destroy this stage-1 band and give only stage-2. Fig. 6.13 columns a-d shows how the intercalation channels appear for μ=-0.025, -0.04. -0.07, and -0.10 eV respectively. The other parameters are shown in the figure caption. Three consecutive galleries are shown for each simulation. The time for each simulation was 20 MMCS, except for column (a) which was 22.5 MMCS. As the chemical potential is decreased, stage-1 disappears at the intercalating crystal edge (column (a)) and only a stage-2 band is present. Note that channels exist when the crystal intercalates directly as stage-2. As μ is reduced to -0.10 eV (column (d)) essentially no intercalant enters the crystal - i.e. the crystal does not intercalate. This is expected experimentally since the open circuit potential of the Ag/TiS_2 intercalation cell is about 0.10 - 0.12 V. Also, there is an indication of the lengthscale increasing as μ decreases.

6.3.4 Deintercalation

Deintercalation simulations are performed by initially filling up the crystal entirely. The chemical potential is then set to -0.17 eV. This corresponds to an experimentally applied voltage of 0.17 V; the voltage required to deintercalate a crystal (see Chapter 3). For these deintercalation simulations, the right edge of the crystal was no longer "free". It was "clamped" so that intercalant could only leave the crystal via the reservoir.

The results of deintercalation are shown in Fig. 6.14. The parameter values, as usual, are in the figure caption. The figure shows that the crystal deintercalates via a stage-2 band propagating in from the crystal edge. The stage-2 region is channel-like in nature. These results are consistent with experimental observations.

6.3.5 Low Density Channels

All of the simulation results shown which contain channel-like structures also contain high density (x=1) regions. It is known that experimentally, the occupied regions have a density of about x=0.4. Therefore, attempts were made to obtain low density channels. What is meant by low density is not necessarily x=0.4, but rather x being (locally) substantially lower than 1.

To find a region of phase space that would hopefully give low density channels (if they exist at all), the following procedure was adopted: Change the intralyer interactions so that an x=1/3 superlattice formed in the occupied regions (similar to Fig. 6.7(a)), then adjust the interlayer

interactions so that channels form. Low density channels were found to form, as shown in Fig. 6.15, with the following parameter set; P=8 eV, V_{est}=0.3 eV, V_{o1}=0.025 eV, V_{o2}=0.008 eV (see below), and all other parameters are "ususal" and are shown in the figure caption. In order to obtain low density channels with these in-plane parameters, it was necessary to increase the range of the interlayer interactions. V_{o1} is the nearest neighbor out of plane interaction (i.e. atoms separated by a distance 5.7 Å along the c-axis), and V_{o2} is the second nearest neighbor out of plane interaction (i.e. atoms separated by a distance 5.7 Å along the c-axis, and 3.4 Å along the a-axis).

Fig. 6.15 shows the intercalant distribution in the galleries after 36 MMCS. The low density channels consist mainly of a x=1/3 superlattice, with a small amount of x=2/3 superlattice near the crystal edge. There are 4 fingers per gallery, stage-1 exists near the crystal edge, and stage-2 exists near the intercalation front.

No phase transition or temperature dependence of channel formation simulations were performed for low density channels.

6.3.6 "Long" Intercalation Times and Channel Merging

Of all the simulations performed, the timescale on which the intercalant distributions were examined never varied by a considerable amount. In some cases it was as short as 2 MMCS and in others as long as 36 MMCS. A natural question is: how do the channels change with the duration of intercalation? Initial simulations set up for long intercalation times revealed a problem: the channels grew into the crystal, but once they reached a certain length, they stopped. However, the larger

the crystal in the channel growth direction (the x direction), the longer this "steady state" channel length. This indicated that the boundary condition at $x=N_x$ could be presenting a problem.

For all of the intercalation simulations shown up to this point, the boundary condition at $x=N_x$ was that it was "free", or unclamped. This allowed particles to leave the crystal so that they would not be "reflected". This boundary condition was meant to mimic a large crystal. What it also allowed, however, was a steady state channel configuration to be reached: the net rate that particles entered the crystal from the reservoir equalled the net rate at which particles broke away from the channels, which equalled the rate at which particles left the crystal at $x=N_x$. This steady state channel length is not what is observed experimentally and it is easy to understand why this "free edge" boundary condition does not properly mimic a large crystal. Consider a particle at $x=N_x$, this particle is basically doing a random walk (due to the low particle density away from the channel regions) and can move to the right or the left with equal probability. If it moves to the right it is lost forever, if it moves to the left it has a chance to re-attach to the channels, making them longer. Therefore, if the length of the crystal was changed to N_x+1, a particle moving to the right at $x=N_x$ is not neccessarily lost, but still has a chance to return. This is why a larger crystal could sustain longer steady state channels - statistically, more particles that initially broke away from the channels returned via a "random walk". The solution to this problem was to increase the size of the crystal in the x direction and to clamp the $x=N_x$ end.

Fig. 6.16 shows the intercalant distributions in a 4 gallery crystal

that was intercalated for a relatively long time. The parameters were chosen for high density channels and are shown in the figure caption. In the discussion that follows, whenever gallery one is referred to, similar activities are also occuring in gallery three, even though it will not be explicitly mentioned. Similarly for galleries two and four.

Referring to Fig. 6.16: three of the four galleries of the crystal are shown, and columns a-j correspond to 20, 40, 60, 80, 100, 120, 140, 160, 180 and 200 MMCS respectively. Early in the intercalation process (columns a) there are 6 channels per gallery. This lengthscale was commonly observed in simulations with the same parameter set and at similar intercalation times. However, by 40 MMCS (column b) two of the channels in the first gallery start to merge near the intercalation front. This results in the channel in the second gallery (between the merging channels) becoming "pinched off" and receding. This type of merging is seen again in the second gallery after 60 MMCS (column c), however, as is seen this merge fails by 80 MMCS (column d). In addition, by 80 MMCS the channels in the first gallery, which initially merged, are now also merging with a third. The net effect is seen by 120 MMCS in column f, where there are now only four channels per gallery. Another merge is starting in gallery one at 140 MMCS. This merge continued, but was not completed, by 200 MMCS (column j). In the merges, the general situation is that the empty region between merging channels fills in with time and the respective channels in the other adjacent layers recede back into the stage-1 region near the crystal edge. Thus, in this particular simulation, what started out as 6 channels at 20 MMCS resulted in effectively 3 channels after 200 MMCS. Presumably if the simulation continued longer the lengthscale would continue to

increase. More comments on the lengthscale and channel merging are given in Chapter 7.

Fig. 6.1 Schematic of the crystal used in Monte Carlo simulations. There are N_z galleries, each of size N_x by N_y. The allowed intercalant sites in the xy plane form a triangular lattice. Intercalant can enter and leave the crystal via the reservoir at the plane x=0.

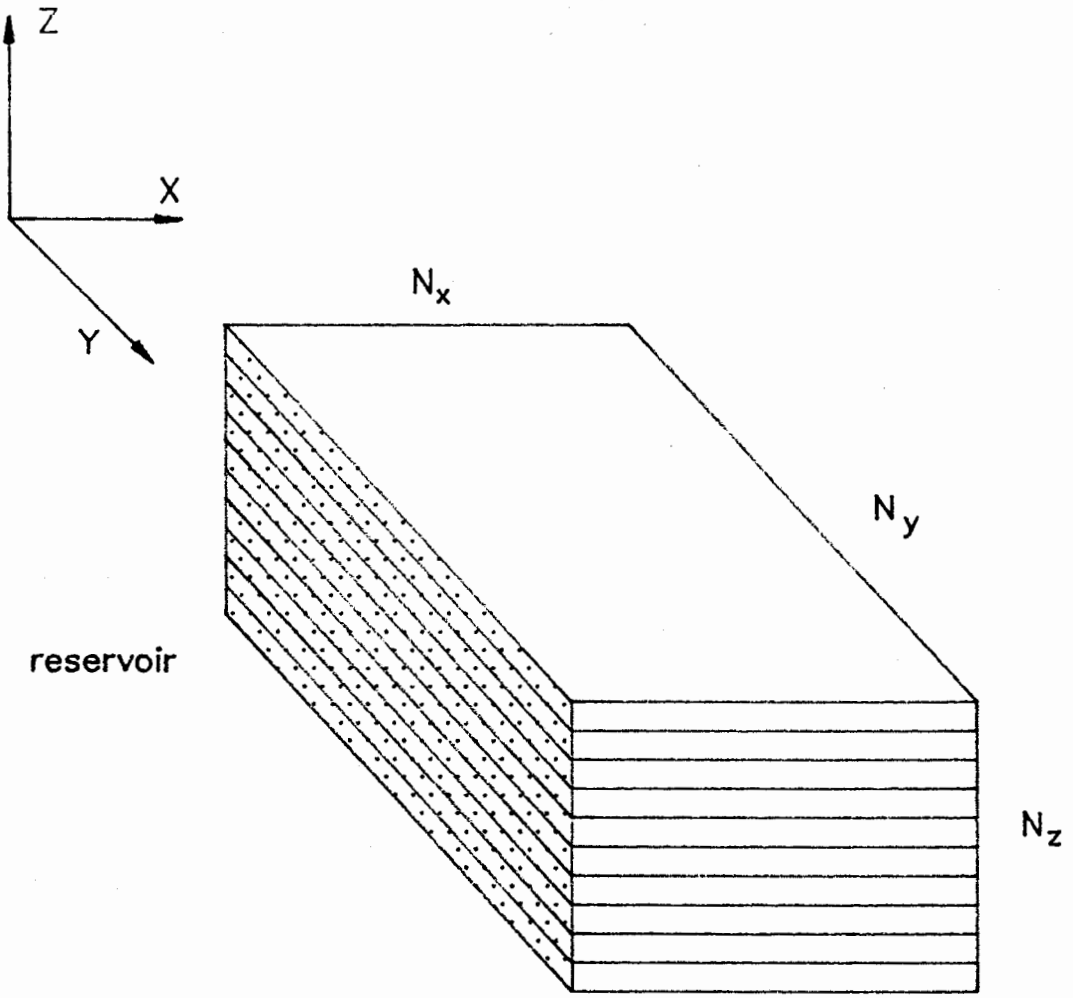

Fig. 6.1

Fig. 6.2 The in-plane and reservoir sites of the crystal used in simulations. At the left edge (x=1), the filled circles represent the reservoir sites. The reservoir sites are the same for every layer. The hatched circles form a $\sqrt{3} \times \sqrt{3}$ superlattice.

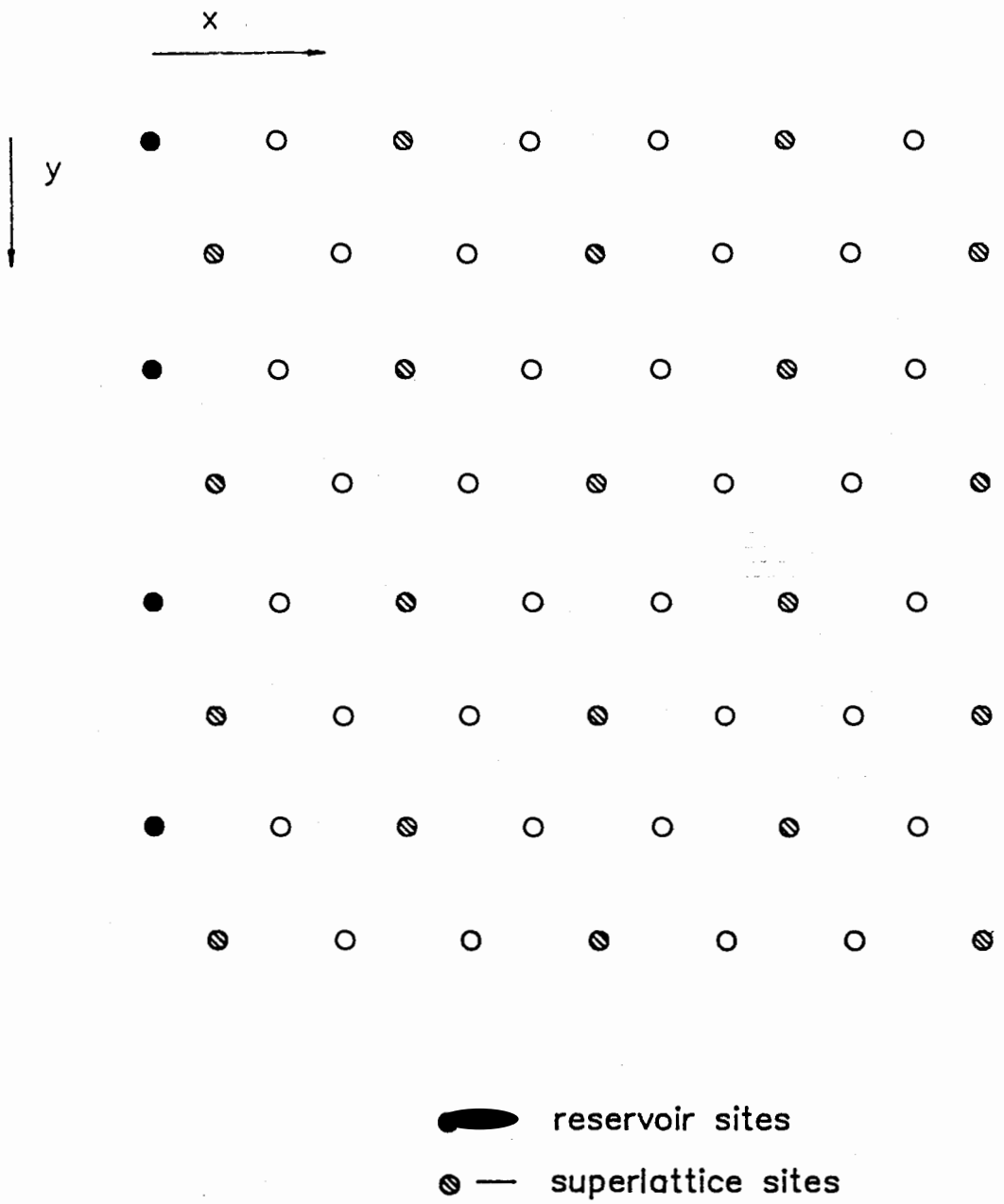

Fig. 6.2

Fig. 6.3 Chemical potential versus x for Ag_xTiS_2. The 0.03 eV step at x=0.17 is related to the out of plane interactions. The 0.045 eV step at x=0.33 is related to the in plane interactions (see text).

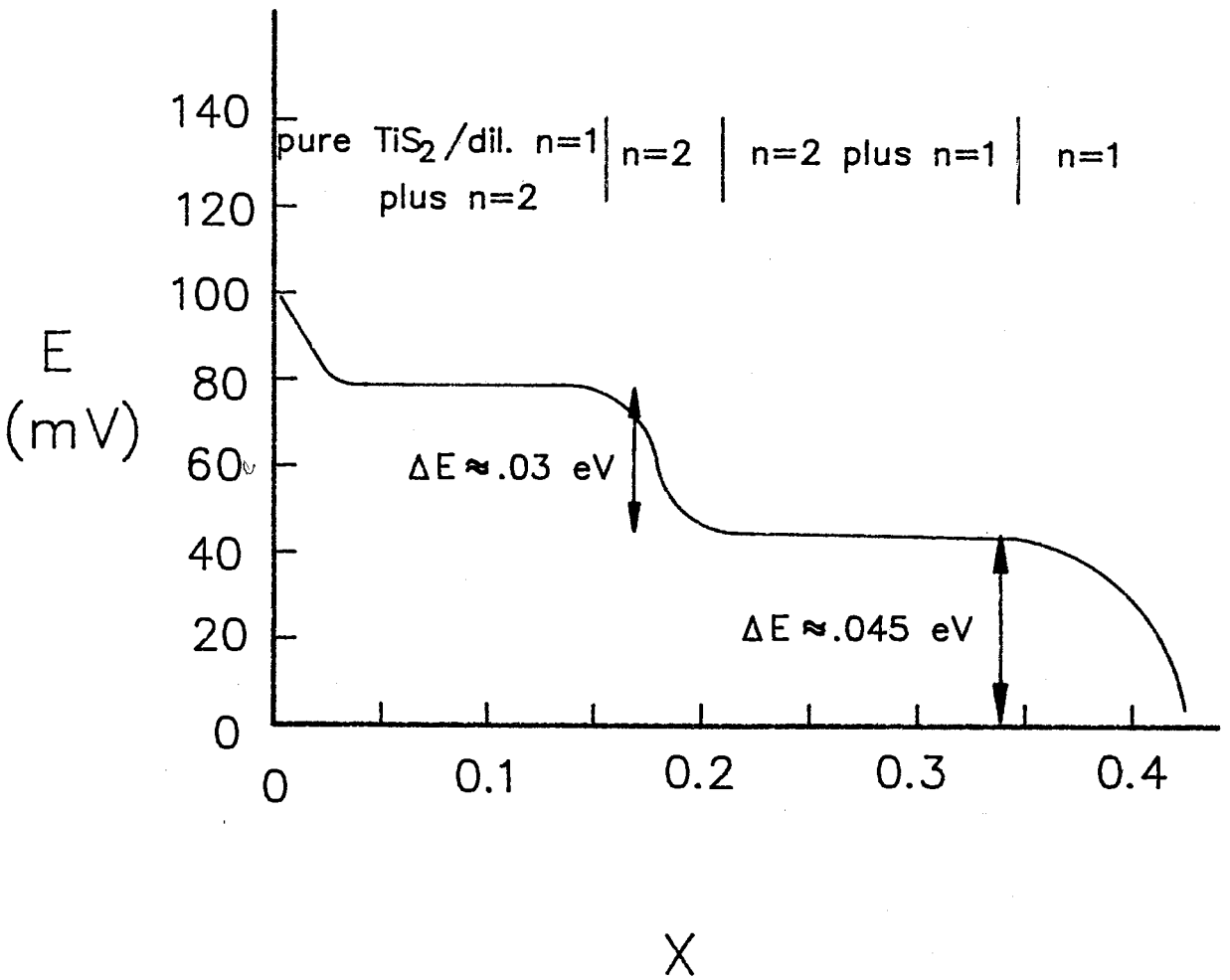
Ag_xTiS_2 /0.1M $AgNO_3$ /Ag
pure TiS_2 /dil. n=1 plus n=2
n=2
n=2 plus n=1
n=1
ΔE ≈ .03 eV
ΔE ≈ .045 eV
E (mV)
140
120
100
80
60
40
20
0
0
0.1
0.2
0.3
0.4
X

Fig. 6.3

Fig. 6.4 Intercalation simulation starting with an empty crystal. Each column represents the galleries of the "crystal" at a different time. Time increases from column a to column f. The formation of stage-2 channels is evident.

Parameter set: $C_{33}=55\times10^{9}$ N/m^2, $C_{44}=18\times10^{9}$ N/m^2, P=6 eV, $V_{est}(a,0)=0.14$ eV, out of plane interaction is 0.045 eV, $\mu=0$, T=293 K, $E_{rs}=0.025$ eV.

Lattice size: $N_x=60$, $N_y=60$, $N_z=6$.

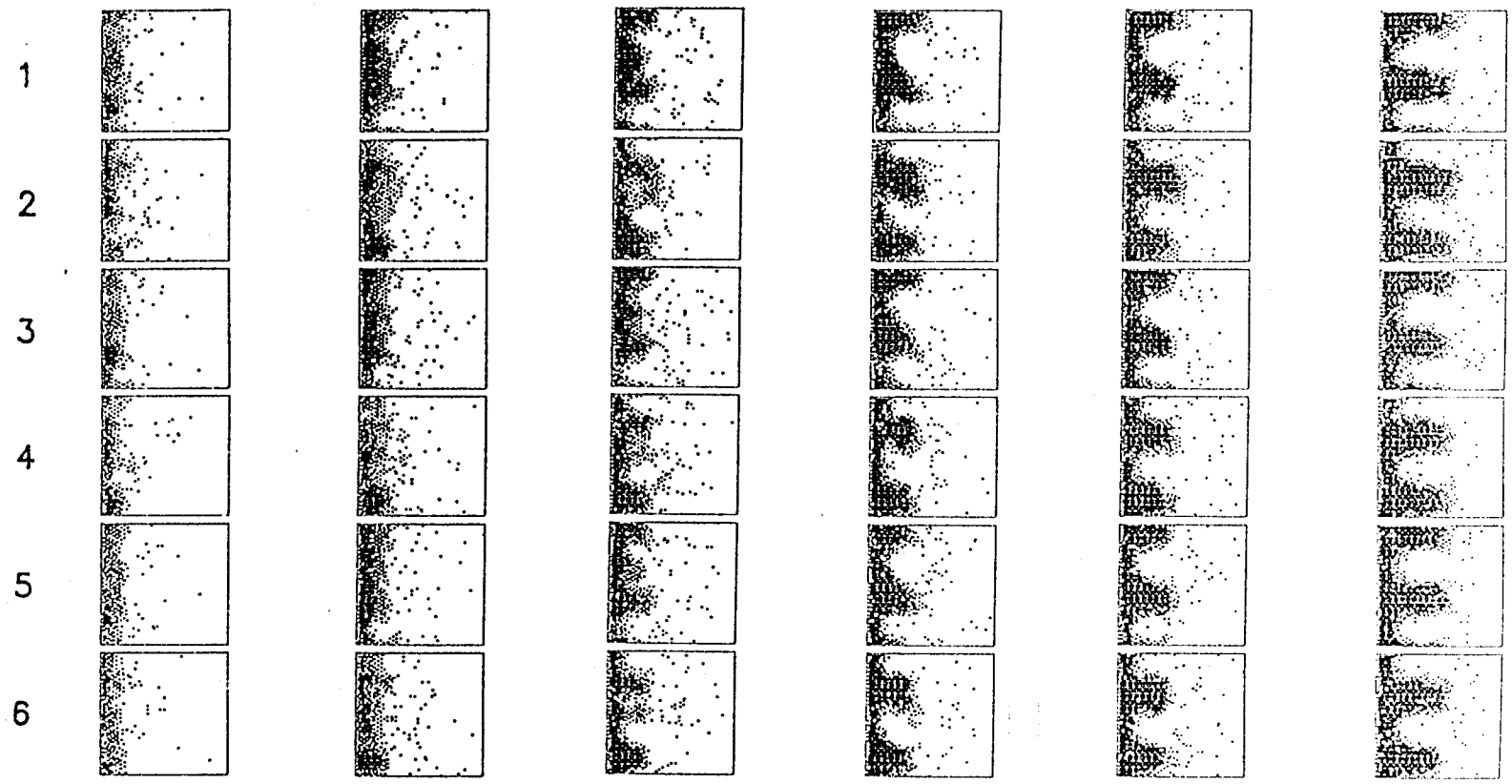

Fig. 6.4

Fig. 6.5 Channel dependence on crystal size. Shown are six galleries of a crystal after 22.5 MMCS. The parameters are the same as in Fig. 6.4, except for the changing lattice size.

Parameter set: $C_{33}=55\times10^9$ N/m^2, $C_{44}=18\times10^9$ N/m^2, P=6 eV, $V_{est}(a,0)=0.14$ eV, out of plane interaction is 0.045 eV, $\mu=0$, T=293 K, $E_{rs}=0.025$ eV.

Lattice size: $N_x=40$, $N_y=120$, $N_z=6$.

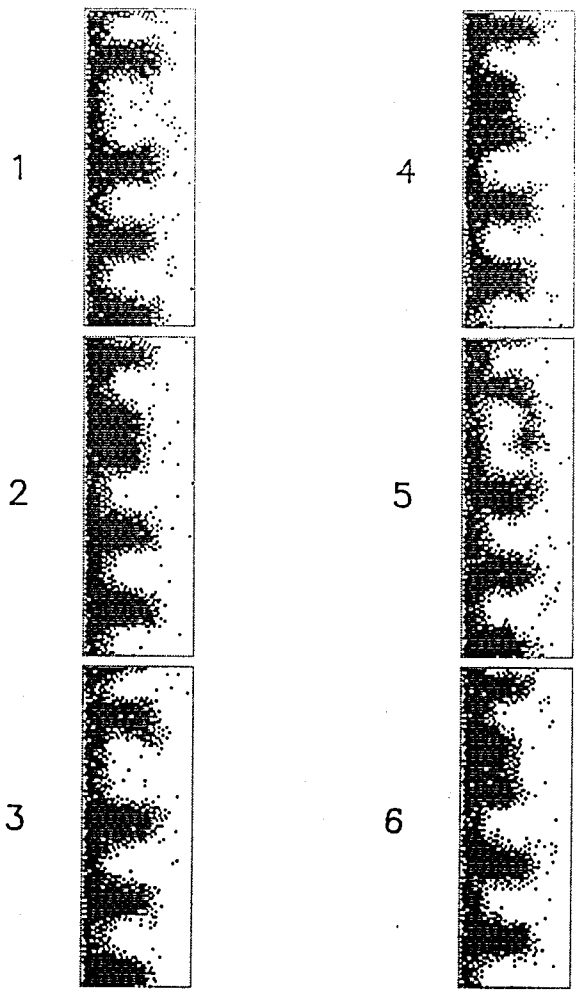

Fig. 6.5

Fig. 6.6 Channel dependence on the reservoir energy. Shown are six galleries of a crystal after 22.5 MMCS. The parameters are the same as in Fig. 6.5, except for a different E_{rs}.

Parameter set: C_{33}=55x10^9 N/m^2, C_{44}=18x10^9 N/m^2, P=6 eV, $V_{est}(a,0)$=0.14 eV, out of plane interaction is 0.045 eV, μ=0, T=293 K, E_{rs}=-0.025 eV.

Lattice size: N_x=40, N_y=120, N_z=6.

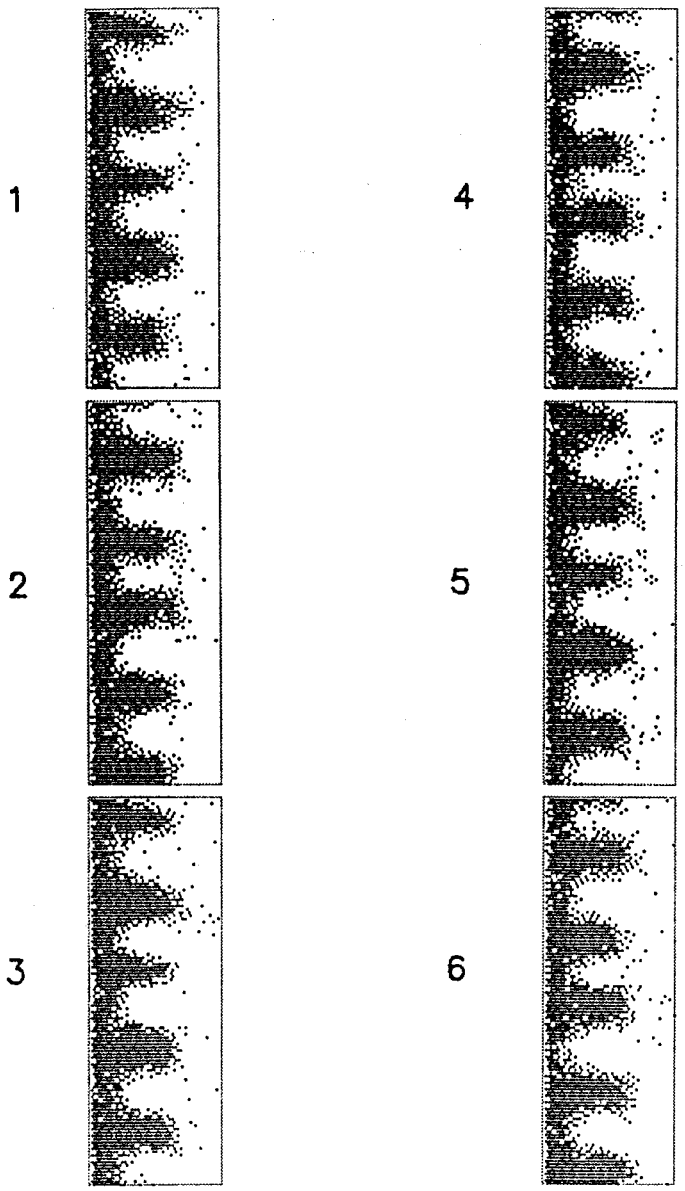

Fig. 6.6

Fig. 6.7 Channel dependence on in plane electrostatic interactions. Each column represents the galleries of simulation with different values of V_{ext}. The time for each simulation was 30 MMCS. Only 3 of the 6 galleries are shown.

Parameter set: $C_{33}=55\times10^9$ N/m^2, $C_{44}=18\times10^9$ N/m^2, P=5.25 eV, out of plane interaction is 0.045 eV, μ=0, T=293 K, E_{rs}=0.025 eV. V_{est}=0.1450, 0.1120, 0.1100, 0.1095, 0.1080, 0.1050, 0.0950 for columns a-g respectively.

Lattice size: $N_x=40$, $N_y=120$, $N_z=6$.

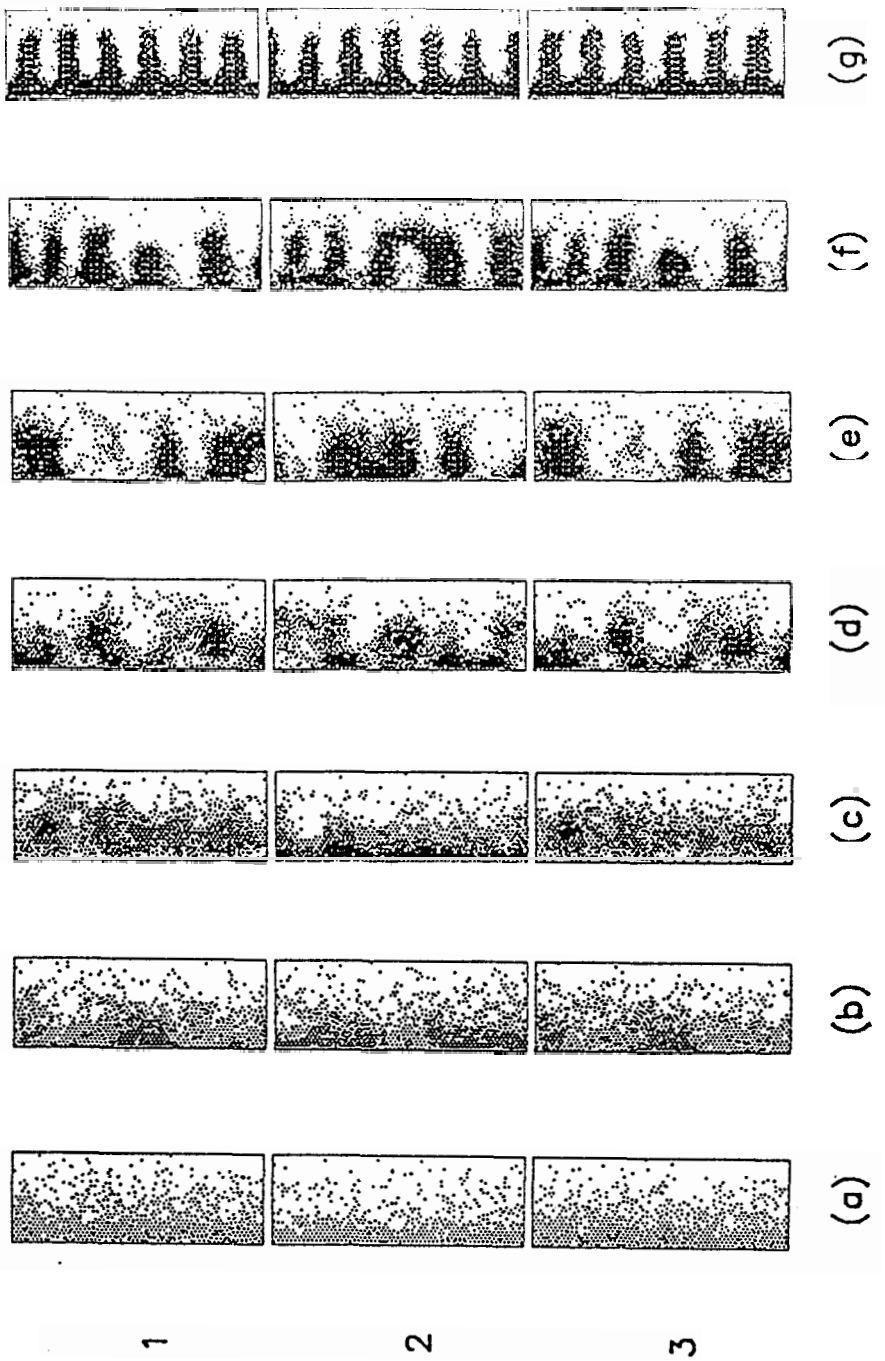

Fig. 6.7

Fig. 6.8 A plot of the intercalant concentration in the crystal as a function of the in plane electrostatic interaction. The data was obtained from the simulations times shown in Fig. 6.7. When compared to Fig. 6.7, the sudden increase of the concentration occurs when the channels form. Error bars are missing due to lack of statistics.

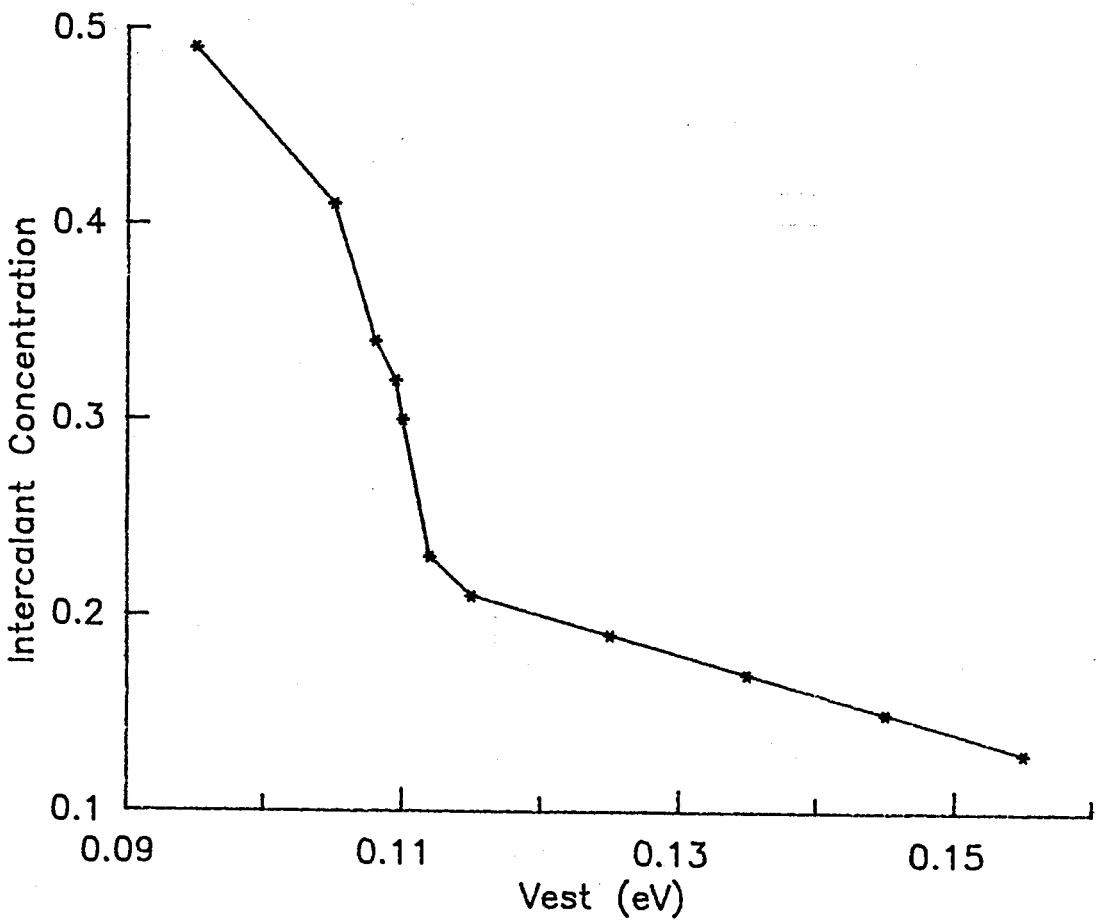
0.5
0.4
0.3
0.2
0.1
Intercalant Concentration
0.09
0.11
0.13
0.15
Vest (eV)

Fig. 6.8

Fig. 6.9 A portion of the channel phase diagram. Shown is a plot of the elastic dipole strength (P) versus V_{est}. The data points indicate the transition point from channels to no channels. The remaining parameters are as in Fig. 6.7. The data points were determined by a visual inspection of channel formation, so no formal error analysis was performed. The uncertainty in V_{est} is about $\pm$ .002 eV.

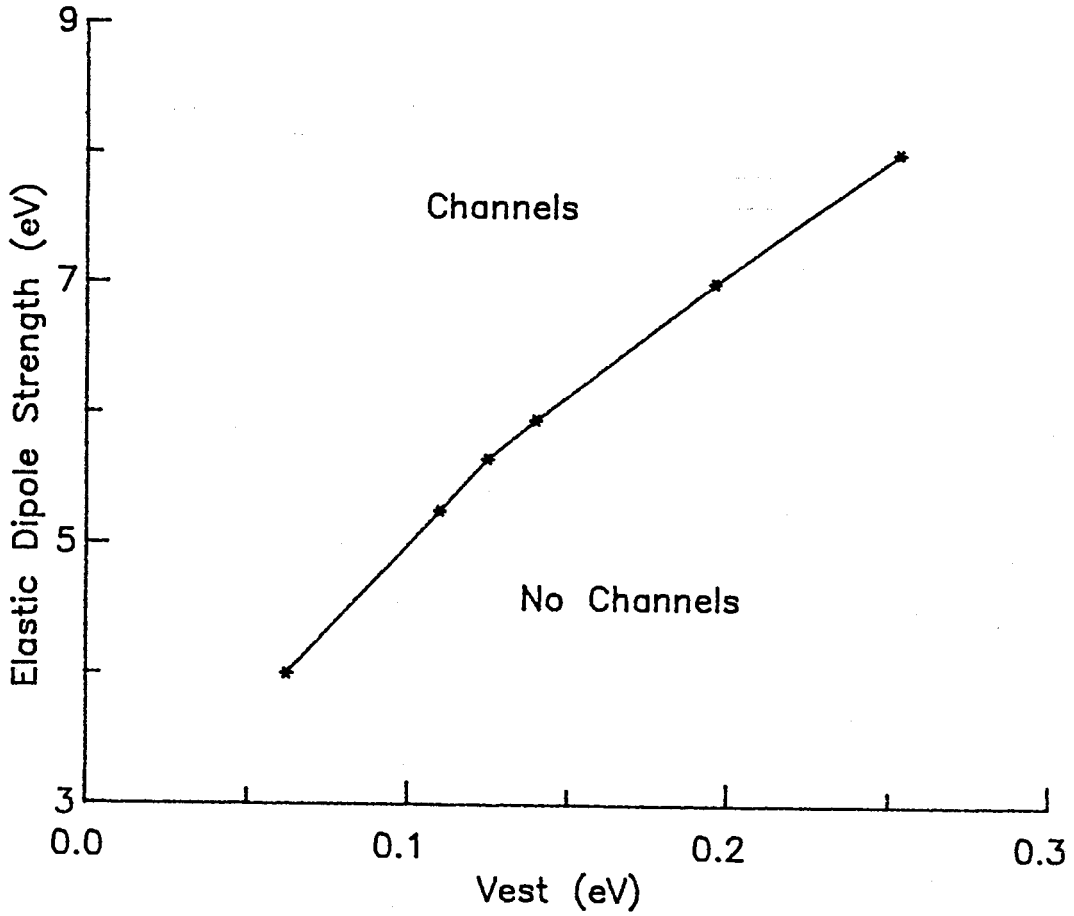
9
7
5
3
Elastic Dipole Strength (eV)
Channels
No Channels
0.0
0.1
0.2
0.3
Vest (eV)

Fig. 6.9

Fig. 6.10 Channel dependence on temperature. Each column represents the galleries of a crystal intercalated at different temperatures. The time for each simulation was 30 MMCS. Only 3 of the 6 galleries are shown. Parameter set: $C_{33}=55\times10^9$ N/m^2, $C_{44}=18\times10^9$ N/m^2, P=5.25 eV, $V_{est}(a,0)=0.095$ eV, out of plane interaction is 0.045 eV, $\mu=0$, $E_{rs}=0.025$ eV. The temperature is 293, 325, 425, 550, 650, 700, 725 K for columns a-g respectively. Lattice size: $N_x=40$, $N_y=120$, $N_z=6$.

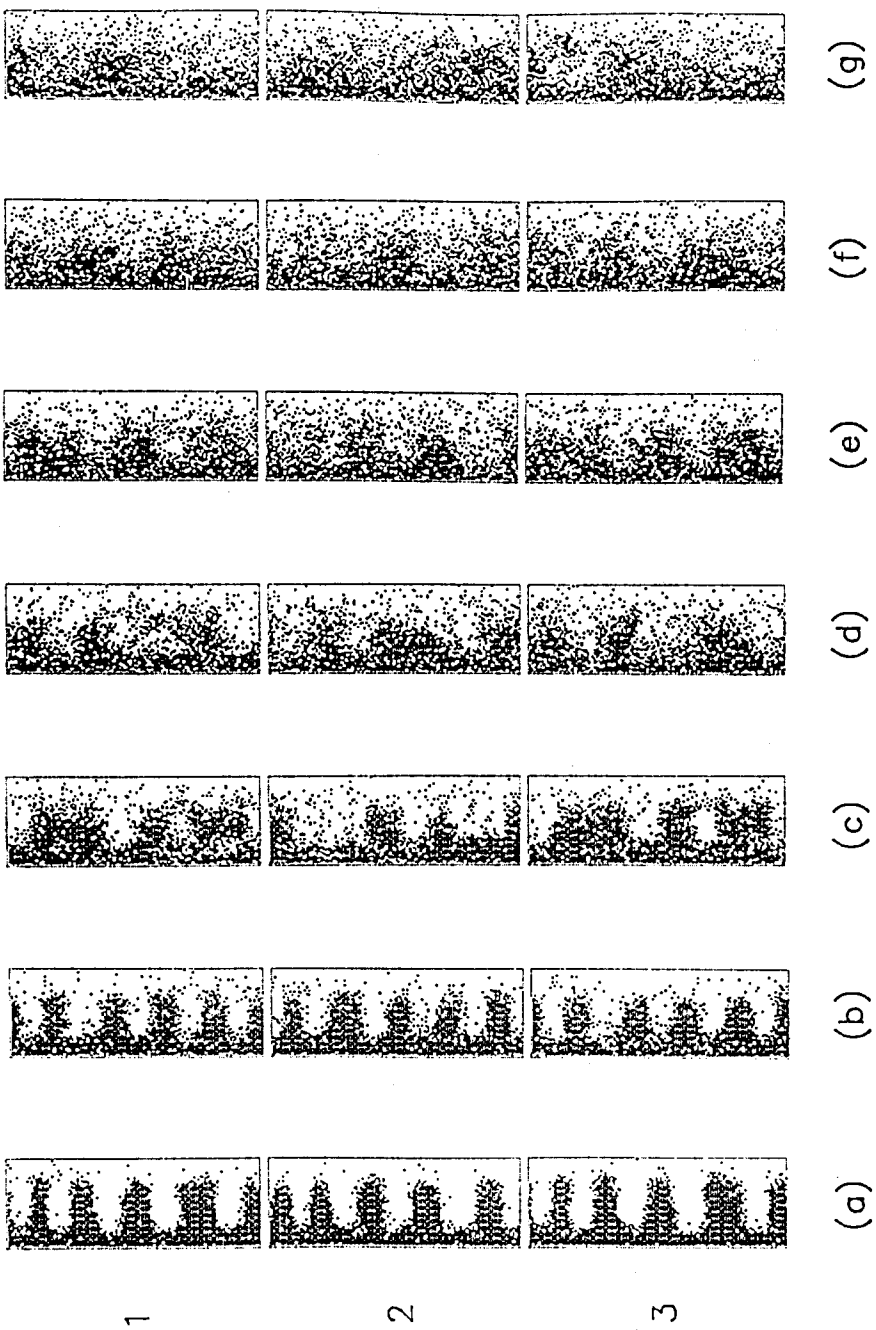

Fig. 6.10

Fig. 6.11 A plot of the intercalant concentration in the crystal as a function of the temperature. The data was obtained from the simulations shown in Fig. 6.10. A sharp transition associated with the disappearance of channels, as for Fig. 6.8, is not evident. No statistical error analysis was performed.

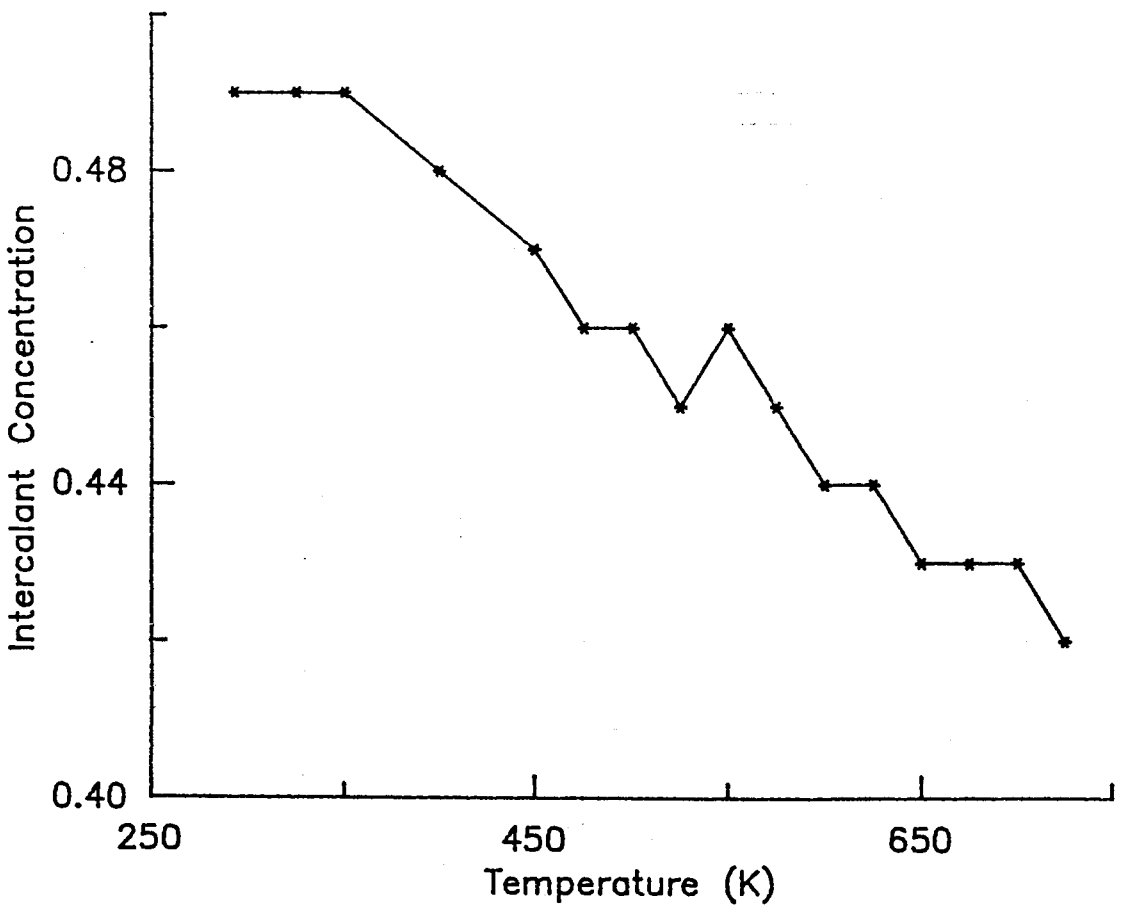
Intercalant Concentration
0.48
0.44
0.40
250
450
650
Temperature (K)

Fig. 6.11

Fig. 6.12 Channel dependence on the interlayer interactions. Each column represents the galleries of a crystal intercalated with different interlayer repulsion energies. The time for each simulation was 30 MMCS. Only 3 of the 6 galleries are shown. Parameter set: C_{33}=55x10^9 N/m^2, C_{44}=18x10^9 N/m^2, P=5.25 eV, $V_{est}(a,0)$=0.095 eV, T=293 K, μ=0, E_{rs}=0.025 eV. The interlayer interaction energies are 0.045, 0.035, 0.025, 0.015, 0.005, and 0.0 eV for columns a-f respectively.
Lattice size: N_x=40, N_y=120, N_z=6.

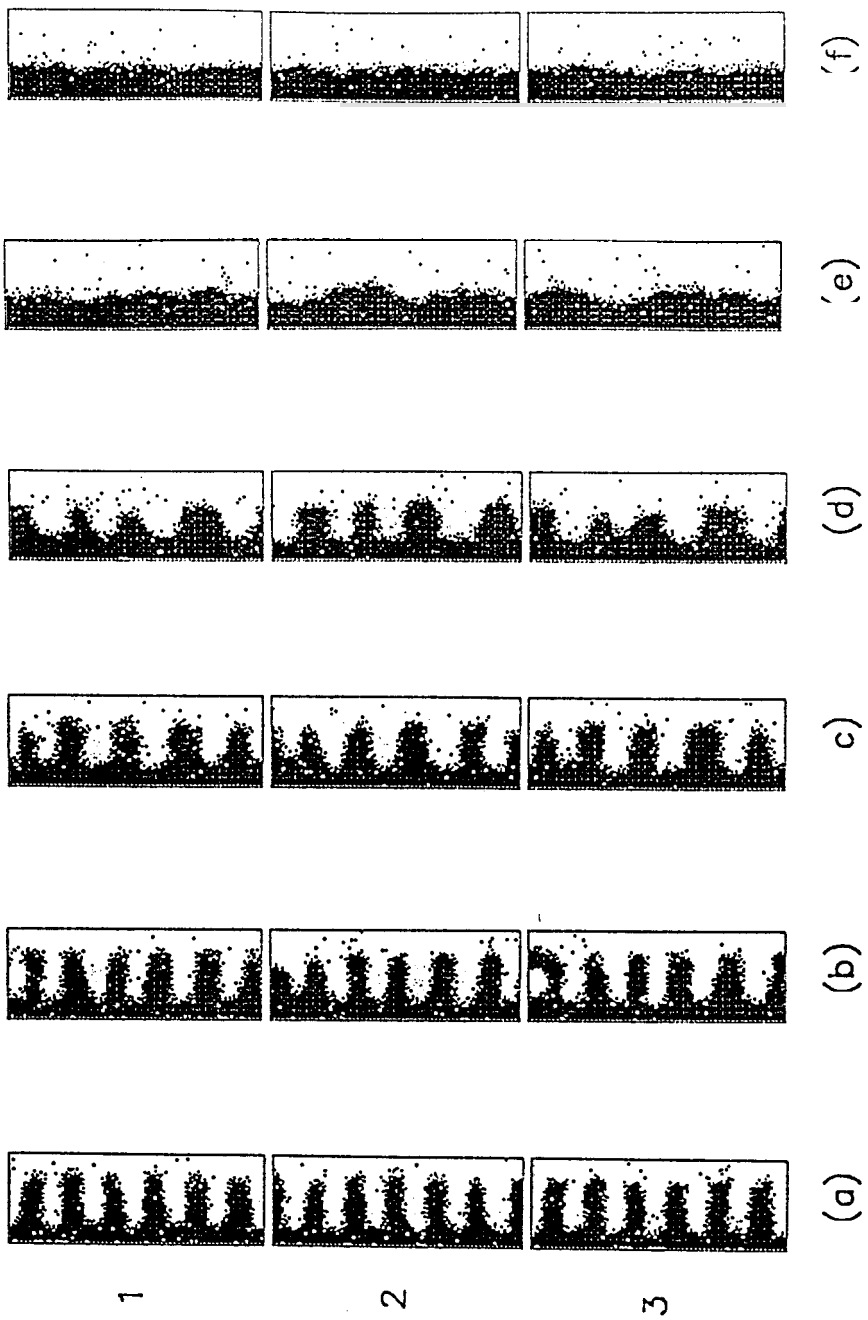

Fig. 6.12

Fig. 6.13 Channel dependence on the chemical potential of the reservoir. Each column represents the galleries of a crystal intercalated with a different chemical potential. The time for each simulation was 20 MMCS, except for column (a) which was 22.5 MMCS. Only 3 of the 4 galleries are shown.
Parameter set: C_{33}=55x10^9 N/m^2, C_{44}=18x10^9 N/m^2, P=5.25 eV, $V_{est}(a,0)$=0.095 eV, T=293 K, E_{rs}=0.025 eV, and the interlayer interaction energy is 0.045. The chemical potentials are μ=-0.025, -0.04, -0.07, -0.10 eV for columns a-d respectively.
Lattice size: N_x=40, N_y=120, N_z=4.

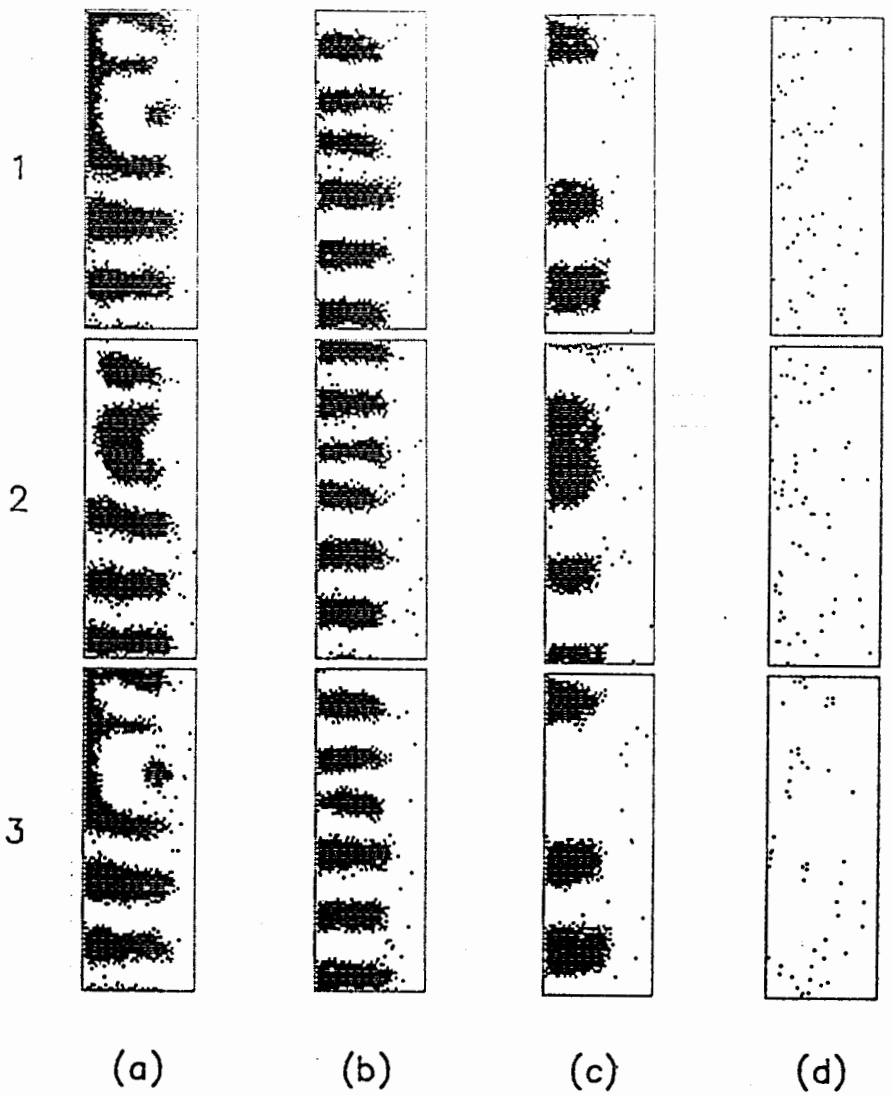

Fig. 6.13

Fig. 6.14 Channel formation during deintercalation. Stage-2 channels again form. Each column shows the galleries at different times. Columns a-d represent 7.5, 15, 22.5, and 30 MMCS respectively. Initially the crystal was completely filled. Only three of the four galleries are shown.
Parameter set: C_{33}=55x10^9 N/m^2, C_{44}=18x10^9 N/m^2, P=5.25 eV, $V_{est}(a,0)$=0.095 eV, out of plane interaction is 0.045 eV, μ=-0.17 eV, T=293 K, E_{rs}=0.025 eV.
Lattice size: N_x=60, N_y=120, N_z=4.

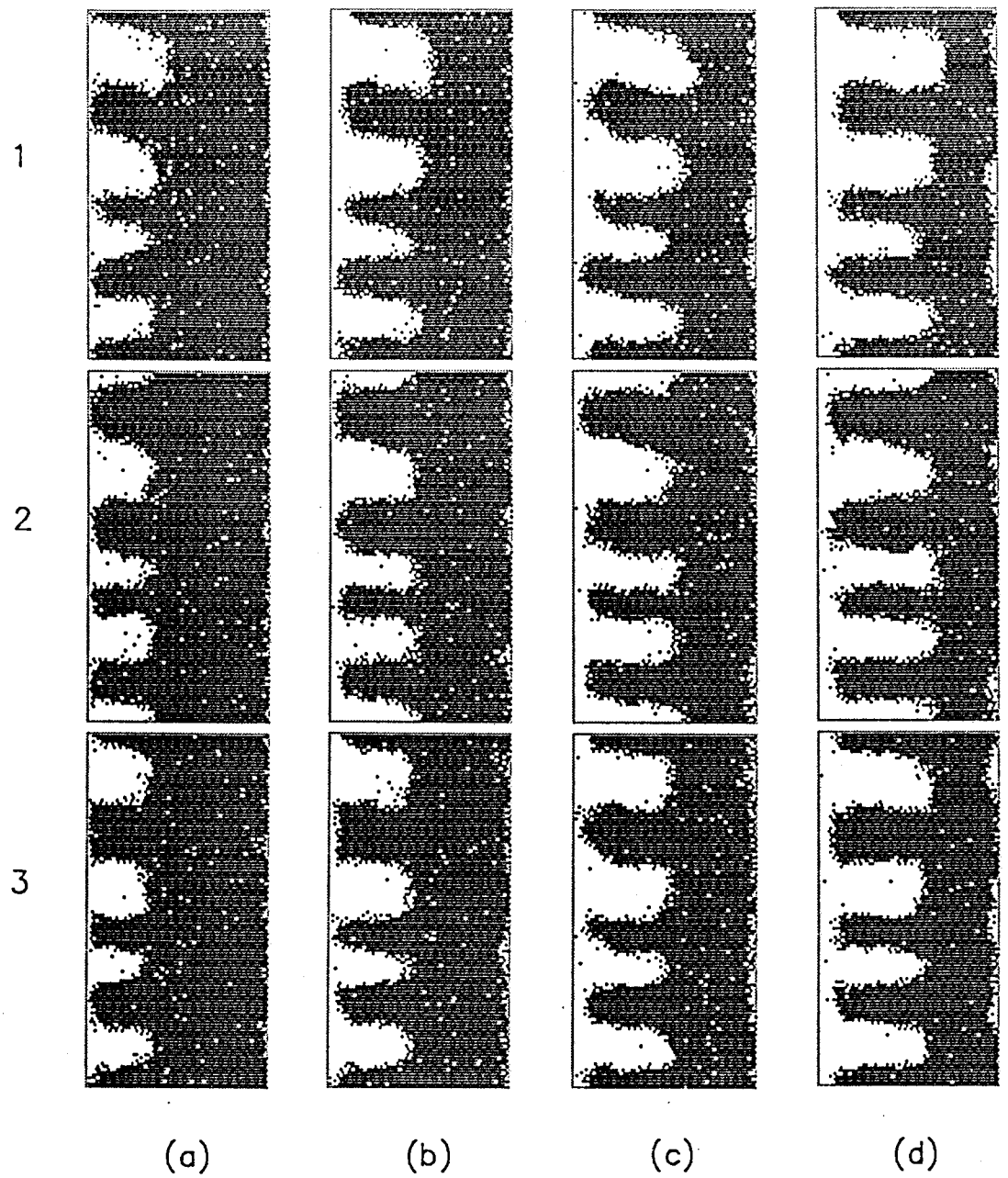

Fig. 6.14

Fig. 6.15 Low density channels showing x=1/3 and x=2/3 superlattices. The intercalant distribution in the crystal is shown at 36 MMCS. All four galleries are shown. With the parameter set chosen, the occupied regions consist of x=1/3 and x=2/3 superlattices.

Parameter set: C_{33}=55x10^9 N/m^2, C_{44}=18x10^9 N/m^2, P=8 eV, $V_{est}(a,0)$=0.3 eV, V_{o1}=0.025 eV, V_{o2}=0.008 eV (see text), μ=0 eV, T=293 K, E_{rs}=-0.025 eV.

Lattice size: N_x=60, N_y=120, N_z=4.

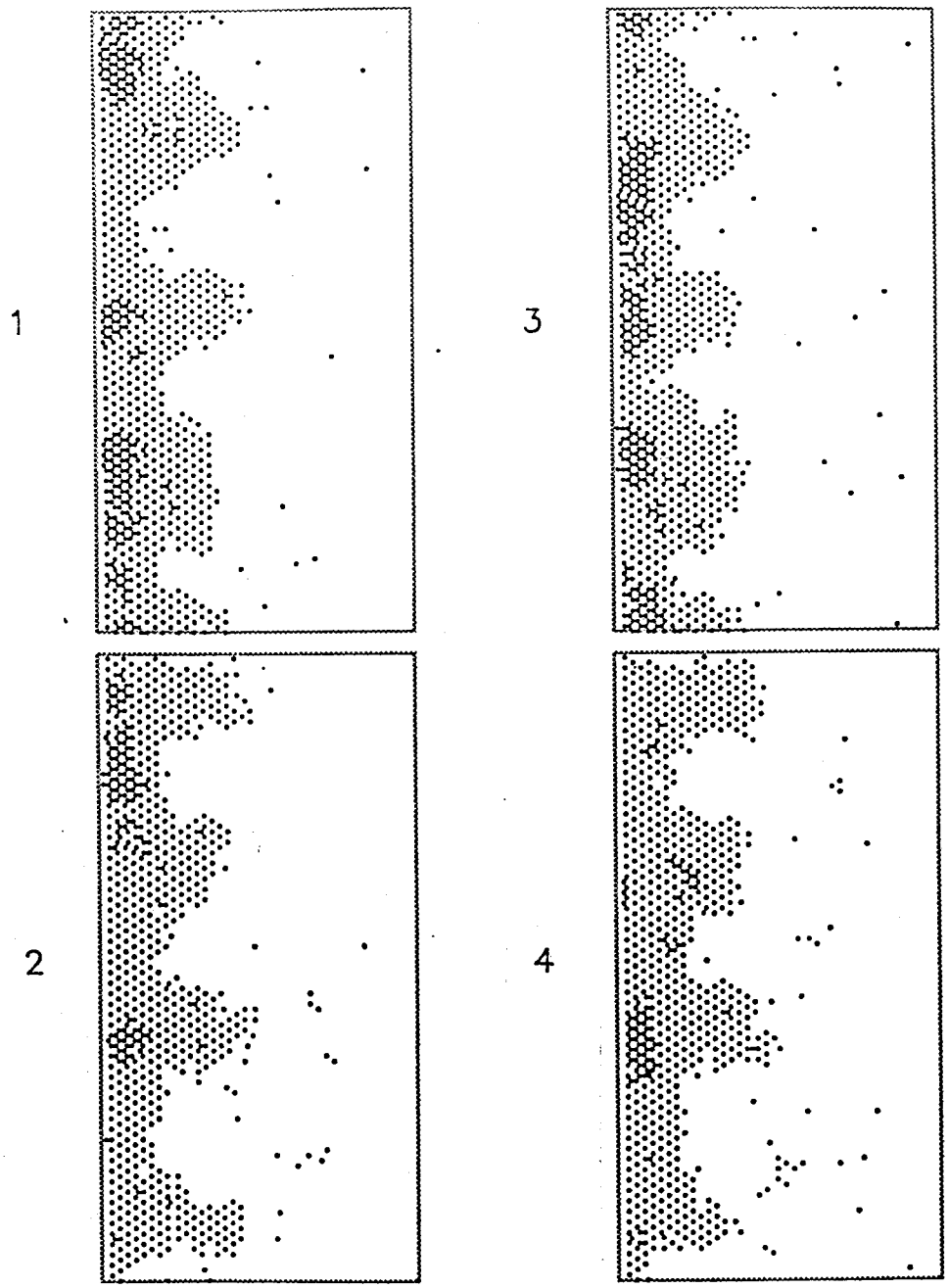

Fig. 6.15

Fig. 6.16 The evolution of channels for long intercalation times showing channel merging. Note that the far edge ($x=N_x$) is clamped . Each column a-j shows the crystal after 20, 40, 60, 80, 100, 120, 140, 160, 180, and 200 MMCS respectively. The initial 6 channels per gallery reduces to effectively 3.
Parameter set: $C_{33}=55\times10^9$ N/m^2, $C_{44}=18\times10^9$ N/m^2, P=5.25 eV, $V_{est}(a,0)=0.095$ eV, out of plane interaction is 0.045 eV, $\mu=0$ eV, T=293 K, $E_{rs}=0.025$ eV.
Lattice size: $N_x=100$, $N_y=120$, $N_z=4$.

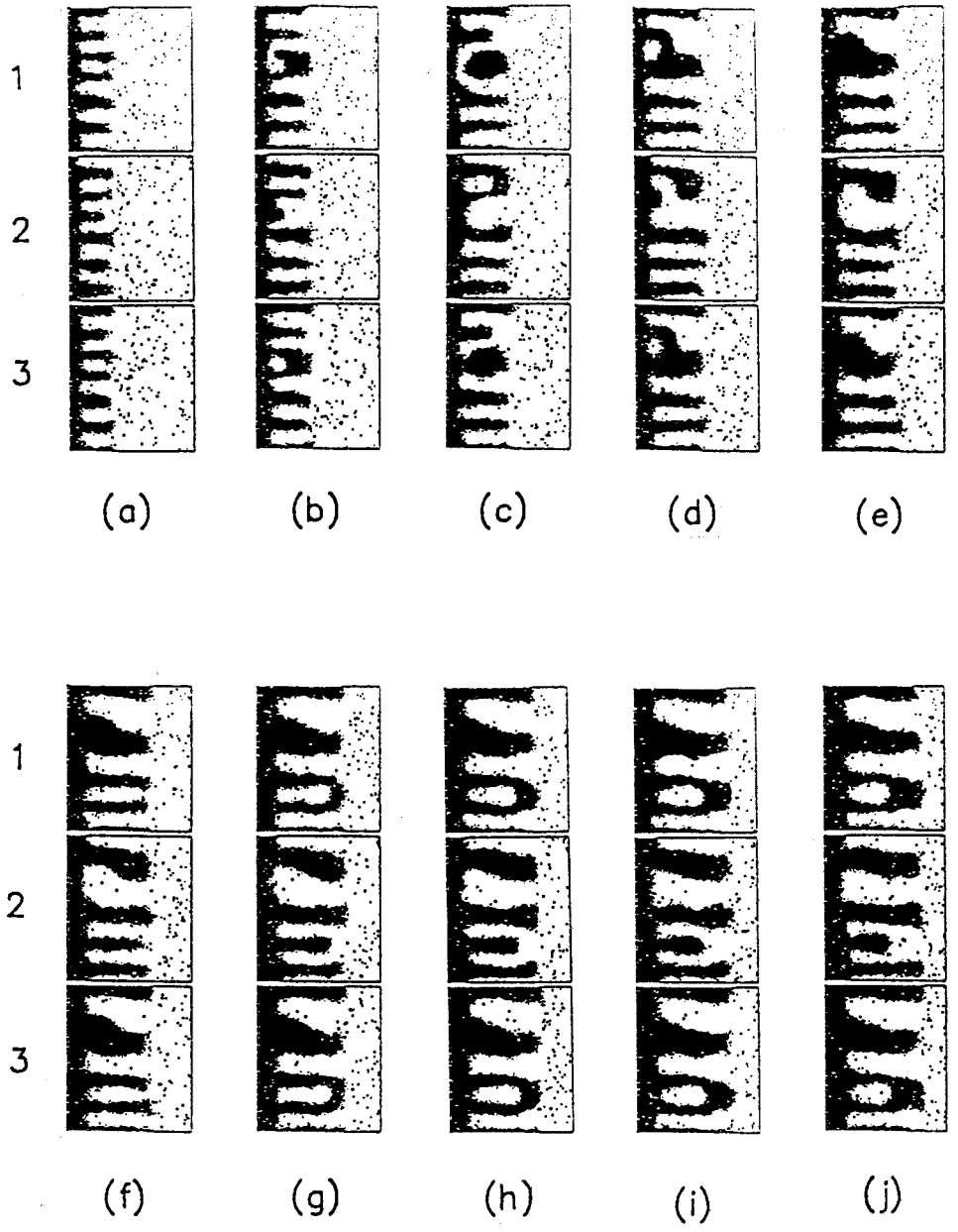

Fig. 6.16

CHAPTER 7

DISCUSSION

7.1 THREE-DIMENSIONAL CHANNEL DOMAIN MODEL

Prior to combining all of the experimental results presented in Chapters 4 and 5, it is worthwhile to summarize the most important results:

(i) Auger maps show that the Ag distributions on cleaved surfaces of stage-2 intercalated crystals are in the form of "channels". These channels extend from the crystal edge to the intercalation front, they are about 5 μm wide and have a periodicity of about 10 μm.

(ii) The elemental Auger intensities from line scan data support the assumption that, upon cleaving the intercalated crystal, the Ag in the cleaved gallery divides equally on an atomic scale.

(iii) Channels exist near crystal edges, but not in corners where two adjacent, simultaneously intercalated edges meet.

(iv) If a cleavage step occurs in a direction perpendicular to the channel direction, the positions of the channels reverse across the cleavage step. This is precisely what the domain model predicts if the cleavage step height corresponds to an odd number of TiS_2 layers.

(v) Upon cleaving, the channels on both of the newly created surfaces are mirror images. This, again, agrees with the assumption that the Ag divides equally on an atomic

scale upon cleaving.

The above results not only include the measured Ag distributions, but also the interpretation of possible cleaving effects.

From these results, a proposed 3-dimensional domain model for stage-2 Ag intercalated TiS_2 is shown in Fig. 7.1. This so-called "channel domain model" is supported by all of the above mentioned results. While none of the results, taken alone, provide enough evidence for the existence of domains and the actual domain structure, taken as a whole the interpretation of the results is believed to be very sound.

Fig. 7.1 may be considered a very simple and appealing picture of domain structure; the channels form near the crystal edge very early in the intercalation process and simply extend farther into the crystal as more intercalant is added into the galleries via the crystal edge. More details of this process will be considered in Section 7.5, where the simulation results of Chapter 6 will be discussed.

It must be stressed that this domain model, at present, is only applicable to partially intercalated, stage-2 Ag/TiS_2 prepared by the electrochemical cell techniques described in Chapter 3. This is due, at least in part, to the fact that the size and shape of intercalation domains are <u>not</u> an equilibrium phenomenon, but depend on sample history (such as sample preparation techniques). For example, thermally grown stage-2 powders would not be expected to exhibit a channel structure due to the lack of a preferred direction during formation, a condition which is very important for channel formation (see Chapter 6).

The observed 5 μm width of the domain structure is very different

from the 100 to 200 Å island size reported previously by Kaluarachchi and Frindt (27) in stage-2, partially intercalated Ag/TiS_2. As was stated in Section 1.5, this size was based on a moving island model applied to sloping intercalation fronts. It must be pointed out, however, that their method of determining this island size was indirect. (In fact, they assumed that islands existed and were in the form of narrow stripes that were parallel to the intercalated crystal edge - precisely the opposite to what was observed in this thesis research). The sloping intercalation fronts they observed could very well be due to long-range strains in the crystal, rather than moving islands of intercalant.

7.2 SURFACE EFFECTS AND CLEAVAGE STEP MODELS

All of the work in this research project was done using surface techniques. Since the objective was to infer the domain structure, a bulk property of intercalation, a problem arises: can a surface technique measure a bulk property? While great care was taken to interpret the results in an "unbiased fashion", one can still be fooled. Could the surface distributions represent a surface effect, rather than the bulk domain structure? To answer this question, the cleaving process must be considered further.

Two newly created surfaces that occur upon cleaving only "remember" two configurations:

(i) the bulk structure that existed prior to cleaving, and

(ii) cleavage steps or other crystal defects.

These configurations only exist immediately after cleaving. Any time after cleaving, the newly exposed surfaces can react to their new environment.

The channel domain model shown in Fig. 7.1 ignores the possibility of cleavage steps and subsequent surface intercalant diffusion, and assumes the results obtained are merely due to the bulk domain structure that existed prior to cleaving. One must not be naive. Thus, in the following discussion, attempts will be made to interpret all of the results in terms of a cleavage step model which also includes surface diffusion. Simultaneously, the results will be interpreted by the channel domain model (in order to contrast and compare the two models). An initially "simple" cleavage step model will be introduced in Section 7.2.1, but it will be constantly refined in subsequent sections in order to agree with the experimentally observed properties of channels.

When describing the cleavage step model, it will be assumed that staging and intercalation domains exist, but not in the form of channels and not on a scale of 10 μm.

7.2.1 Channels for a Cleavage Step Model

The appearance of channels via Auger and optical analysis can be explained in terms of a cleavage step model. This model will be where, upon cleaving, cleavage steps result which are perpendicular to the intercalated crystal edge and regularly spaced at 10 μm intervals. Then after cleaving, surface Ag diffuses to, and resides, near these surface steps. Other Ag motion near the surface which might occur are the deintercalation of bulk Ag via the surface steps, or the intercalation of surface Ag via the surface steps. This diffusion/deintercalation/intercalation must occur within an hour or two after cleaving since channels are observed with Auger analysis within this

time period. The final result could be the appearance of stripes of Ag extending from the crystal edge to the intercalation front.

While this cleavage step model does provide an explanation for the appearance of channels, there exists the unlikely fact that the cleavage steps are always perpendicular to the crystal edge and spaced 10 μm apart. In addition, the Ag must reside near the steps and in regions that are about 5 μm wide.

The channel domain model simply predicts that these Ag rich regions on the cleaved surface are due to the bulk domain structure that existed prior to cleaving.

7.2.2 Relative Auger Intensities for a Cleavage Step Model

The intensity ratio, R, of the maximum Ag Auger signal to the minimum Ag Auger signal obtained from Ag Auger line scans can be calculated theoretically from the intensity equation represented by equation 4.1. In terms of a channel domain model, the intensity ratio for the Ag signals calculated from Eq. 4.1 agrees with the experimentally obtained value if it is assumed that the Ag divides equally on an atomic scale upon cleaving. Under this assumption, the local concentration of Ag on the surface is approximately 0.2 of a monolayer. It is believed that this assumption is realistic since the cleaving process is quite symmetric.

For a cleavage step model, no such simple assumption can explain the observed ratio. Consider surface Ag that resides near the surface cleavage steps. This Ag has an average concentration of x_s of a monolayer. The value of x_s required to give the observed intensity ratio R=1.7 depends on the subsurface distribution of Ag. Two simple cases to consider are that

either the actual domain size is much smaller than the 10 μm cleavage step spacing (Fig. 7.2(a)), or the actual domain size is much larger than the 10 μm cleavage step spacing (Fig.7.2(b)). For the case where the domain size is smaller, the calculated value of x_s to give R=1.7 is about 0.08. When the domain size is much larger, the value of x_s needs to be about 0.04. These values of x_s are rather low if it is assumed that the Ag divides equally upon cleaving to give x_s=0.2 - a reasonable assumption. In order for the local surface intercalant to have such a low value, the surface Ag must be "going somewhere". Since Ag is not volatile and so would be expected to remain on the crystal surface, the most reasonable explanation seems to be that the surface Ag concentration is decreasing via the intercalation of the surface Ag through the cleavage steps. However, this intercalation is in contrast with the spontaneous deintercalation observed (Chapter 5).

7.2.3 Absence of Channels in Corner Regions and a Cleavage Step Model

The absence of channels in corner regions (where two intercalated edges meet) is easily explained in terms of a channel domain model: during the intercalation process the channels extending in from the two adjacent edges "run into" each other and destroy the channel-like structure.

For a cleavage step model, there seems to be no explanation except for the possibility that regular cleavage steps do not occur in these corner regions. Why not?

7.2.4 Channel Reversal Across a Cleavage Step Perpendicular to the Channel Direction

Channel reversal across a cleavage step perpendicular to the channel direction (Fig. 5.3) has a simple interpretation in terms of a channel domain model: the cleavage step corresponds to an odd number of TiS_2 layers so that the domain model predicts that the intercalant distribution on one side of the step is anti-correlated to the distribution on the other side of the step.

The explanation of the channel reversal in terms of a cleavage step model is complicated. Firstly, if the 5 μm wide channel regions are formed by cleavage steps perpendicular to the crystal edge, then it seems reasonable that 5 μm wide regions should also be formed by cleavage steps parallel to the crystal edge. From Fig 5.3, the cleavage step parallel to the crystal edge appears very different (narrower) than the apparent cleavage steps perpendicular to the crystal edge. Secondly, why do the cleavage steps perpendicular to the crystal edge shift by 5 μm across a cleavage step parallel to the crystal edge? Two possible answers to this are:

(i) <u>During</u> the cleaving process, cleavage steps perpendicular to the edge are being created. If a cleavage step parallel to the crystal edge is then created, the steps perpendicular to the edge terminate, and new steps (also perpendicular to the edge) begin. These new steps are displaced laterally with respect to the old ones by exactly 5 μm. The resulting appearance of cleavage steps is shown in Fig. 7.3 (a).

(ii) The cleaving process creates cleavage steps which are both parallel and perpendicular to the crystal edge as shown in Fig. 7.3 (b). Then

for some reason, after cleaving the two portions of the crystal on either side of the cleavage step parallel to the crystal edge shift 5 μm laterally with respect to each other.

Both of these possibilities seem rather far-fetched. However, case (ii) may seem to be more likely. It is assumed that subsequent Ag surface diffusion, as explained in Section 7.2.1, would cause the decoration of the cleavage steps to appear as channels.

7.2.5 The Appearance of Channels at the Same Location on Both of the Newly Created Surfaces

The effect of the channels in the cleaved gallery appearing at the same location on both of the newly created surfaces has a simple explanation in terms of the channel domain model. Since the results of Auger intensities indicate that the Ag in the cleaved gallery splits equally on an atomic scale upon cleaving, then it is obvious that domains in the cleaved gallery would split equally and occur at the same location on both surfaces.

This effect explained in terms of a cleavage step model becomes very tricky and includes, surprisingly, only one possibility. It turns out, in fact, that diffusion of surface intercalant cannot occur in order for this effect to be explained by a cleavage step model.

First, assume that the "actual" domain size is much smaller than 5 μm. Then on a scale of 5 μm every gallery would appear to be the same, that is, uniformly filled with intercalant. The cleaving process then creates a series of steps perpendicular to the crystal edge and spaced 10 μm apart (Fig. 7.4(a)). In order to obtain 5 μm wide occupied regions

separated by 5 μm wide unoccupied regions, the surface Ag diffuses away from the surface step on its own level (Fig. 7.4(b)). If this occurs on both surfaces, the observed distribution would have opposite Ag occupation on the two surfaces (which is contrary to what is experimentally observed). This picture only occurs, however, if all of the cleavage steps are in a regular staircase fashion as shown in Fig. 7.4(a). If the cleavage steps do not form a regular staircase (Fig. 7.4(c)), then the situation becomes confused. Some of the surface Ag does not "know" which cleavage step to diffuse toward, and some Ag would have no cleavage step to diffuse toward. In this case, a regular pattern of surface Ag would not exist. So it seems that a domain size of much less than 5 μm cannot explain the observed results in terms of a cleavage step plus diffusion model.

Second, assume that the "actual" domain size is much larger than 5 μm so that on a scale of 5 μm the system would appear to exhibit classical staging. Then again, as above, the cleavage steps must occur in a regular staircase fashion in the c-axis direction. However - to give channels, as will be explained below, the regularity depends on whether or not surface diffusion of intercalant occurs. If surface diffusion does not occur then the cleavage steps must be 5 μm apart and each cleavage step must correspond to an odd number of TiS_2 layers. This is shown in Fig. 7.5. Note that for this model to work, the intercalant in the cleaved galleries must divide equally on an atomic scale, leaving a surface intercalant concentration of 0.2 of a monolayer. Recall, however, that in order to obtain the correct Auger intensities, the surface intercalant concentration must be about 0.04 of a monolayer (see Section 7.2.2). This requires the surface intercalant to leave the crystal surface by either leaving the

crystal entirely or by intercalating via the surface steps. If surface diffusion does occur, then the same problem arises as in the case where the actual domain size is assumed to be much smaller than 5 μm; that is, the intercalant on the two surfaces are in the opposite configurations, not the same configurations.

From these possibilities, the only one which correctly describes the results is the case where the domain size is much larger than 5 μm, the cleavage steps are 5 μm apart, and each cleavage step corresponds to height equal to an odd number of TiS_2 layers.

7.3 CHANNEL DOMAIN MODEL VERSUS CLEAVAGE STEP MODEL

Section 7.2 addressed the possibility that the observed surface intercalant distribution was due to cleavage steps rather than to the bulk domain structure. It is worthwhile to summarize the two models and how they explain the observed results.

The channel domain model states that the bulk domain structure is in the form of 5 μm wide intercalate domains which extend from the crystal edge to the intercalation front. Upon cleaving the intercalated crystal, the intercalant in the cleaved gallery divides equally on an atomic scale onto both of the newly created surfaces. The relative Auger intensities from Auger line scan data support this "cleaving assumption". No channels are observed in corner regions where two intercalated edges of the crystal meet since the channels within each gallery interfere with each other during the intercalation process and destroy the channel-like structure. When a cleavage step of a height corresponding to an odd number of TiS_2

layers occurs, which is perpendicular to the channel direction, a channel reversal exists across the step. Such an occurrence is predicted by the topology of a stage-2 channel domain model. Upon cleaving, the channel location on both of the newly created surfaces is the same, as predicted by the cleaving assumption.

The cleavage step model states that the intercalant distribution needs to be more of a classical stage-2 system, or at least a domain system with the size of the domains being large compare with 5 μm. The cleaving process creates cleavage steps which are perpendicular to the intercalated crystal edge. These cleavage steps are regularly spaced at 5 μm and each cleavage step height corresponds to an odd number of TiS_2 layers. No such cleavage steps are present in corner regions where two intercalated edges meet. If these cleavage steps encounter a cleavage step which is parallel to the crystal edge, then the former shift laterally by exactly 5 μm.

While the channel domain model is quite simple, the cleavage step model is rather complex and unlikely, particularly becasue regular cleavage steps must occur at intervals of 5 μm and consistently be of heights corresponding to an odd number of TiS_2 host layers.

It is believed that the above discussion strongly supports the channel domain model and makes the cleavage step model most unlikely.

7.4 WHY CHANNELS ARE NOT OBSERVED IN EVERY SAMPLE

As was pointed out is Section 4.3.5, not all samples revealed the existence of channels. Of all the samples analyzed, only about 10 or 15

percent showed the existence of channel-like structure. The remainder of the samples revealed no intercalant structure whatsoever - only constant elemental distributions on the sample surface. This section addresses the problem of why channels are observed on only a small proportion of the samples tested.

The first question to pose is: In the intercalated systems prepared, are channels present in all stage-2 regions of the crystals prior to cleaving? When answering this question, regions of crystals where two adjacent, simultaneously intercalated edges meet will not be considered since these corner regions are not expected to contain channels, as described previously in Section 7.2.3. The answer to this question for ideal crystals and ideal intercalating conditions would probably be yes (assuming that channels do indeed exist) , but the crystals used and the sample preparation conditions were not "perfect". Real crystals contain defects within the intercalating galleries. These defects could alter the domain structure into some topology other than channels. In addition, during the sample preparation procedure, the crystals were in contact with tape gum, various chemicals, and silicone sealant. These contaminants could remain on portions of the crystal during sample preparation. In particular, contamination or damage at the edges of the crystal could effectively inhibit the intercalant from entering some galleries. In addition, the intercalated crystal could then contain some stage-2 regions intermixed with unintercalated regions, as shown in Figure 7.6. At the boundary between these two types of regions there would probably not be any type of staging, as shown in the figure, since it is known that galleries

near the surface of a crystal intercalate faster and do not exhibit simple staging (56). From experience it is known that unintercalated crystals cleave easier than intercalated crystals so one can expect that the hypothetical crystal shown in Fig. 7.6 to cleave at the position of an unintercalated gallery. If this were the case, Auger analysis would yield a constant Ag distribution and a surface decoration pattern would not be expected.

The above argument relates the absence of channels to the fact that channels might not exist in all regions of the stage-2 crystal. But what if channels do exist in the cleaved gallery? What could be responsible for the absence of channels that do exist prior to cleaving? Section 7.2 stated that the newly created surfaces that occur upon cleaving remember only two configurations: the bulk configuration that existed prior to cleaving and cleavage steps. Diffusion can occur subsequently. If channels exist, and are not revealed by surface analysis, then cleavage steps and/or diffusion must be responsible for their absence. Cleavage steps on a scale much smaller than 10 μm could mask the channel structure, leaving only a constant intercalate distribution (on the scale of 10 μm). Such cleavage steps have been seen for TiS_2 as determined from Scanning Tunneling Microscopy (57).

With all this talk of cleavage steps and unintercalated galleries, there still exists a very simple possibility for the absence of channels; they do not exist in all stage-2 crystals. Instead, some crystals may either exhibit classical staging, or a domain size much smaller than 5 μm. In either case, surface analysis on a scale of 5 μm would reveal constant

intercalate distributions.

7.5 COMPUTER SIMULATIONS, CHANNEL FORMATION AND THE 10 μm LENGTHSCALE

7.5.1 Introduction

The channel domain model for stage-2, Ag intercalated TiS_2, shown previously in Fig. 7.1 shows the intercalate distribution once intercalation (or deintercalation) and subsequent stage conversion are complete. But a number of obvious questions still remain.

(1) Under what conditions do channels form or not form?

(2) How do the channels form?

(3) What determines, and can possibly alter, the 10 μm lengthscale of the channels?

These questions were attempted to be answered via the Monte Carlo computer simulations, whose results were shown in Chapter 6.

It is important to state here that the discussions that follow deal mainly with the properties of the so-called "high-density" channels - where, within a channel, all sites are filled. Even though the "low density" channels have properties which are closer to the experimentally observed channels (i.e the density and superlattice ordering), most of the simulations were done with parameter sets for high density channels. The reason for this is that the high density channels were observed first, and once observed, many simulations were done to study their properties. Only after that were low density channels sought (Fig. 6.15). Future work will most likely involve more low density channel simulations.

To answer the first question from these simulation results - the

simulations show that channels form under a variety of conditions. Many different parameter sets revealed intercalation channels. If channels did form under a given set of conditions (see Fig. 6.7, for example), then the simulations indicate that channels will not form if the following parameters are altered sufficiently as follows:

(a) the temperature is increased,

(b) the interlayer repulsion is reduced,

(c) the intralayer attraction is decreased,

(d) the intralayer electrostatic repulsion is increased,

(e) the reservoir chemical potential is decreased.

Point (a) is due to the increasing entropy effects with temperature. The channels seemed to disappear gradually with temperature (see Fig. 6.10).

Point (b) is a result of two dimensional diffusion not resulting in finger formation unless a driving field exists (55), no such field existed in our simulations. The channels appeared to disappear gradually as the interlayer interactions were reduced (see Fig. 6.12).

Points (c) and (d) are basically equivalent and are due to islands of intercalant being energetically unfavorable. The channels seemed to disappear abruptly with small changes in the intralayer interactions (see Fig. 6.7).

Point (e) is a result of the intercalant atoms entering the crystal too slowly. This causes the atoms that enter the crystal to have time to diffuse away from the reservoir before other atoms

enter the crystal. This condition inhibits the formation of intercalant islands (see Fig. 6.13).

The answer to the second question (how the channels form) is provided quite simply by the results of simulations which show the distributions early in the intercalation process. This was shown in Fig. 6.4 (the following short discussion assumes that parameter values are such that channel formation does occur). Early in the simulation the intercalant atoms enter the crystal more or less randomly. Then, due to the long range intralayer attraction, atoms preferentially enter the crystal in the neighborhood of already intercalated atoms. This results in the formation of islands of atoms near the intercalating crystal edge. The islands tend to be staggered along the c-axis direction due to the interlayer repulsion between the atoms. The staggering of islands permits movement of the atoms in the direction perpendicular to the intercalating crystal edge, but inhibits movement parallel to the intercalating crystal edge. Therefore, the atoms move farther into the crystal and the depleted regions near the intercalating crystal edge are replenished via the reservoir. The end result is islands of intercalant that are elongated in the intercalation direction and staggered along the c-axis - in other words, a stage-2 channel distribution.

The answer to the channel lengthscale question is more involved and is dealt with in the next Section.

7.5.2 The Channel Lengthscale

The simulations of Chapter 6 involved a set of parameters. These parameters were chosen to have values appropriate to those for intercalating atoms of Ag into TiS_2 - i.e. the intercalate that entered the crystal was assumed to be made up of individual atoms, rather than the elementary islands of intercalant of Kirczenow's work (24). Therefore, the distance scale of the allowed lattice sites in the simulations represents atomic distances. With this in mind, all of the channel lengthscales observed in the simulations were on the order of tens of angstroms, not the experimentally observed 10 microns. Naturally one would want to obtain a lengthscale close to the experimental value, but how does one obtain a lengthscale of microns when the simulated sample size is only a few hundred angstroms? Obviously this cannot be done unless the intercalating crystal edge in the simulations consisted of about 10,000 lattice points per gallery, and this is too large a "crystal" to be handled in a simulation.

The method that will be used here to obtain micron-sized lengthscales will involve examining increasing lengthscale trends that were observed in simulations, and assume that these trends persist to ever increasing lengthscales. The definition of the lengthscale is the period of the channels.

Some immediate observations from the simulations is that the initial lengthscale depends on the input parameters. The general trends observed are:

(a) the lengthscale increases as the nearest neighbor intralayer

repulsion is increased (Fig. 6.7),

(b) the lengthscale increases with an increase in temperature (Fig. 6.10),

(c) the lengthscale increases with a decrease in the interlayer repulsion (Fig. 6.12),

(d) The lengthscale increases as the chemical potential of the reservoir is decreased (Fig. 6.13),

(e) The lengthscale increases with the time of the intercalation simulation (Figs. 6.16).

Points a-d present a problem when attempting to obtain a 10 μm lengthscale. Take point (c) for example and refer to Fig. 6.7. From this figure, the lengthscale increased with a decreasing interlayer repulsion (V_{out}) approximately as follows:

V_{out} (eV)	lengthscale (μm)
0.045	0.006
0.035	0.006
0.025	0.007
0.015	0.009
0.005	0.018
0.000	∞ (?)

The lengthscale for V_{out}=0 is not neccessarily infinite, but definitely greater than 0.036 μm (the size of the lattice). As can be seen, the lengthscale increases very rapidly, so a very small change in V_{out} (near V_{out}=0) provides a very large increase in the lengthscale. This provides an "uncomfortably narrow" parameter range in which a 10 μm

lengthscale would exist, and would require an extremely small, and unrealistic, interlayer repulsion.

This type of rapid increase is common to lengthscale increases for points a-d mentioned above, and therefore, these are not believed to be realistic mechanisms for increasing the lengthscale.

One remaining mechanism for increasing the lengthscale is point e above: the lengthscale increases with the intercalation time. From Fig. 6.16, the lengthscale increased by a considerable amount as the intercalation time increased. If this process continued, then a 10 μm lengthscale would result at some time. Recall that for this particular simulation, the $x=N_x$ edge was clamped rather than free. This was due to the observation that, with a free edge, a steady state could be reached. This steady state was caused by the large number of particles that would leave the crystal at this free edge. It is evident that a clamped edge enhances channel merging in that particles, which have previously broken away from the channels, have the opportunity to return to the intercalated region and create (or even enhance) a perturbation, the net result being channel merging. (A free edge does not favour this because too many particles leave the crystal before they can have the chance to return to create the perturbation). A clamped edge is actually quite realistic in that it mimics a finite crystal although in the simulations performed the crystal is very small. It is important to note that the <u>formation</u> of channels is not dependent on the edge being clamped, since channels readily formed with a free edge.

So channels merge and, possibly, at some time a lengthscale of 10 μm would be reached. At what time would this occur? This is a dangerous

question to attempt to answer considering the available data. For instance, it is quite possible that the merging times could depend on the crystal size. In any case, a possible direction would be to observe merging for long intercalation times and then plot the lengthscale versus time. Extrapolation of this curve could give the time when a 10 μm lengthscale would occur. This Monte Carlo time would then have to be related to real time via the intralayer diffusion constant, whose value is about 10^{-10} cm^2/s (20) - i.e. the attempt frequency of intralayer particle hopping is given by the diffusion constant divided by the square of the hopping distance (about 3.4 Å for TiS_2); and the reciprocal of the attempt frequency, whose value turns out to be about 10^{-5} s, is proportional to the Monte Carlo time. The proportionality constant is not known.

So why was 10 μm the only lengthscale observed in experiments? Because they were all intercalated for about the same time!

7.5.3 "Failures" of the Computer Simulations

The results of the Monte Carlo simulations of intercalation just described ignored one of the main failures of the simulations. This failure will be briefly discussed here.

With the simulation parameter set initially chosen for Ag_xTiS_2, channels formed in the very first simulation, but the local density of intercalant was too high (this simulation was shown in Fig. 6.4). Rather than obtaining x=0.4 for a local intercalant concentration, x=1 was observed. The parameters then had to be artificially altered to obtain channels with a lower density, combined with a $\sqrt{3}$ x $\sqrt{3}$ superlattice. The

reason for this failure could be due to (1) ignoring of the tetrahedral sites in the simulated crystal, and (2) the failure of the Safran-Hamman elastic model.

The tetrahedral sites in Ag/TiS_2 are empty, as the Ag prefers the octahedral sites. However, the tetraderal sites still provide sites for particle transport. In fact, the structure of TiS_2 is such that intercalant moving from octahedral site to octahedral site must pass through tetrahedral sites. This definitely alters the intercalation rate and therefore the intercalation kinetics and inevitably the channel properties.

The Safran Haman elastic model assumes particle-particle interactions in an elastic continuum. This ignores interference effects from other particles along with the discreteness of the lattice. Ignoring these effects is definitely an oversimplification.

However, given this failure, the results of the simulations were overall very interesting and informing. At the onset of the simulations, it was not known that channels would form at all with the intercalation model used. In fact they did, and many interesting properties of the channels were determined, both from a purely theoretical point of view (the observed transitions form channels to no channels) and from an experimentalist's point of view (possibly altering the 10 μm lengthscale).

One other late note - it was realized that the crystal edge used in the simulations (see Fig. 6.2) did not correspond to a real crystal edge in TiS_2. The real TiS_2 edge corresponds to the top row of sites in Fig. 6.2

rather than the left column of sites actually used in the simulations. Simulations recently done with this "proper" edge do not significantly differ from the results presented in Chapter 6, nor do they affect the disussion presented in this chapter.

7.6 SUGGESTIONS FOR FUTURE WORK

From an experimental viewpoint, there is very little that can be done to further establish the existence of channels in TiS_2. It would be interesting to alter the channel lengthscale as supplied by the computer simulations. Intercalating at different temperatures and for varying times would probably be a solid starting point for lengthscale manipulation. Theoretically, there is much work that can still be done. The computer simulations of intercalation shown in Chapter 6 examined channel properties in a relatively small portion of phase space. A more extensive study could certainly be performed, particularly in the area of lengthscales.

The spontaneously deintercalating crystals and the surface decoration of TiS_2 surfaces needs much more work in order to understand the processes which cause these phenomena. Attempting to control the spontaneous deintercalation by varying the sample temperature and the sample environment would prove useful.

In addition, the surface decoration pattern resulting from the intercalation through a pinhole did not seem to exhibit a reasonable stage-2 domain structure. Further work on staging in pinhole regions would prove useful in determining the amount of stage order (or disorder) in these regions.

Finally, since channels have been found in stage-2 Ag intercalated

TiS_2, it would be worthwhile to see if such structures exist in other materials.

Fig. 7.1 Three dimensional view of a stage-2 channel domain model. The dark regions represent channels which extend into the page toward the intercalation front. The host layers are not shown.

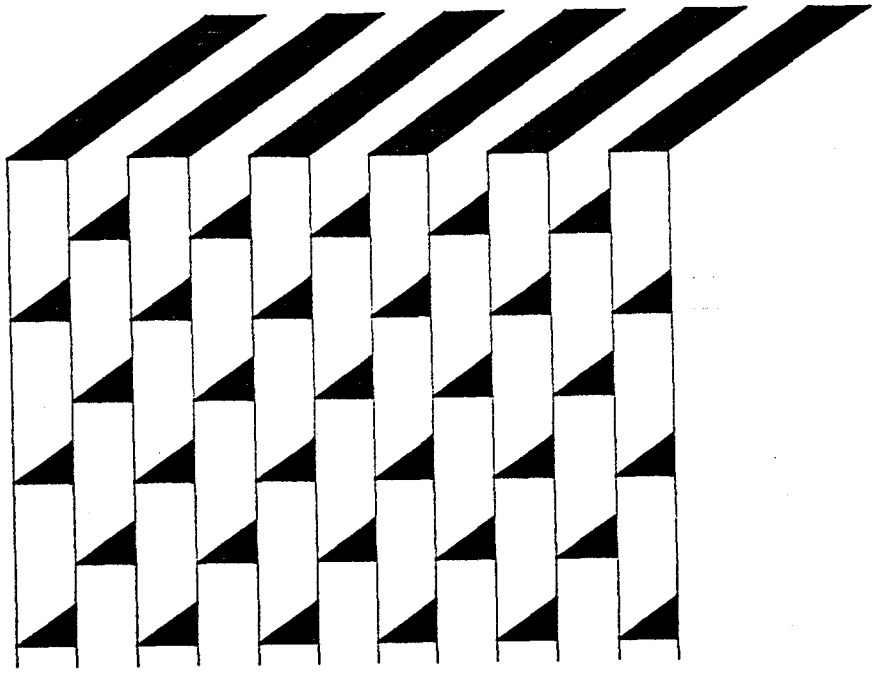

Fig. 7.1

Fig. 7.2 Schematic view of stage-2 domains with different domain sizes for a cleavage step model. The surface intercalant, due to cleaving, has a local concentration of x_s of a monolayer. The value of x_s for the two models shown here can be determined from theoretical Auger intensities (see text).

(a) A stage-2 crystal for a cleavage step model where the domain size is much smaller than the viewing resolution. Then the system appears as stage-1, except the average intercalant concentration is reduced by a factor of 2 as compared to the "usual" stage-1.

(b) A stage-2 crystal for a cleavage step model where the domain size is much larger than viewing resolution. On this scale, the system appears as a classical stage-2.

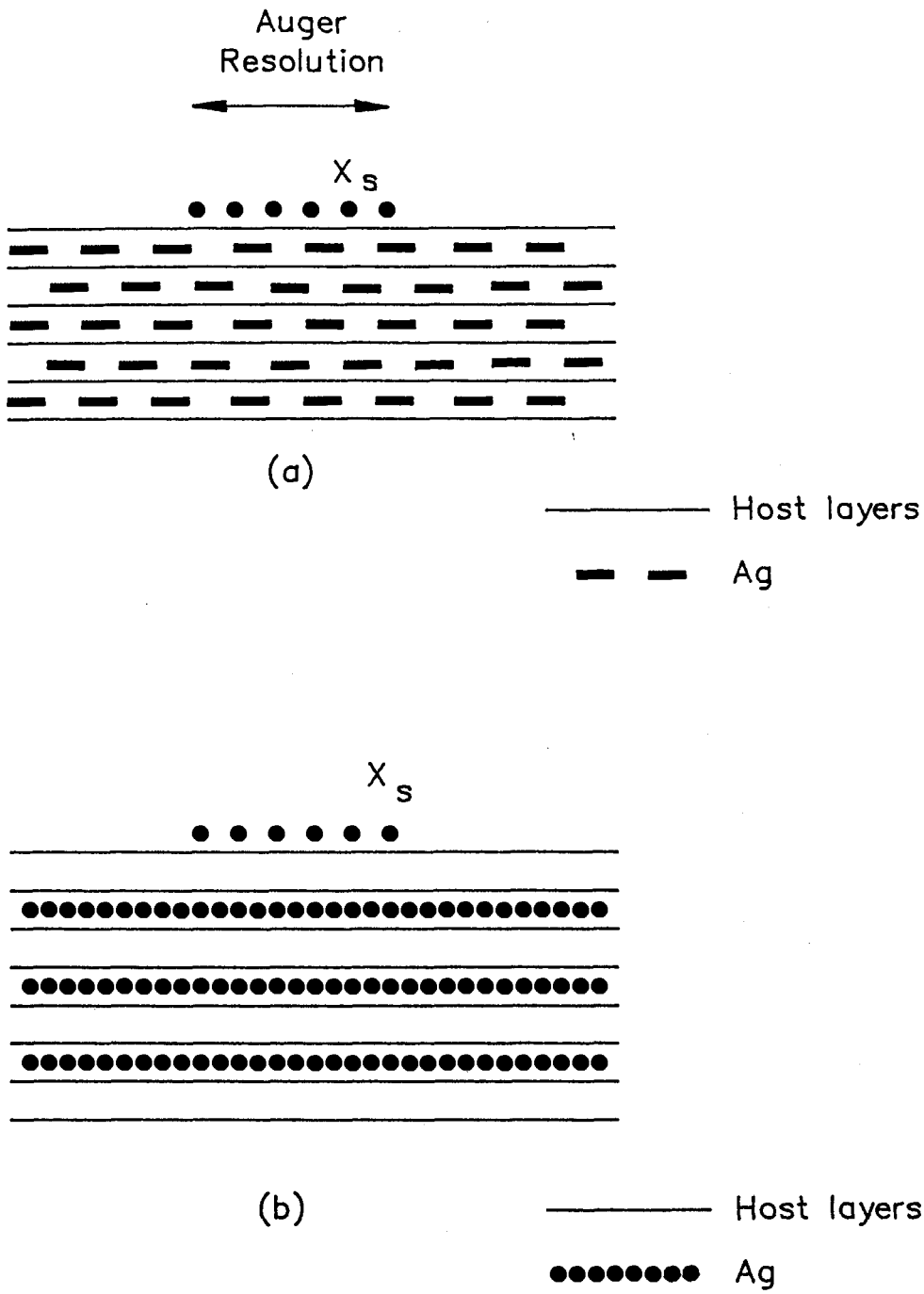

Fig. 7.2

Fig. 7.3 Channel reversal and cleavage step models.

(a) The cleavage steps formed during the cleaving process, which are perpendicular to the intercalated crystal edge, are irregular - they are shifted near a step parallel to the crystal edge. The amount of the shift is equal to one half of the step spacing.

(b) The cleavage steps formed during the cleaving process, which are perpendicular to the intercalated crystal edge, are regular - they are <u>not</u> shifted near a step parallel to the crystal edge. Subsequently, near the cleavage step which is parallel to the intercalated crystal edge, the entire crystal shifts laterally by an amount equal to one half of the step spacing.

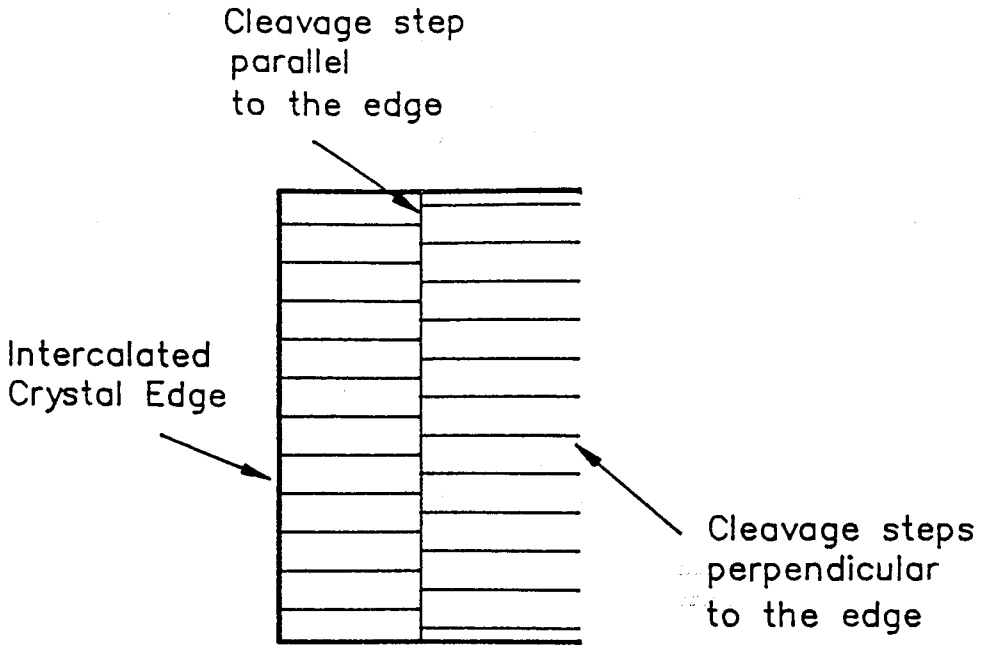
Cleavage step
parallel
to the edge
Intercalated
Crystal Edge
Cleavage steps
perpendicular
to the edge

(a)

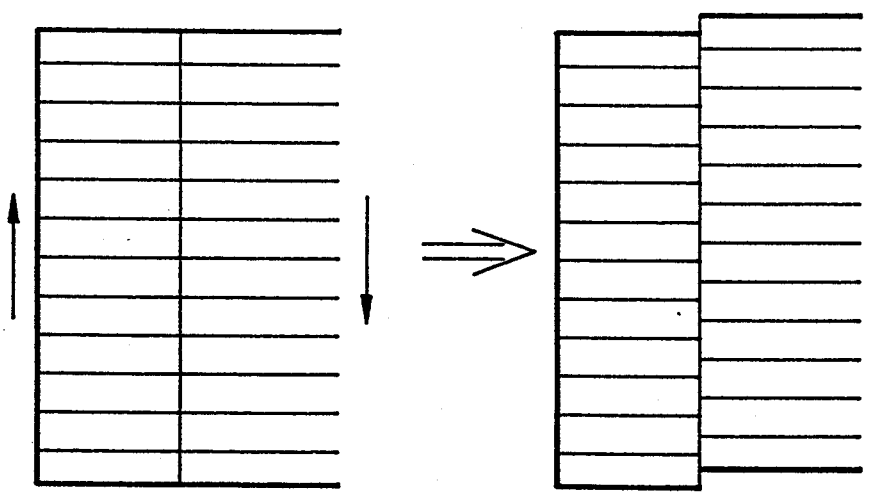

(b)

Fig. 7.3

Fig. 7.4 A cleavage step model with surface diffusion which does not describe the experimental observations. It is assumed that the domains, represented by the circles, are much smaller than 5 μm so that the galleries appear to be uniformly filled with intercalant.

(a) Upon cleaving, the intercalant in the cleaved gallery (open circles) splits equally. The cleavage steps form a regular staircase pattern.

(b) The surface intercalant in (a) then, diffuses away from the cleavage step on its own level. This results in intercalant distributions on the two which are not mirror images, in contrast to experimental observation.

(c) An example of a situation where the cleavage steps do not form a regular staircase pattern. Subsequent diffusion of the intercalant would, again, not result in the two surfaces not being mirror images.

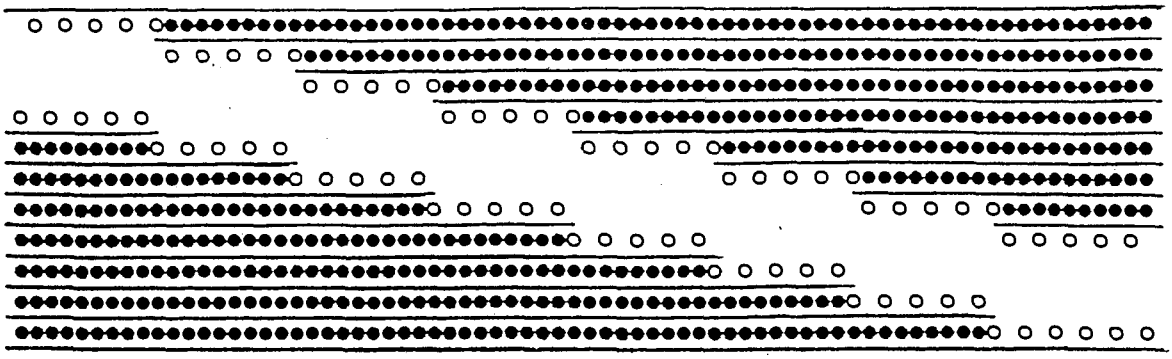

(a)

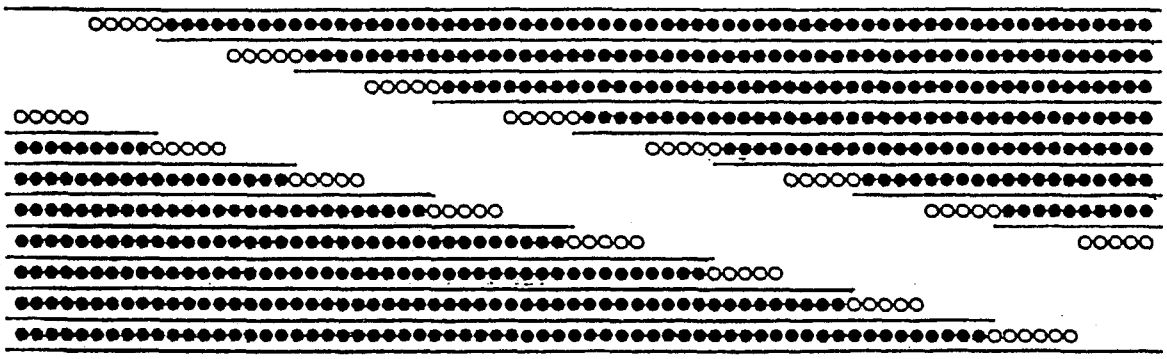

(b)

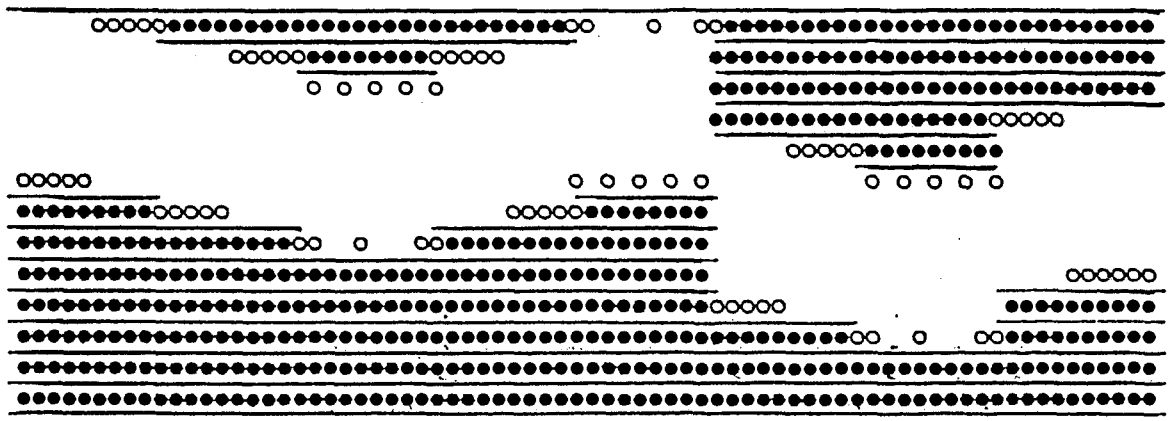

(c)

Fig. 7.4

Fig. 7.5 A cleavage step model, with no surface intercalant diffusion, which agrees with experimental observation. The cleavage steps are 5 μm apart. The domain size is much larger than 5 μm so the system appears as a classical stage-2. The cleavage steps must correspond to an odd number of host layers.

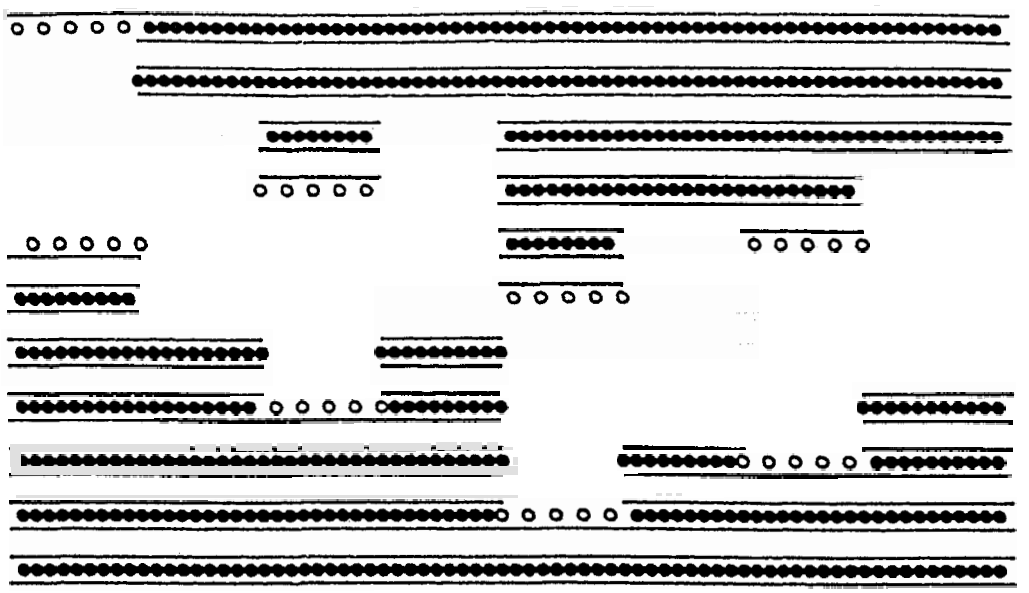

Fig. 7.5

Fig. 7.6 A stage-2 crystal with some galleries which do not intercalate. Staging is not expected near the empty galleries, as indicated. Cleaving would preferentially occur at these empty galleries as indicated by the arrows. In this situation, surface analysis would reveal a constant intercalant distribution.

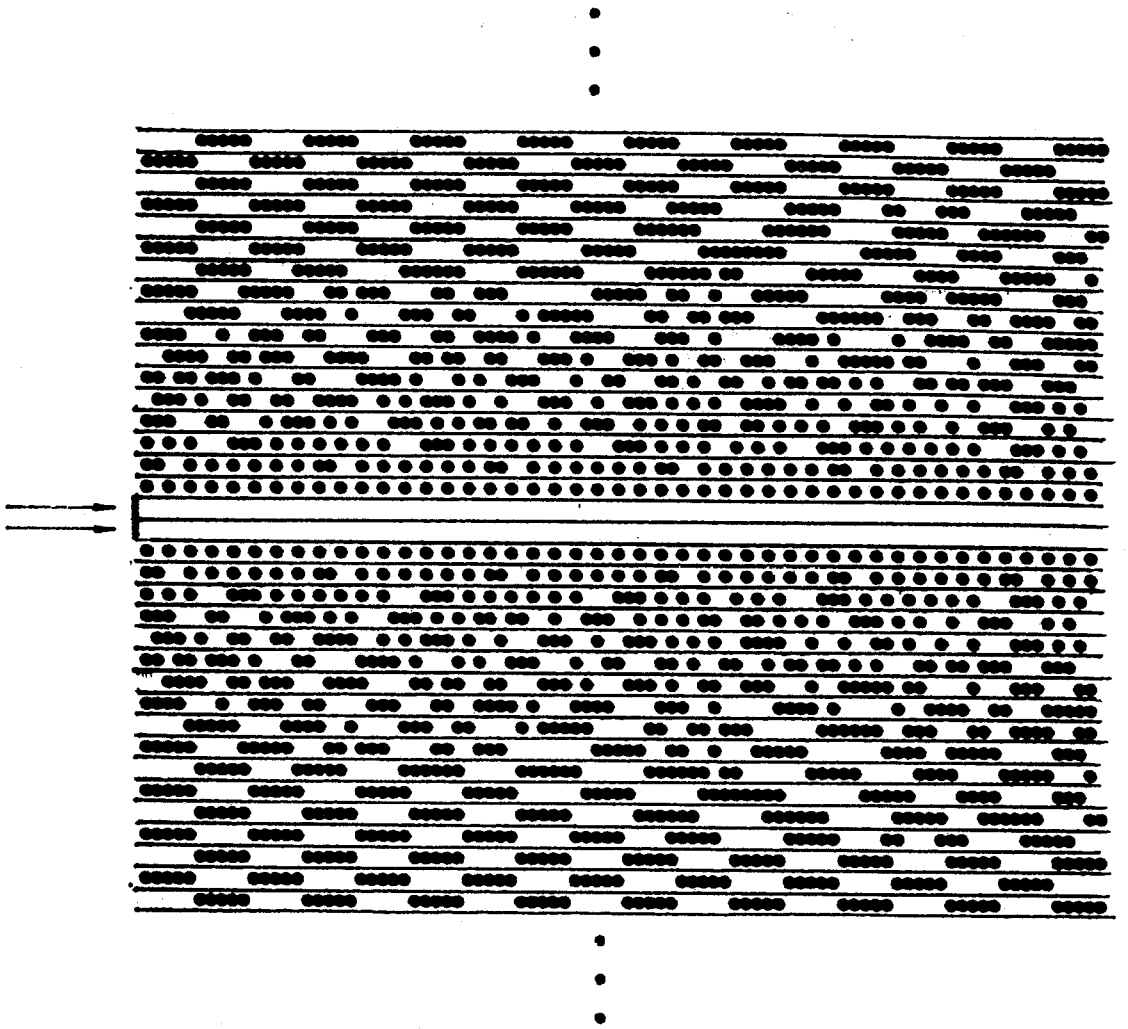

Fig. 7.6

CHAPTER 8

CONCLUSIONS

The surface distribution of intercalant on cleaved crystals of partially intercalated stage-2 Ag/TiS_2 was determined by a combination of Auger analysis and optical observation. The distribution of Ag is in the form of narrow finger-like structures, or channels. The channels extend from the intercalated crystal edge to the stage-2/empty crystal intercalation front, are about 5 μm wide and have a periodicity of about 10 μm. The channels are not in corner regions where two simultaneously intercalated edges of the crystal meet. Channels are seen in both stage-2 intercalated and stage-2 deintercalated crystals.

Assuming simple, symmetric cleaving effects, the surface channels are representative of the bulk intercalant distributions prior to cleaving. The channels are then interpreted as stage-2 Daumas-Hérold domains.

Monte Carlo computer simulations of intercalation and deintercalation revealed channel domains which resemble those observed experimentally. The simulations also give insight into the channel properties and under what conditions the channels can be surpressed or enhanced.

Partially intercalated stage-2 Ag/TiS_2 cleaved crystals are not stable over long periods of time and spontaneously deintercalate. The deintercalating Ag diffuses over the basal plane of the crystal and nucleates with any pre-existing Ag on the cleaved surface. This nucleation process allows the surface Ag distributions to be seen optically, and they correlate with the distributions seen with Auger analysis immediately after cleaving.

The channel domain model of staging is conceptually satisfying since it minimizes the domain wall area relative to other possible configurations. In addition, the intercalant can simply flow through channels, or along channel boundaries during intercalation, deintercalation and stage conversion. These mechanisms of transport do not require the movement of domains or atomic diffusion in regions where the host layers are unseparated. This helps to explain the seemingly quick speed at which crystals deintercalate from stage-1 to stage-2.

APPENDIX A

PARAMETERS FOR AUGER LINE SCANS AND MAPS

During Auger line scan and map data collection, the primary electron beam is rastered over the sample surface and the difference between the elemental Auger peak of interest and the background level is measured at each point in the rastering cycle. This difference is the measured intensity of the element displayed on Auger line scan data. In order to select the exact energy position of the Auger peaks and also level of the background in the vicinity of the Auger peak, a preliminary survey is done in a small energy window around the Auger peak of interest. Typical parameters are shown in Table A1.1a. The lower limit and the range define the energy window; the volts/step define the data collection points; the time/step defines how long to stay on each point; and the number of sweeps is a measure of how long to collect data. From the table, the data collection time was longest for Ag since it is the weaker of the Auger signals. The Auger peak positions and the background levels are determined from the obtained spectra, and typical values are shown in Table A1.1b. The peak energy defines the position of the Auger peak; the base energies define the background level; and the number of sweeps defines how long to do the line scan (or map) for each element. Again, since Ag has the weaker Auger signal, its data collection time is the longest.

The number of sweeps shown in the tables is only approximate, and varied from time to time, depending on the relative intensities of the elements. Also, for most peaks, only one base energy is sufficient to define the background level.

Table A1.1 Parameters for Auger line scans and maps.

(a) The energy windows used for the Auger peaks shown.

(b) The energies defining the positions of the Auger peaks, and the background levels near the peaks.

Table A1.1

(a)

ELEMENT NAME	Ti	Ag	S	C	O
LOWER LIMIT (eV)	372	336	137	257	495
RANGE (eV)	20	25	20	30	20
VOLTS/STEP	0.50	0.50	0.50	0.50	0.50
TIME/STEP (ms)	50	50	50	50	50
SWEEPS	2	8	1	4	4

(b)

ELEMENT NAME	Ti	Ag	S	C	O
PEAK ENERGY (eV)	379	348	147	263	509
BASE ENERGY (eV)	391	351	155	280	495
SECOND BASE ENERGY (eV)	0	342	0	0	0
SWEEPS	2	8	1	4	4

APPENDIX B

MONTE CARLO COMPUTER PROGRAM

The following is a sample program used for running the Monte Carlo intercalation simulations of Chapter 6. This sample program is set for intercalation into a crystal with the far edge unclamped (see Chapter 6 for details).

```
c     unclamp.f  : monte carlo simulation for diffusion on lattice
c     periodic in y and z directions.  particles introduced along
c     x=1.  the lattice is m wide by n long by 1 layers.  the
c     sites at the crystal edge at x=n is unclamped.
c     the variables are: np the site occupancy
c                        ne the neighbors of a site
c                        npos the positions of occupied sites
c                        v  the interaction energy
c
      integer np(30001), ne(9,6,30001), npos(30001), nm
      integer nfram, nc, n, m, l, q, t1, t2, t3, t4, t5,t6, x, y, z
      integer r1, r2, kk, jj, jjj, jn, re, kkk, site, occ, res, lm
      real *8 dseed,rseed, v(9), pel, beta, ef, ei, test
      real *8 uext, ers, c33, c44, a0, c0, vin, vout, a3, prs
      real *8 temper, roomt, a1, c1, vel, tem1, tem2, tem3, tem4
      real *8 fract, frac
      common /ranblk/dseed
      open(5,file='in.int')
      open(7,file='out.dat')
      open(8,file='ps.out')
c
c     read in the data from the input file
c
c     the number of frames
      read(5,11) nfram
c     the number of sweeps per frame
      read(5,12) nc
c     the lattice size
      read(5,13) n,m,l
c     the elastic dipole strength
      read(5,14) pel
c     the elastic parameters
      read(5,14) c33
      read(5,14) c44
c     the external potential and the reservoir energy
      read(5,14) uext
      read(5,14) ers
```

```
c     the inplane and out of plane electrostatic interactions
      read(5,14) vin
      read(5,14) vout
c     the lattice parameters
      read(5,14) a0
      read(5,14) c0
c     the temperature
      read(5,14) temper
      read(5,14) v(8)
11    format(i4)
12    format(i9)
13    format(i4,i4,i4)
14    format(f7.4)
c
c     write the input data to the output file
c
      write(7,101) nfram
      write(8,171) nfram
      write(7,102) nc
      write(8,172) nc
      write(7,103) n-1,m,1
      write(8,173) n-1,m,1
      write(7,104) pel
      write(7,105) c33,c44
      write(7,106) uext,ers
      write(7,107) vin
      write(7,108) vout
      write(7,109) a0,c0
      write(7,111) temper
      write(7,993) v(8)
101   format(' the number of frames is',i4)
102   format(' the number of cycles per frame is ',i9)
103   format(' the lattice size is ',i4,i4,i4)
171   format(i4)
172   format(i9)
173   format(i4,i4,i4)
104   format(' the elastic dipole strength is',f7.4,' ev')
105   format(' c33 =',f7.2,'  c44 = ',f7.2)
106   format(' external potential is',f7.4,' ers = ',f7.4)
107   format(' in plane electrostatic energy is',f7.4)
108   format(' out of plane electrostatic energy is',f7.4)
109   format(' lattice parameters are a0=',f7.2,' c0=',f7.2)
111   format(' the temperature is',f7.2)
993   format(' the nn out of plane interaction is ',f7.4)
c
c     the values of the interaction energy
c
      a3=c33/c44
      a1=a0
      c1=0.0
      v(1)=vel(pel,c44,a3,a1,c1)+vin
      a1=a0*1.73
```

```
      v(2)=vel(pel,c44,a3,a1,c1)
      a1=2*a0
      v(3)=vel(pel,c44,a3,a1,c1)
      a1=a0*2.65
      v(4)=vel(pel,c44,a3,a1,c1)
      v(5)=v(4)
      a1=a0
      c1=c0
      v(6)=vel(pel,c44,a3,a1,c1)
      v(7)=v(6)
      a1=0
c     v(8)=vel(pel,c44,a3,a1,c1)+vout
      c1=2*c0
      v(9)=vel(pel,c44,a3,a1,c1)
      v(9)=0.0
      v(6)=0.0
      v(7)=0.0
c
      roomt=300.0
      q=m*n*1
      nm=n*m
      1m=1*m
      beta=40*roomt/temper
      frac=exp(-(ers-uext)*beta)
      prs=frac/(1.0+frac)
c
c     initialize the configuration
c
      dseed=rseed()
      nocc=0
      do 100 j=1,q
100     np(j)=0
      np(q+1)=-1
      np(q+2)=-2
      np(q+3)=-3
c
c     now need to set up the nearest neighbors of the lattice sites.
c     this is done for the case up to 44 neighbors.  special
c     conditions are needed near the crystal edges.
c
      do 130 z=1,1
       do 140 y=1,m
        re=mod(y,2)
        do 150 x=1,n
         j=(z-1)*nm+(y-1)*n+x
c
c     first, sixth and seventh neighbors
c
         ne(1,1,j)=j+1
         ne(1,2,j)=j+n+1-re
         ne(1,3,j)=j+n-re
         ne(1,4,j)=j-1
```

```
          ne(1,5,j)=j-n-re
          ne(1,6,j)=j-n+1-re
          ne(6,1,j)=ne(1,1,j)-nm
          ne(6,2,j)=ne(1,2,j)-nm
          ne(6,3,j)=ne(1,3,j)-nm
          ne(6,4,j)=ne(1,4,j)-nm
          ne(6,5,j)=ne(1,5,j)-nm
          ne(6,6,j)=ne(1,6,j)-nm
          ne(7,1,j)=ne(1,1,j)+nm
          ne(7,2,j)=ne(1,2,j)+nm
          ne(7,3,j)=ne(1,3,j)+nm
          ne(7,4,j)=ne(1,4,j)+nm
          ne(7,5,j)=ne(1,5,j)+nm
          ne(7,6,j)=ne(1,6,j)+nm
          if(z.eq.1) then
            do 21 i=1,6
             ne(6,i,j)=ne(6,i,j)+q
21          continue
          endif
          if(z.eq.1) then
            do 22 i=1,6
             ne(7,i,j)=ne(7,i,j)-q
22          continue
          endif
          if(y.eq.1) then
             ne(1,5,j)=ne(1,5,j)+nm
             ne(1,6,j)=ne(1,6,j)+nm
             ne(6,5,j)=ne(6,5,j)+nm
             ne(6,6,j)=ne(6,6,j)+nm
             ne(7,5,j)=ne(7,5,j)+nm
             ne(7,6,j)=ne(7,6,j)+nm
          endif
          if(y.eq.m) then
             ne(1,2,j)=ne(1,2,j)-nm
             ne(1,3,j)=ne(1,3,j)-nm
             ne(6,2,j)=ne(6,2,j)-nm
             ne(6,3,j)=ne(6,3,j)-nm
             ne(7,2,j)=ne(7,2,j)-nm
             ne(7,3,j)=ne(7,3,j)-nm
          endif
          if(x.eq.1) then
            ne(1,4,j)=q+1
            ne(6,4,j)=q+1
            ne(7,4,j)=q+1
            if(re.eq.1) then
              ne(1,5,j)=q+1
              ne(1,3,j)=q+1
              ne(6,5,j)=q+1
              ne(6,3,j)=q+1
              ne(7,5,j)=q+1
              ne(7,3,j)=q+1
            else
```

```
            ne(1,5,j)=q+2
            ne(1,3,j)=q+2
            ne(6,5,j)=q+2
            ne(6,3,j)=q+2
            ne(7,5,j)=q+2
            ne(7,3,j)=q+2
          endif
        endif
        if(x.eq.n) then
          ne(1,1,j)=q+3
          ne(6,1,j)=q+3
          ne(7,1,j)=q+3
          if(re.eq.0) then
            ne(1,2,j)=q+3
            ne(1,6,j)=q+3
            ne(6,2,j)=q+3
            ne(6,6,j)=q+3
            ne(7,2,j)=q+3
            ne(7,6,j)=q+3
          endif
        endif
c
c       now do second neighbors
c
        t1=j-2*n
        t2=j-n+2-re
        t3=j+n+2-re
        t4=j+2*n
        t5=j+n-1-re
        t6=j-n-1-re
        if(y.le.2) t1=t1+nm
        if(y.ge.m-1) t4=t4-nm
        if(y.eq.1) then
          t2=t2+nm
          t6=t6+nm
        endif
        if(y.eq.m) then
          t3=t3-nm
          t5=t5-nm
        endif
        if(x.eq.1) then
          t6=q+1
          t5=q+1
        endif
        if((x.eq.2).and.(re.eq.1)) then
          t6=q+1
          t5=q+1
        endif
        if((x.eq.2).and.(re.eq.0)) then
          t6=q+2
          t5=q+2
        endif
```

```
          if(x.eq.n) then
            t2=q+3
            t3=q+3
          endif
          if((x.eq.n-1).and.(re.eq.0)) then
            t2=q+3
            t3=q+3
          endif
          ne(2,1,j)=t1
          ne(2,2,j)=t2
          ne(2,3,j)=t3
          ne(2,4,j)=t4
          ne(2,5,j)=t5
          ne(2,6,j)=t6
c
c       now for third neighbors
c
          t1=j-2*n+1
          t2=j+2
          t3=j+2*n+1
          t4=j+2*n-1
          t5=j-2
          t6=j-2*n-1
          if(y.le.2) then
             t1=t1+nm
             t6=t6+nm
          endif
          if(y.ge.m-1) then
            t3=t3-nm
            t4=t4-nm
          endif
          if(x.le.2) t5=q+1
          if((x.eq.3).and.(re.eq.1)) t5=q+2
          if(x.ge.n-1) t2=q+3
          if(x.eq.1) then
            t6=q+1
            t4=q+1
          endif
          if((x.eq.2).and.(re.eq.1)) then
            t4=q+2
            t6=q+2
          endif
          if(x.eq.n) then
            t1=q+3
            t3=q+3
          endif
          ne(3,1,j)=t1
          ne(3,2,j)=t2
          ne(3,3,j)=t3
          ne(3,4,j)=t4
          ne(3,5,j)=t5
          ne(3,6,j)=t6
```

```
c
c       now for fourth neighbors
c
        t1=j-3*n+1-re
        t2=j-n+3-re
        t3=j+2*n+2
        t4=j+3*n-re
        t5=j+n-2-re
        t6=j-2*n-2
        if(y.le.3) t1=t1+nm
        if(y.eq.1) t2=t2+nm
        if(y.ge.m-1) t3=t3-nm
        if(y.ge.m-2) t4=t4-nm
        if(y.eq.m) t5=t5-nm
        if(y.le.2) t6=t6+nm
        if((x.eq.n).and.(re.eq.0)) t1=q+3
        if(x.ge.n-1) t2=q+3
        if((x.ge.n-2).and.(re.eq.0)) t2=q+3
        if(x.ge.n-1) t3=q+3
        if((x.eq.1).and.(re.eq.1)) t4=q+1
        if((x.eq.1).and.(re.eq.0)) t4=q+2
        if(x.le.2) t5=q+1
        if((x.eq.3).and.(re.eq.1)) t5=q+1
        if((x.eq.3).and.(re.eq.0)) t5=q+2
        if(x.le.2) t6=q+1
        if((x.eq.3).and.(re.eq.1)) t6=q+2
        ne(4,1,j)=t1
        ne(4,2,j)=t2
        ne(4,3,j)=t3
        ne(4,4,j)=t4
        ne(4,5,j)=t5
        ne(4,6,j)=t6
c
c       now for fifth neighbors
c
        t1=j-3*n-re
        t2=j-2*n+2
        t3=j+n+3-re
        t4=j+3*n+1-re
        t5=j+2*n-2
        t6=j-n-2-re
        if(y.le.3) t1=t1+nm
        if((x.eq.1).and.(re.eq.1)) t1=q+1
        if((x.eq.1).and.(re.eq.0)) t1=q+2
        if(y.le.2) t2=t2+nm
        if(x.ge.n-1) t2=q+3
        if(y.eq.m) t3=t3-nm
        if(x.ge.n-1) t3=q+3
        if((x.eq.n-2).and.(re.eq.0)) t3=q+3
        if(y.ge.m-2) t4=t4-nm
        if((x.eq.n).and.(re.eq.0)) t4=q+3
        if(y.ge.m-1) t5=t5-nm
```

```
        if(x.le.2) t5=q+1
        if((x.eq.3).and.(re.eq.1)) t5=q+2
        if(y.eq.1) t6=t6+nm
        if(x.le.2) t6=q+1
        if((x.eq.3).and.(re.eq.1)) t6=q+1
        if((x.eq.3).and.(re.eq.0)) t6=q+2
        ne(5,1,j)=t1
        ne(5,2,j)=t2
        ne(5,3,j)=t3
        ne(5,4,j)=t4
        ne(5,5,j)=t5
        ne(5,6,j)=t6
c
c       now do eighth and ninth neighbors
c
         ne(8,1,j)=j-nm
         ne(8,2,j)=j+nm
         ne(9,1,j)=j-2*nm
         ne(9,2,j)=j+2*nm
         if(z.eq.1) ne(8,1,j)=ne(8,1,j)+q
         if(z.eq.1) ne(8,2,j)=ne(8,2,j)-q
         if(z.le.2) ne(9,1,j)=ne(9,1,j)+q
         if(z.ge.1-1) ne(9,2,j)=ne(9,2,j)-q
150     continue
140    continue
130   continue
c
c
c    now start the main monte carlo algorithm
c
c
      do 160 jj=1,nfram
       do 170 jjj=1,nc
c
c    pick a random occupied site
c
180       res=0
          occ=0
          r1=int((nocc+(lm/2))*randf())+1
          if(r1.gt.nocc+(lm/2)) r1=nocc+(lm/2)
c
c    if r1 is greater than nocc then a reservoir site
c    has been chosen
c
          if(r1.gt.nocc) then
c
c     check to see that the reservoir site is occupied
c
            if(randf().le.prs) then
c
c            the reservoir is occupied, so pick a random
c            reservoir site
```

```
c
              res=1
              occ=1
              ll=int(l*randf())+l
                if(ll.gt.l) ll=l
              ml=(int((m/2)*randf())+l)*2-l
                if(ml.gt.m) ml=m
              site=(ll-l)*nm+(ml-l)*n+l
            endif
c
c     otherwise it is an occupied lattice site
c
          else
            site=npos(rl)
            occ=l
          endif
c
c         now check to see if we picked and occupied site
c
          if(occ.eq.0) go to 180
c
c       pick a random direction for movement
c
          r2=int(6*randf())+l
            if(r2.gt.6) r2=6
c
c       if the site picked is not empty or not a reservoir
c       site then go back to the start
c
          kk=ne(l,r2,site)
          if((np(kk).eq.l).or.(np(kk).eq.-l)) go to 180
          if((np(kk).eq.-2).and.(randf().le.prs)) go to 180
c
c       now we have picked an occupied site and the movement
c       direction has an available site there
c
          ei=0.0
          ef=0.0
c
c     now calculate the energy of the initial and final
c     configurations.  afterward, the values must be corrected
c     for double counting of vl and for adding v8 and v9
c
c
          if(res.eq.l) then
             ei=ers
          else
            do 190 i=l,7
             do 200 j=l,6
              if(np(ne(i,j,site)).eq.l) ei=ei+v(i)
200          continue
190         continue
```

```
            if(np(ne(8,1,site)).eq.1) ei=ei+v(8)
            if(np(ne(8,2,site)).eq.1) ei=ei+v(8)
          endif
          if(np(kk).eq.-2) then
             ef=ers
          else
           if(np(kk).eq.-3) then
             ef=0.0
           else
             do 400 i=1,7
              do 410 j=1,6
               if(np(ne(i,j,kk)).eq.1) ef=ef+v(i)
410           continue
400          continue
             ef=ef-v(1)
             if(np(ne(8,1,kk)).eq.1) ef=ef+v(8)
             if(np(ne(8,2,kk)).eq.1) ef=ef+v(8)
           endif
          endif
c
c         now test for the change in energy
c
          if((ef-ei).le.0.0) go to 230
             test=exp(-beta*(ef-ei))
             if(randf().gt.test) go to 240
230       if(res.eq.0) then
             np(site)=0
             if(np(kk).eq.0) then
                np(ne(1,r2,site))=1
                npos(r1)=ne(1,r2,site)
             else
               if(r1.ne.nocc) then
                do 235 kkk=r1,nocc-1
                  npos(kkk)=npos(kkk+1)
235              continue
                endif
                nocc=nocc-1
             endif
           else
             nocc=nocc+1
             np(ne(1,r2,site))=1
             npos(nocc)=ne(1,r2,site)
           endif
240       continue
170      continue
         do 250 z=1,1
          do 260 y=1,m
              jn=(z-1)*nm+(y-1)*n
               write(7,202) (np(jn+x),x=2,n)
               write(8,202) (np(jn+x),x=2,n)
202            format(100(i1))
260       continue
```

```
         write(7,204)
204      format(' ')
250     continue
         fract=float(nocc)/float(m*l*(n-l))
         write(7,207) jj,fract
207      format(i3,f7.2)
        write(7,204)
160    continue
       close(7)
       close(5)
       close(8)
       stop
       end
c
c      the function vel calculates the elastic energy in
c      the safran hamman model
c
       function vel(p1,c4,a3,a,c)
       real *8 p1,c4,a3,a,c,teml,tem2,tem3,vel
         teml=-p1*p1*160.0*(a3*a*a-2.0*c*c)
         tem2=4.0*3.14*c4
         tem3=(a3*a*a+c*c)**2.5
         vel=teml/(tem2*tem3)
       return
       end
c
c
       function randf()
       implicit real (a-h,o-z)
       real randf
       real *8 dseed
       common /ranblk/dseed
       real *8 d2p31m, d2p31, amult
       data d2p31m/2147483647.D0/,d2p31/2147483648.D0/,amult/16807.D0/
       dseed=mod(amult*dseed,d2p31m)
       randf=dseed/d2p31
       end
c
c
       function rseed()
       implicit real (a-h,o-z)
       real *8 rseed
       external time
        integer time, longtime, seconds, minutes, timevector(3)
        integer i,irand
        longtime=time()
        call srand(longtime)
        call itime(timevector)
        minutes=timevector(2)
        seconds=timevector(3)
        ix=irand(longtime)
        do 885 i=1,seconds+10
```

```
        ix=irand(0)*irand(0)
885     continue
        rseed=ix/(minutes+1)
       end
```

LIST OF REFERENCES

1. M.S. Dresselhaus and G. Dresselhaus, Adv. Phys., 30, 139 (1981).

2. Physics and Chemistry of Materials with Layered Structures, F.A. Lévy, vol. 1 to 6, D. Reidel Publishing Company, Holland (1976).

3. J.A. Wilson and A.D. Yoffe, Adv. Phys., 18, 193 (1969).

4. R.H. Friend and A.D. Yoffe, Adv. Phys., 36, 1 (1987).

5. R. Clarke and C. Uher, Adv. Phys., 33, 469 (1984).

6. M.S. Whittingham and R.R. Chianelli, J. Chem. Ed., 57, 569 (1980).

7. L.F. Mattheiss, Phys. Rev. B8, 3719 (1973).

8. J.E. Fischer and H.J. Kim, Phys. Rev. B35, 6826 (1987).

9. G.A. Scholz and R.F. Frindt, Mat. Res. Bull., 15, 1703 (1980).

10. J.R. Dahn, D.C. Dahn and R.R. Haering, Solid State Commun., 42, 179 (1982).

11. J.R. Dahn and R.R. Haering, Can. J. Phys., 61, 1093 (1983).

12. J.R. Dahn and W.R. McKinnon, J. Phys. C17, 4231 (1984).

13. S. Hendricks and E. Teller, J. Chem. Phys., 10, 147 (1942).

14. S.A. Safran, Phys. Rev. Lett., 44, 937 (1980).

15. C.D. Fuerst, J.E. Fischer, J.D. Axe, J.B. Hastings and D.B. McWhan, Phys. Rev. Lett., 50, 357 (1983).
H.J. Kim, J.E. Fischer, D.B. McWhan and J.D. Axe, Phys. Rev. B33, 1329 (1986).

16. B. Marcus and Ph. Touzain, Synth. Met., 23, 13 (1988).

17. S.A. Safran and D.R. Hamann, Phys. Rev. B22, 606 (1980).

18. S.E. Millman and G. Kirczenow, Phys. Rev., B26, 2310 (1982).
S.E. Millman, G. Kirczenow and D. Solenberger, J. Phys. C15, L1269 (1982).
S.E. Millman and G. Kirczenow, Phys. Rev. B28, 3482 (1983).

19. J.G. Hooley, W.P. Garby and J. Valentin, Carbon 3, 7 (1965).
J.G. Hooley, Mater. Sci. Eng., 31, 119 (1977).

20. D. Kaluarachchi and R.F. Frindt, Phys. Rev. B31, 3648 (1985).

21. N. Daumas and M.A. Hérold, C. R. Acad. Sci., Ser. C, 268, 373 (1963).

22. S.A. Safran and D.R. Hamann, Phys. Rev. Lett., 42, 1410 (1979).

23. S. Ohnishi and S. Sugano, Solid State Commun., 36, 823 (1980).

24. G. Kirczenow, Phys. Rev. Lett., 55, 2180 (1985).
G. Kirczenow, Synth. Met., 12, 143 (1985).

25. G. Kirczenow, Can. J. Phys., 66, 39 (1988).

26. M.E. Misenheimer and H. Zabel, Phys. Rev. B27, 1443 (1983).

27. D. Kaluarachchi and R.F. Frindt, Phys. Rev. B28, 3663 (1983).

28. R. Clarke, N. Wada and S.A. Solin, Phys. Rev. Lett., 44, 1616 (1980).

29. A. Erbil, A.R. Kortan, R.J. Birgeneau and M.S. Dresselhaus, Phys. Rev. B28, 6329 (1983).
S. Flandrois, A.W. Hewat, C. Hauw and R.H. Bragg, Synth. Met., 7, 305 (1983).
F. Baron, S. Flandrois, C. Hauw and J. Caultier, Solid State Commun., 42, 759 (1982).

30. J.M. Thomas, G.R. Millward, R.F. Schlögl and H.P. Boehm, Mater. Res. Bull., 15, 671 (1980).

31. R. Levi-Setti, G. Crow, Y.L. Wang, N.W. Parker, R. Mittleman and D.M. Hwang, Phys. Rev. Lett., 54, 2615 (1985).

32. M. Bretz and R. Clark, Phys. Rev. Lett., 55, 2506 (1985).

33. M.S. Whittingham and J.A. Panella, Mater. Res. Bull., 16, 37 (1981).

34. H.P.B. Rimmington and A.A. Balchin, J. Crystal Growth, 21, 171 (1974).

35. G.A. Scholz, P. Joensen, J.M. Reyes and R.F. Frindt, Physica 105B, 214 (1981).

36. G.A. Scholz, The Silver Intercalated 2H-TaS_2 and 1T-TiS_2 Transition Metal Dichalcogenides, PhD Thesis, Simon Fraser University (1982).

37. M. Mori, K. Ohshima, S.C. Moss, R.F. Frindt, M. Plischke and J.C. Irwin, Solid State Commun., 43, 781 (1982).

38. Practical Surface Analysis, D. Briggs and M.P. Seah, John Wiley and Sons (1983).

39. Methods of Surface Analysis, A.W. Czanderna, Elsevier Publishing Company, N.Y., (1975), Chapters 1, 2, 5 and 7.

40. SAM-595 Instruction Manual, Perkin Elmer Corporation (1981).

41. Handbook of Auger Electron Spectroscopy, L.E. Davis, N.C. MacDonald, P.W. Palmberg, G.E. Riach, R.E. Weber, Perkin Elmer Corporation, Minnesota, 2nd Ed. (1978).

42. D Kaluarachchi, Intercalation and Distribution of Silver in the Transition Metal Dichalcogenide 1T-TiS_2, PhD Thesis, Simon Fraser University (1988).

43. J. Schramke and R. Schöllhorn, Solid State Ionics, 23, 197 (1987).

44. M.S. Whittingham, Prog. Solid St. Chem., vol. 12, 41 (1978).

45. Practical Surface Analysis, D. Briggs and M.P. Seah, John Wiley and Sons (1983).

46. A. Curzon, Simon Fraser University, private communciation

47. For example, see G. Binnig, H. Rohrer, Ch. Gerber, and E. Weibel, Phys. Rev. Lett. 49, 57 (1982) and references therein.

48. Electron Beam X-Ray Microanalysis, K.F.J. Heinrich, Litton Education Publishing Inc. (1981).

48. H.I. Starnberg and H.P. Hughes, J. Phys. C, 20, 4429 (1987).

50. M. Weber and T. Butz, Phys. Rev. Lett. 66, 361 (1991).

51. M. Schärli and F. Lévy, Phys. Rev. B, 33, 4317 (1986).

52. H. Wagner, Hydrogen in Metals, edited by G. Alefield and J. Völkl, (Springer, Berlin, 1978) Vol I, p. 5.

53. H. Wagner and H. Horner, Adv. Phys. 23, 587 (1974).

54. J.R. Dahn, W.R. McKinnon, R.R. Haering, W.J.L. Buyers, and B.M. Powell Can. J. Phys. 58, 207 (1980).

55. J.S. Langer, Rev. Mod. Phys. 52, 1 (1980).

56. D. Kaluarachchi and R.F. Frindt, Phys. Rev. B 39, 8175 (1989).

57. X. Qin, Simon Fraser University, unpublished.